UNIVERSITY OF CALIFORNIA
RIVERSIDE

The Development of a Linear-Quadrupole Electrodynamic Balance to Probe the Physical and Optical Properties of Aerosol Particles

A Dissertation submitted in partial satisfaction
of the requirements for the degree of

Doctor of Philosophy

in

Chemistry

by

Chelsea Liliana Price

December 2022

Dissertation Committee:
Dr. James F. Davies, Chairperson
Dr. Quan Cheng
Dr. Min Xue

The Dissertation of Chelsea Liliana Price is approved:

_____

_____

_____

Committee Chairperson

University of California, Riverside

ACKNOWLEDGEMENTS

Many thanks are extended to my advisor, Dr. James F. Davies, who guided and supported me through my graduate career. His confidence in me usually surpassed my own and I feel fortunate to have had such a positive mentor in my life. He truly pushed me to work and think independently, lessons which are both invaluable and priceless. I am thankful for the mentorship and am looking forward to our future friendship!

Thanks are also extended to the current and future lab members of the Davies lab. Your support, scientific knowledge, and lunch chit chats brightened the everlasting length of time in graduate school. A special thanks to Ravleen Kaur for always being a sounding board in scientific slumps and stumps as well as a lovely friend.

Thank you to my committee members Dr. Quan Cheng and Dr. Min Xue for their support and kind words after each milestone in my graduate career.

Thank you to my mental health counselors, Ethel and Grace, for all of your advice, patience and love. The number of times I expressed my frustration and tears trying to navigate graduate school must have been overwhelming, but your demeanor, words, and knowledge helped me grow as a person as well as a scientist. I am fortunate to have such strong women as role models in my life.

Thank you to my all my family members and friends for staying by my side through this process and being my personal cheerleaders, without your continued encouragement this would have been a much more difficult journey.

Finally, I would like to extend an eternal thanks to NKLA for bringing the most important angel into my life, Miss Marimekko. Initially I wanted a pet to keep me company

through graduate school and cross the rainbow bridge once I graduated, but her presence has helped me immensely. She provided such amazing insight into every part of graduate school and her comments to every paper and this thesis are incredible. She warmed my heart since the moment I brought her into my home and now I cannot imagine life without her.

COPYRIGHT ACKNOWLEDGEMENT

The text and figures of Chapter 3 of this dissertation were previously published, reprinted with permission from *J. Phys. Chem. A*, 2020, 124, 9, 1811 – 1820. The corresponding author, Dr. James Davies, directed and supervised the research that formed the basis of that chapter.

The text and figures of Chapter 4 of this dissertation were previously published, reprinted with permission from *Environ. Sci. Technol.*, 2022, 56, 7, 3941 – 3951. The corresponding author, Dr. James Davies, directed and supervised the research that formed the basis of that chapter.

The text and figures of Chapter 5 of this dissertation were previously published, reprinted with permission from *J. Phys. Chem. A*, 2022, 126, 39, 6963 – 6072. The corresponding author, Dr. James Davies, directed and supervised the research that formed the basis of that chapter

ABSTRACT OF THE DISSERTATION

The Development of a Linear-Quadrupole Electrodynamic Balance to Probe the Physical and Optical Properties of Aerosol Particles

by

Chelsea Liliana Price

Doctor of Philosophy, Graduate Program in Chemistry
University of California, Riverside, December 2022
Dr. James F. Davies, Chairperson

Aerosol particles present in the atmosphere influence climate through their interactions with light and their effect on cloud formation, and negatively impact air quality with significant health implications. In the atmosphere, aerosol particles can undergo transformations through an array of processes, including evaporation and condensation of semi-volatile compounds, oxidation initiated by heterogeneous reactions, and photochemistry initiated by solar illumination. The evolution of particle composition influences its physical and optical properties, which need to be understood to fully assess their role in the environment.

To study the physical and optical properties of aerosol particles, a linear quadrupole electrodynamic balance (LQ-EDB) was developed and used to levitate single aerosol particles using electric fields. This method allows for contactless probing of particle properties in controlled conditions that mimic the natural environment. To probe the size and optical properties of the particle, a broadband light source was integrated with the LQ-EDB to illuminate the particle, giving rise to morphology dependent resonances (MDRs)

that were sampled in a back-scattered geometry with a spectrometer. The wavelength of the MDR's was used to determine the droplet size, refractive index, and wavelength-dispersion parameters via Mie theory. These methods were initially benchmarked in measurements of the evaporation rates of semi-volatile organic particles and the refractive index of aqueous salt particles. These measurements identified the facility of the methods in exploring the optical properties of aerosol that regulate their interactions with incoming solar radiation.

In general, aerosol particles in the atmosphere have a cooling effect due to the scattering of incoming solar radiation. However, particles containing light absorbing species contribute to a warming effect. Using the LQ-EDB, we explored the physical and optical properties of aerosol particles containing light absorbing brown carbon (BrC) chromophores, such as those generated by wildfires and biomass burning. We report the optical properties, hygroscopic growth, and phase behavior as a function of relative humidity for a surrogate BrC particle containing 4-nitrocatechol and ammonium sulfate, revealing complex phase behavior that has implications for the optical properties and chemical reactivity of BrC aerosol.

Subsequently, a new LQ-EDB was developed that incorporated heating elements to study the vapor pressures and influence of phase state on the rate of evaporation of a series of linear dicarboxylic acids from 293 to 350 K. These measurements provide clear evidence that phase state, either crystalline or amorphous, is a controlling factor in the rate of evaporation and contribute to our broader understanding of liquid-vapor partitioning in organic aerosol, organic solvents, fuel mixtures, and semi-volatile household products.

TABLE OF CONTENTS

LIST OF FIGURES

LIST OF TABLES

CHAPTER I

1.1 Overview of Atmospheric Aerosol Particles

Aerosol are ubiquitous in the atmosphere, local environments and many industrial processes. They can be used in drug and pesticide design, can affect human health, but also play an integral role in the atmosphere, affecting visibility, air quality, and climate.[1–8] Along with this versatility comes complexity. An aerosol is a suspension of particles in a gas phase. They consist of organic and inorganic material and are constantly changing in the atmosphere due to interactions with their surrounding environment, complicating their function and fueling the desire to better understand their role.[9,10]

Volatile organic compounds (VOCs) are emitted from biogenic and anthropogenic sources. These compounds can continuously exist in the gas phase or they can chemically transform through homogeneous reactions in addition to heterogenous and multiphase reactions when the gas phase reacts with liquid or solid particles. Another reaction pathway for gas and particle phase species is oxidative reactions to form secondary organic aerosol (SOA).[10,11] These atmospheric reactions age aerosol changing their size and chemical composition affecting properties such as volatility, hygroscopicity, and morphology as well as optical properties.[10,12]

Aerosol in the atmosphere can indirectly or directly impact climate. Both indirect and direct effects refer to how aerosol contributions to cloud formation and how aerosol scatter light, respectively, have changed since pre-industrial times. Aerosol can act as cloud condensation nuclei (CCN) eventually forming a cloud whose properties are influenced by the initial aerosol particles.[9,13] Aerosol particles can directly scatter or absorb light, leading

to a cooling or heating effect, respectively.[9] Organic aerosol particles in the atmosphere typically do not absorb solar radiation, but recent studies have shown that brown carbon (BrC) containing aerosol will absorb light.[13–15] Studies have shown that black carbon, emitted from industrial processes and wildfires, absorbs light across all wavelengths and greatly contributes to climate change.[16] Wildfires also emit BrC which absorbs light in the visible and UV range and is an additional contributor to climate change.[13]

Given the complexity of atmospheric aerosol, their effects on climate remain largely uncertain, as depicted in Figure 1.1.[17] This figure shows the contributions of each atmospheric species to radiative (climate) forcing (RF) along with their uncertainties (horizontal bars). Positive RF leads to surface warming while negative RF leads to surface cooling. Numerical values are shown to the right of the emitted compound with their level of confidence of very high (VH), high (H), medium (M), or low (L). Overall, the total anthropogenic RF for 2011 relative to 1750 is 2.29 Wm^{-2} and has increased almost four-fold since 1950, confirming that anthropogenic emissions impact climate. The RF contribution from aerosol and precursors is highlighted in Figure 1.1 (blue box). The positive RF is attributed to organic and black carbon while the negative RF comes from mineral dust, sulfate, nitrate, etc. While there is a high confidence associated with the contribution from aerosol, there is low confidence with cloud adjustments due to aerosols, indicating more information is needed to understand aerosol-cloud interactions. Furthermore, both contributions include high uncertainty values, which can be reduced through additional studies that better constrain the effects of aerosol and their global variability.

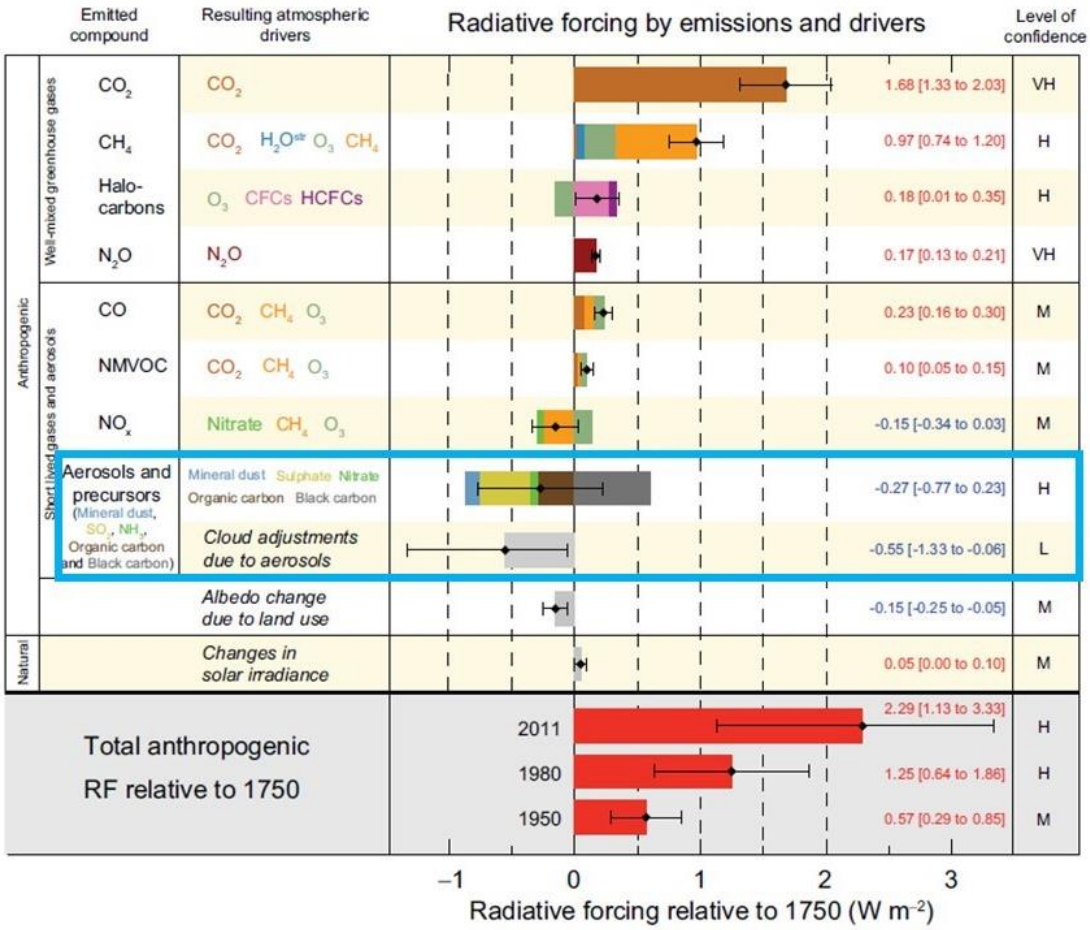

Figure 1.1: Components contributions to radiative forcing (climate change) with uncertainties. Figure reproduced from IPCC 2013 report.[17]

An improved understanding of aerosol physical and chemical properties will allow us to better understand their role in the atmosphere and impacts on climate, industrial applications, and human health.

1.1.1 Sources of Aerosol

Aerosol are generated from either natural or anthropogenic sources. Natural sources consist of vegetation (plants, soil, biomass burning), oceanic, volcanic and dust emissions, while anthropogenic sources include vehicular and industrial processes that involve the combustion of fossil fuels, and fires started by humans.[18,19] Aerosols emitted directly, from either natural or anthropogenic sources, in the liquid or particulate form are primary aerosols (PA). These include aerosol produced directly from sea spray, terrestrial surfaces, and incomplete combustion. Secondary organic aerosol (SOA) form from the gas to particle conversion initiated by gas phase oxidants and volatile organic compounds (VOC).[18,20,21] This includes new particle formation through nucleation and condensation of gaseous precursors on existing particles. Newly formed particles can then transform through heterogenous and multiphase reactions changing the composition of the particle. Further gas phase oxidation of SOA in the atmosphere is initiated by oxidants like ozone, nitrogen oxides, and hydroxyl radicals which ages and oxidizes the SOA lowering volatility and increasing oxygen-to-carbon ratio (O/C).[9,18] This allows SOA to exist in a variety of compositions and sizes giving clues to their source of origin.

1.1.2 Composition of Aerosol

Depending on the source, aerosol can exist in the atmosphere with a broad particle size distribution with diameters (d) ranging from 1 nm to 100 μm. For example, aerosol resultant from mineral dust, pollen, and sea spray typically fall within 1 μm < d < 100 μm, while soot particles and SOA range from 10 – 100 nm.[4,9,18,22] Aerosol particles that are less than 1 μm generally consist of carbon, nitrates, sulfates, and ammonium ions.[19,22] In

addition, aerosol emitted from biomass burning are generally small (> 1 μm) and result from the incomplete combustion of organic matter. They consist of organic carbon often associated with hydrogen and oxygen atoms, as well as black and brown carbon.[13,22] Conversely, coarse particles have diameters between 1 μm and 10 μm, and contain inorganic materials like sea salt, Ca, Fe, and Si, in addition to the compounds that form smaller particles.[5,9,19,22] A comparison of the various size ranges is depicted in Figure 1.2. This is an overview of atmospheric processes that create and transform aerosol along with a highly variable size distribution for each process ranging from 10^{-2} – 10^{2} μm.

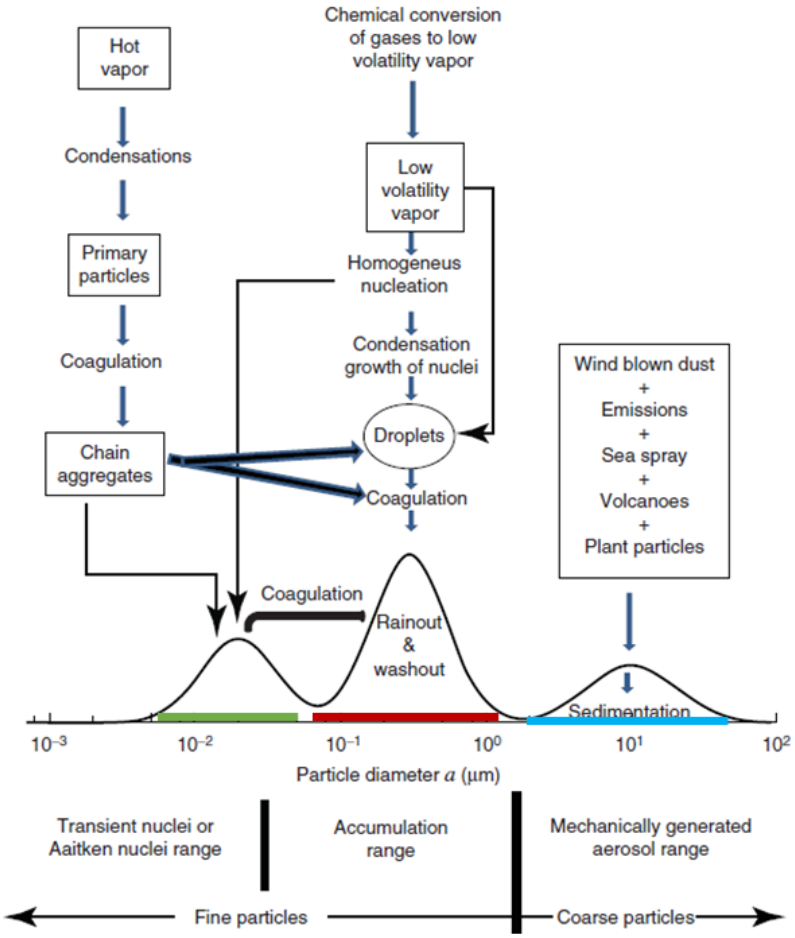

Figure 1.2: Schematic of Size distribution of aerosol. Primary or secondary particles (green), Primary and secondary particles (red), and primary particles (blue). Figure adapted from Finlayson-Pitts[23] and Tomasi et al.[21]

The variability in size also affects their lifetime in the atmosphere. Typically, larger aerosol particles have a shorter lifetime while smaller aerosol particles have a longer lifetime. Larger aerosol particles (> 2 µm) are susceptible to gravitational settling while smaller aerosol particles (< 0.1 µm) can diffuse and coagulate with larger particles.[23]

The size of an aerosol particle is also an indication of how it was formed in the atmosphere. Smaller particles can be categorized into three areas:[9,18,19]

- Particles with diameters (d) that are < 10 nm are fresh particles formed through the nucleation process
- Particles between 10 nm < d < 100 nm are formed through condensation of pre-existing particles or vapor nucleation
- Particles between 0.1 μm < d < 1 μm are formed through direct emission, the condensation of vapors, or coagulation of smaller particles

Since the size range of aerosol particles is so large, the aerosol particle concentration also spans several orders of magnitude (up to 108 cm-3).[23] Particle concentration can be reported as number concentration (number of molecules/volume of air) and mass concentration (mass of gas X/volume of air). When comparing urban to remote areas, both the number-and mass- concentration are much higher in urban areas due to more anthropogenic emissions, as depicted in Figure 1.3. The pie charts show the mass concentration breakdown of different aerosol. For example, remote areas, denoted in pink text, typically show a higher mass concentration of sulfates (red) due to their proximity to the ocean. Contrarily, urban emissions, denoted in blue text, generally show a higher mass concentration of organics (green) mainly due to anthropogenic emissions. In Riverside, CA mass concentrations are categorized into organics, nitrate (blue), sulfate, and ammonium (orange). Organic emissions make up a little under half of the pie chart, while nitrate, sulfate and ammonium make up the other half. This breakdown makes Riverside a city of interest in Southern California due to its diverse emissions.

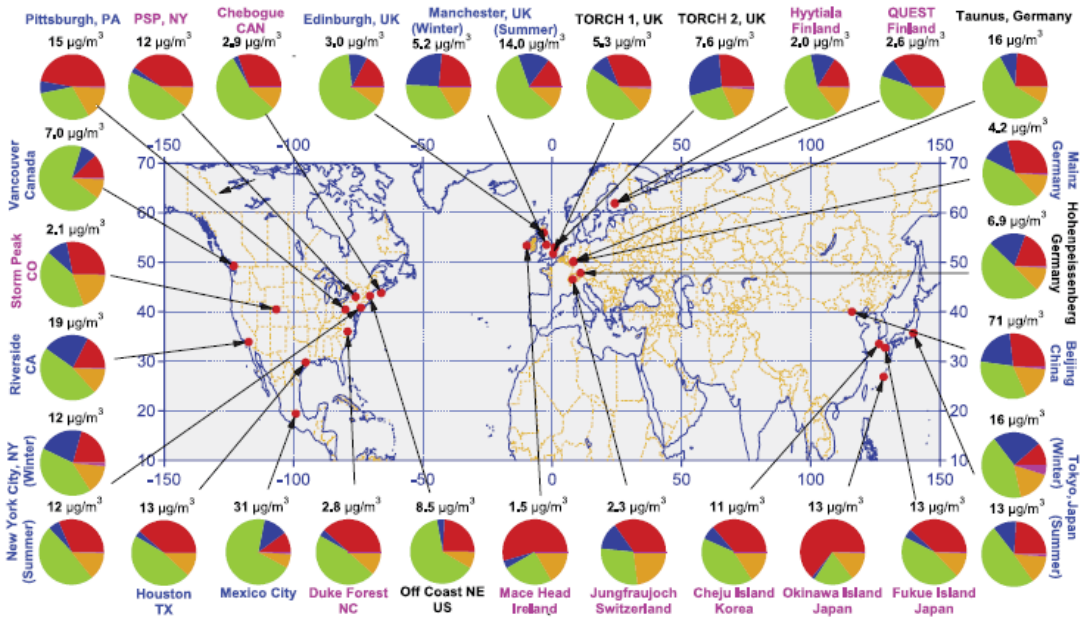

Figure 1.3: Mass concentrations of collected aerosol (pie chart) in urban (blue text) and remote (pink text) areas. Pie charts breakdown concentrations into organics (green), sulfate (red), nitrate (blue), ammonium (orange), and chloride (purple). Figure reproduced from Zhang et al.[24]

A wide range of sizes and concentrations exist because atmospheric aerosol undergo various physical and chemical transformations that change their size and chemical composition. These transformations include condensation, evaporation, and gas- and aqueous- phase reactions that influence their effects in the atmosphere.[9,23]

1.1.3 Climate Effects of Aerosol

Greenhouse gases are long lived contributors to climate change, yet aerosol particles also impact the global radiation balance through direct and indirect effects and have been determined to contribute to climate change according to the IPCC report (see Figure 1.1).[17] This finding has influenced the desire to better understand the climate effects of aerosol particles.

Aerosol particles may impact climate in two ways:

- Directly by changing the amount of heat in the atmosphere
- Indirectly by influencing cloud formation

Both natural and anthropogenic aerosol particles present in the atmosphere scatter and absorb solar and thermal radiation, directly impacting climate. An aerosol particle that scatters and reflects radiation cools the Earth's surface due to a reduction of incoming radiation and loss of energy. An aerosol particle that absorbs radiation warms the earth's surface since the absorbed energy is remitted as heat to its surroundings.[5,22,23] This is evident in both the suspended aerosol particle as well as when the particle is deposited on a surface, like a snow pack, leading to a warming effect.[25] The magnitude of cooling or heating is governed by composition, size, and number concentration, as well as properties like hygroscopicity, density, and refractive index. These properties are affected by both the source of the aerosol and its environment.[25–27] The environment in which aerosol exist is complex and can both age and mix aerosol with other species. This can impact hygroscopic behavior, reactivity, composition, and optical properties.[27,28] An organic coating may form on the surface of an inorganic particle and influence its hygroscopicity by enhancing or impeding its ability to uptake water, changing the refractive index of the particle and its evaporative properties.[29] The mixing state is also of importance to black- and brown carbon particles (BC or BrC). These particles arise from anthropogenic emissions and biomass burning and are known to absorb radiation. The presence of other aerosol species in the particle can form a shell around the BC core, enhancing absorption, known as the lensing effect, and increasing the warming of surroundings.[30,31] In addition to their absorptive

properties, BrC particles may be water soluble, increasing their hygroscopicity and ability to act as cloud condensation nuclei.[32]

When aerosol act as cloud condensation nuclei (CCN) they indirectly impact climate. In a hygroscopic aerosol, water vapor molecules that interact with the particle may be absorbed and lead to an aqueous droplet with an increased diameter.[9,33] In supersaturated relative humidity conditions (i.e. RH > 100%), these particles can act as CCN to form cloud droplets and eventually clouds. The properties of the cloud depend on the microphysical properties of the CCN, and depending on the size distribution, number concentration and composition of the aerosol, the cloud may exhibit different optical properties that influence cloud-radiation interactions[9,19,23] If there is a large aerosol number concentration, there is an increase in the concentration of CCN and therefore an increase in the number of cloud droplets. With a fixed water content, this would lead to an increase in reflectivity (less solar radiation absorbed) and a cooling of surroundings since lifetime is prolonged.[18,22] Absorbing aerosol particles, such as BrC, that are water-soluble can also serve as CCN and further alter the microphysical and optical properties of clouds.[32]

The direct and indirect effects of aerosol particles in the atmosphere are complex and dependent on multiple factors that are always being researched. Aerosol particles, however, do not exclusively impact climate, but also affect air quality and human health.

1.1.4 Air Quality and Health Effects of Aerosol

Over the past decades, anthropogenic emissions have increased substantially and have in turn worsened air quality. While this is globally apparent, efforts have been introduced to lessen the impact of anthropogenic emissions and improve air quality.

The southern California region was once known for its crippling smog in the early to late 1900s. The smog resulted from aerosol particles present in the atmosphere that existed as haze, which decreased visibility and impacted human health.[18,22,34] Emissions from smog producing cars impacted visibility so greatly that Los Angeles City Hall was regularly obscured and people walking through the city streets complained of burning eyes and lungs.[35,36] The burning arose from smaller and finer aerosol particles with diameters less than 2.5 μm, also known as particulate matter ($PM_{2.5}$). These particles are so small that they can be inhaled and deposited in lungs and even translocated into the bloodstream, depending on their size.[3,4,34] Other possible health effect of $PM_{2.5}$ include obstruction of respiratory pathways leading to asthma, allergies, and oxidative stress triggered by aerosol particles containing oxygenated aromatic compounds or transition metals.[22,34] The smog in Los Angeles was so thick that in 1943 visibility shrank to only three city blocks. The record ozone level and smoggiest day in history occurred on September 13, 1955 with an ozone concentration of 0.68 parts per million (ppm) in downtown Los Angeles - a major concern for health.[36] This triggered the founding of the California Air Resources Board (CARB) in 1967 in hopes to improve air quality.[35] Following their establishment, California pushed oil companies to produce unleaded gas with fewer smog forming ingredients, power plants to shift from oil to natural gas, and equip new cars with catalytic converters.[35,36]

Concurrently, residents of Riverside and San Bernadino counties, east of Los Angeles, complained about the drifting smog which worsened air quality in the inland region. After these complaints, the South Coast Air Quality Management District (SAQMD) was formed to address any issues related to air quality and subsequently adopted regulations to reduce emissions.[35] Since SAQMD's formation, the 8-hour ozone average (ppm) has decreased over time with a 2020 average of 0.139 ppm, significantly less than the peak in 1955.[37] UC Riverside has played an important role in air quality research over the decades with the Center of Environmental Research and Technology (CE-CERT) and will continue to do so with the aid of SAQMD and CARB.[38] Recently, SAQMD approved a grant for UC Riverside to boost air quality research and training and CARB opened its Southern California headquarters on UC Riverside property. CARB's new research facility will help transition California to a zero-emission state using their vehicle emission testing and research facilities.[38,39] Although improvements have been made to Southern California's air quality, studies are still necessary to further technological advancements and to gain a comprehensive understanding of the complexity of aerosol particles to fully grasp their role in the atmosphere and avoid backpedaling to smoggier times. Further, with the increased prevalence of wildfires introducing significant quantities of biomass burning aerosol and smoke into the atmosphere, understanding the role of new kinds of aerosol in the environment will be crucial. A detailed knowledge of the chemical composition, physical properties, and atmospheric interactions of aerosol particles is necessary for constraining their effects on climate and air quality.

1.2 Properties of Aerosol

1.2.1 Physical State

Aerosol in the atmosphere have a complex composition and can be comprised of a mixture of inorganic salts, organic components, and water. The chemical composition of aerosol dictates hygroscopicity, which is the ability of an aerosol particle to uptake water and maintain water molecules in the condensed phase.[9,34] This property is related to the environmental relative humidity and varies the size, physical and optical properties of aerosol, and the phase state of the particles. Typically, inorganic aerosol particles exhibit a decrease in size with relative humidity until the efflorescence point is reached, at which point nucleation of a solid phase occurs and the particle crystallizes. Conversely, when the relative humidity is increased the solid particle may jump in size quickly at the deliquescence point, where the particle goes from the solid to the liquid phase and will continue to grow as the relative humidity increases.[9,18,23] The efflorescence and deliquescence RH (DRH and ERH) are often different, leading to hysteresis in the RH response of an aerosol and an increased importance of knowing the RH history of the particle. Usually, hygroscopic growth measurements are reported using growth factors that relate the hydrated size at a specific RH to the dry size at 0% RH. The growth curves in Figure 1.4 are representative of a pure inorganic salt, NaCl, and an arbitrary organic particle. The growth curve for NaCl shows three key features: the efflorescence and deliquescence RH and hysteresis (40 – 75 % RH) where the droplet enters a super saturated state with respect to the solute before efflorescence. These features, however, are missing from the organic particle's growth curve because organic particles are known to phase

separate at low RHs instead of effloresing. In addition, the mass growth factors (ratio of the particle mass at a given RH to the dry particle mass) differ between NaCl and the organic particle. NaCl is more hygroscopic than an organic containing particle and will have a larger mass growth factor at high RHs.

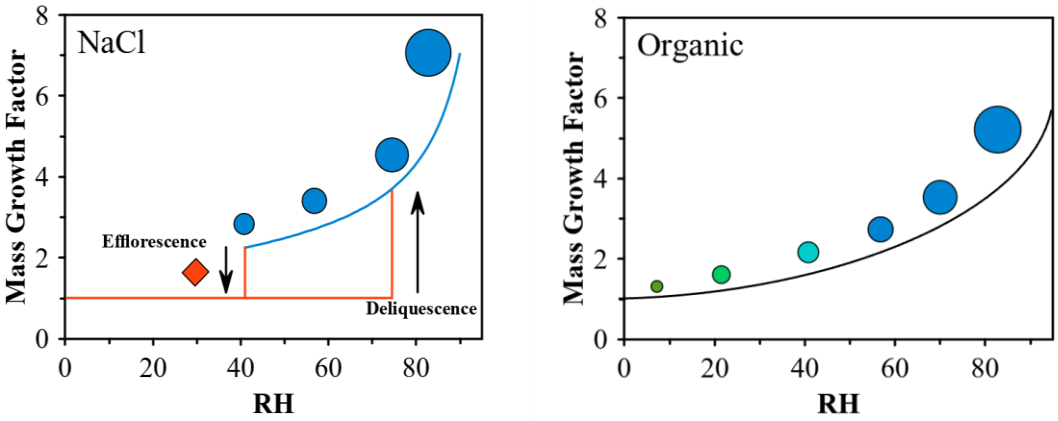

Figure 1.4: Representative hygroscopic growth curve for NaCl and an organic containing particle.

Aerosol in the atmosphere consist of several species, so pure component growth curves, as seen with NaCl in Figure 1.4, are not truly representative of atmospheric aerosol, but provide a reference point. Different mixing states of organic and inorganic components can influence physical properties, like hygroscopicity. Generally when organic components are well-mixed (homogenous) with inorganic salts, the DRH and ERH are lower than that of the pure salt because the highly polar organic species increases the solubility of the salt while the increased viscosity impedes crystallization .[40] When the organic and inorganic components are not well-mixed, the organic components may phase separate from the inorganic part creating little to no change in DRH or ERH of the pure inorganic component. This shows that organic rich particles do not follow the same behavior as inorganic particles. Instead of the definite phase changes associated with aqueous inorganic particles

at the deliquescence and efflorescence points, organic rich particles enter viscous, glassy, semi-solid or amorphous states with decreasing RH which impedes diffusion and efflorescence.[41,42]

Organic rich and inorganic aerosol are both hygroscopic and may activate into CCN once their specific supersaturation is reached. Inorganic aerosol are usually very hygroscopic and have well determined deliquescence and efflorescence points. When other components are added to aerosol, such as the presence of insoluble material, the efflorescence and deliquescence point may shift.[18,22,43] Organic rich aerosol in the atmosphere come from SOA that became oxidized in the atmosphere leading to oxygen rich compounds with an increased O/C ratio, making them less volatile and more hygroscopic.[23,44] Hygroscopicity is a key component of Köhler theory, which describes how cloud droplets are formed and applies best to homogenous aerosol particles. When multiple components are present in an aerosol particle, extensions and simplifications of this theory are needed. One simplification, the hygroscopicity parameter, κ, describes the hygroscopic properties of an aerosol particle with one parameter that relates to the chemical composition, and is empirically derived from hygroscopicity and CCN activity measurements.[45] The properties of multi-component aerosol particles in the atmosphere can be altered through cloud processing. In addition, existing multi-component aerosol that are immiscible at low RH can become miscible as RH increases and may form CCN. If the RH decreases before this point is reached, liquid-liquid phase separation (LLPS) may occur since the organic components that partitioned in the particle become immiscible at low RH.[43] If multi-component aerosol form cloud droplets, cloud processing further mixes the

inorganic and organic components and may change O/C. If the new O/C is around 0.6, these aerosol particles may undergo LLPS.[43] Internal reactions go on until the cloud has dissipated. As water is lost due to cloud evaporation, inorganic and organic components present in aerosol particles may become immiscible leading to LLPS. Generally, LLPS aerosol particles resultant from cloud processing exist in a core-shell morphology.[43]

Core-shell morphologies are not the only configuration LLPS aerosol particles can adopt. If multiple components are internally well-mixed in the spherical aerosol particle, it is fully homogenous. Aerosol mixing can occur in the atmosphere through the condensation of volatile compounds onto particles and the coagulation of compositionally different particles.

When these components are not entirely miscible LLPS occurs, giving rise to different physical states. The physical state of an aerosol particle not only depends on chemical composition, but also relative humidity and temperature.[46,47] Variations in relative humidity can cause aerosol to enter phase transitions such as LLPS, deliquescence and efflorescence. Phase separation occurs due to low miscibility caused by alterations in activity coefficients of components and water, polarity, and surface tension.[44] This is more apparent at low RH due to decreased water activity, causing the organics to be salted out.

Due to these effects, spherical aerosol particles can exist as:

- Fully homogeneous (one liquid phase)
- Core Shell (two liquid phases)
- Crystalline (solid)
- Partially engulfed / inclusion containing (liquid phase with solid areas)

Particle morphology influences their reactivity in the atmosphere. Adopting a core-shell morphology impedes the core (inner) phase from interacting with any gas-phase species and deters the exchange of volatile organics and water. In a partially engulfed morphology, both phases can interact with gas-phase species. The physical state of aerosol particles is tied to both their reactivity in the clouds as well as in the atmosphere.[43] These physical properties are strongly related to optical properties which vary as physical properties change in the environment.

1.2.2 Optical Properties

Atmospheric aerosol interact with light through scattering or absorption. Together, scattering and absorption are described by the complex refractive index of the particle, denoted as:

$$n\,(\lambda) = m(\lambda) + ik(\lambda) \tag{1.1}$$

where *m*, the real component, is representative of scattering and *k*, the imaginary component, is representative of absorption. The complex refractive index fully describes how a material interacts with light and, when coupled with the size distribution and morphology of the aerosol particles, can fully describe how an aerosol interacts with light.

A particle scatters light when the direction of incident light is altered without absorption. This may be in the form of reflection, refraction, or diffraction of light. Scattering is most efficient when the particle radius is equal to or larger than the wavelength of incident light. Particles with too small of radii are inefficient scatterers of light. Mediums like air and water have refractive indices of 1.00 and 1.33, respectively. Water present in the atmosphere is a strong indication of the relative humidity aerosol is exposed to and can be absorbed into existing aerosol particles. Inorganic salts in the atmosphere are highly hygroscopic and the associated RI trend can be followed. For example, if an aerosol particle has a RI of 1.39 at 75 % RH, the RI would tend towards that of water when the RH is increased. Conversely, the RI would increase towards that of the solute as RH is decreased. Changes in RI can also be indicative of liquid-liquid phase separation (LLPS). Although changes in RI are expected as RH is varied, a significant jump in RH that lasts over a period of time points to the presence of a separate phase in the aerosol particle.[44] Tracking the RI is important in elucidating any physical transformations an aerosol particle may undergo.

The imaginary component of the complex refractive index is associated with absorption. Most organic aerosol particles typically do not absorb light, so absorption is negligible or near to zero at a given wavelength. This would yield a k value of $<10^{-8}$, while an absorbing particle would have a $k > 10^{-4}$.[48] Atmospheric aerosol light absorption is mainly resultant from black carbon in the atmosphere which is known to absorb a large part of the solar spectrum.[16] More recently, researchers have been studying brown carbon compounds that absorb light in a lower wavelength range (visible and near UV).[13] The properties of brown carbon containing aerosol particles are studied in chapter 4.

Aerosol particles in the atmosphere exist as both spherical and non-spherical particles. When dealing with homogeneous and spherical particles of a known diameter and RI, Mie Theory is used to further describe scattering and absorption.[15,49] Mie Theory is an analytical solution of Maxwell's equations for scattering of infinite electromagnetic plane waves from homogeneous and spherical particles.[15,49] Through the decades Mie Theory has been extended to the calculation of scattering and absorption of layered concentric spheres, spheres with spherical inhomogeneities, and agglomeration of spheres.[48] This allows the theory to be applied to fractal-like species (soot) that arise from combustion and are highly absorbing. Absorptive properties are expected to change with RH, tying this property to hygroscopicity. The physical transformations can easily be followed using the changes in optical properties, but this strategy also applies to the chemical transformations that an aerosol particle undergoes.

1.2.3 Chemical Properties

The environment in which atmospheric aerosol exist is incredibly variable and chemical reactions lead to aging and can change the physical and chemical properties of aerosol. Gas-phase oxidants present in the atmosphere can react with volatile organic compounds (VOC) existing in either the gas or particle phase, depending on their volatility. Highly volatile organic compounds will remain in the gas phase while lower volatility species (semi- and intermediate- volatile) exist in both the gas and particle phase. Compounds present in the atmosphere include alcohols, aldehydes, ketones, saturated and unsaturated compounds, as well as aromatics. The volatility of these compounds can be explored to asses whether they will be in the gas or particle phase.

Under dry environmental conditions, an aerosol particle may undergo evaporation depending on its composition. If the aerosol is semi-volatile and pure, the organic will partition into the vapor phase.[9] This will decrease the size of the aerosol particle, but its refractive index will remain constant. If the aerosol particle is composed of multiple components the more volatile organic will partition into the gas phase first and a shift in the refractive index indicates a less volatile organic remains. In a heterogeneous reaction, a gas phase oxidant can interact with a condensed aerosol in different manners. The oxidant can: (i) transport to the surface of the aerosol particle, (ii) be incorporated onto the surface of the aerosol particle, (iii) diffuse into the aerosol particle and react inside the condensed phase. Once the product is formed inside the condensed phase, the product may diffuse out of the condensed phase and desorb from the surface.[9]

A common oxidant in the atmosphere is hydroxyl radicals (•OH) formed through the interaction of ozone with light, as well as through the photodegradation of peroxides and through Criegee chemistry following ozonolysis of unsaturated organic molecules. After formation, hydroxyl radicals will react with any molecule that contains a hydrogen. Once the hydroxyl radical abstracts a hydrogen atom from the VOC, the radical will react with oxygen (O_2) to form a peroxyradical (RO_2). This peroxyradical then has multiple reaction pathways available, as shown in Figure 1.5, including reactions with hydroperoxy radicals (HO_2), NO_x, other peroxyradicals, oxygen, decomposition, or isomerization.[11]

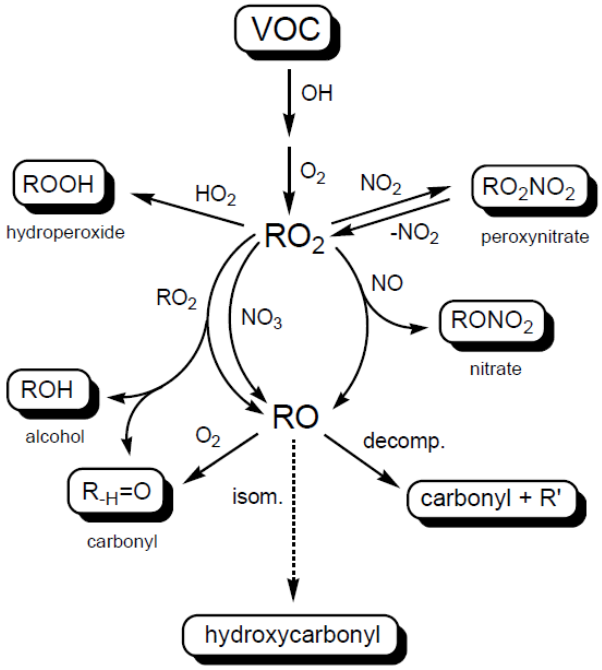

Figure 1.5: Simplified hydroxyl radical oxidation scheme. Figure from Hallquist et al.[11]

Other possible gas-phase oxidants include ozone, which needs a VOC with a double bond like an alkene or aromatic compound, to initiate the reaction or NO_x oxidation pathways which are dominant during nighttime. NO_x oxidation pathways are important for the formation of nitrated aromatic compounds such as nitrophenols, nitroguaiacols, and nitrocatechols. These compounds have strong absorptive properties and are known to be components of brown carbon (BrC). These compounds can undergo oxidative aging, changing their behavior in the atmosphere and physical properties.[50,51]

Another possible pathway incorporates solar radiation and its reaction with aerosol. The solar spectrum spans from about 200 – 2500 nm (UV, Visible, and IR) giving a wide range of available wavelengths.[23] Because radiation energy is inversely proportional to wavelength, lower wavelengths (UV) have sufficient energy to break chemical bonds.

When photolysis occurs, light with enough energy will react with a molecule to break chemical bonds and form products. For photolysis of a molecule, there needs to be light available at a given wavelength, the molecule must absorb light at a given wavelength, and the wavelength of light must have enough energy relative to the bond energy to break the chemical bond.[23] How quickly a compound is photolyzed depends on the photon intensity, the absorption cross section of the molecule, and the quantum yield (probability that photon absorption leads to dissociation).[9] The rate of photolysis has been recently explored and tied to atmospheric processes in clouds and the particle phase. In this study, high NOx toluene SOA was aged by direct photolysis on filters and in aqueous solutions. The SOA contained nitrophenols, a light absorbing species. It was found that photobleaching on the filter (simulating the particle phase) was much slower than in the aqueous phase (simulating cloud processes). They found that the decay of nitrophenol was much quicker in the viscous organic phase than the aqueous phase while SOA composition in the aqueous phase did not change much. This suggested that photodegradation of chromophores was preferred. These findings are important contributions to understanding brown carbon species containing light absorbing chromophore created during wildfires.[52]

These light interactions not only create gas phase oxidants that trigger oxidation reactions, but also react with atmospheric aerosol creating further products. While there are many heterogeneous reactions and photochemical pathways that can evolve the composition of aerosol particles in the atmosphere, the environmental conditions also play an important role in regulating chemical transformations, particularly due to the influence of water on the physical state of particles, which is regulated by the relative humidity.

Understanding the connection between the physical properties and chemical reactivity is important for predicting the lifetime effects of aerosol exposed to the oxidizing environment of the atmosphere. The complexity of aerosol calls for the use of techniques that can probe their various aspects and processes in the atmosphere.

1.3 General Aerosol Methods

While many techniques exist to study atmospheric processes two of the general methods are briefly introduced.

1.3.1 Environmental Chambers

Smog chambers can simulate atmospheric reactions in controlled conditions that mimic those in the natural environment. Smog chambers can be located either outdoors or indoors, yet indoor chambers are not susceptible to unpredictable changes in temperature and relative humidity. Smog chambers generally consist of an enclosed reactor made of an inert component like Teflon film, stainless steel, or quartz. Reactors range in size from < $1m^3$ to > 100 m^3. Other components include an inlet system to inject chemical species, light sources to initiate photochemical reactions, temperature control system to keep the reactor from heating after irradiation, and monitoring system.[53] Things to consider when running chamber experiments are pollutants/contamination in the reactor and wall loss (aerosol settling and depositing on walls).[23] The inlet system will initially inject clean background air into the reactor followed by gas phase species or aerosol. UV lights are commonly used to start photochemical reactions (like producing OH radicals and starting ozonolysis).[53] Reactors are then coupled to monitoring systems such as the aerosol mass spectrometer (AMS), chemical ionization mass spectrometer (CIMS), and scanning mobility particle

sizer (SMPS) to further understand the chemical processes involved and resultant aerosol.[53] These chamber experiments have expanded knowledge in atmospheric reactions like VOC oxidation initiated by OH, O_3, NO_X, etc and recently new particle formation (NPF).[54–57] While environmental chambers have been advantageous in their application, reactions may take multiple hours while NPF tends to occur in a matter of seconds and may also deposit on the reactor walls. To simulate quicker atmospheric reactions, a different approach using flow tube reactors is necessary.

1.3.2 Flow Tube Reactors

The flow tube reactor has been widely used as it can also mimic atmospheric reactions. The main difference between the environmental chamber and the flow tube reactor is that by controlling the inlet concentrations and oxidation conditions an atmospheric oxidation reaction that would occur over several days can take have a residence time of a few minutes in the flow tube reactor.[23,58] This cuts down in particle and gas interactions with instrument walls. Other aerosol processes like new particle formation and heterogeneous reactions on particle surfaces occur between seconds and minutes can be probed by flow tube reactors.[59–62] Using this instrument, other factors like uptake coefficients of vapors on particles and gas-phase kinetics can be studied as well.[58,63,64] Like the environmental chamber, the flow tube reactor comes in many designs which affects the extent of the reaction, residence time, and wall effects.[23,59,65] All flow tube reactors, however, consider the inlet configuration (which determines the initial mixing of components and the concentration profile), the diameter-to-length ratio and body length (which determines the residence time), ways to mix reactants, and how to generate oxidants (light source).[58,59,65]

For example, the oxidative flow reactor (OFR), a type of flow tube reactor, can contain up to 10^{10} OH molecules cm^{-3} which gives the equivalent of hours to weeks' worth of oxidation over the residence time of minutes.[65] Flow tube reactors, like environmental chambers, are coupled to other instruments like CIMS and SMPS to elucidate information about chemical composition and size distribution.[61,64,65]

While both environmental chambers and flow tube reactors are helpful in exploring chemical processes, they provide limited information of the physical characteristics of the aerosol particles, have restricted ability to vary reaction timeframes, and provide only mass-averaged composition for the whole aerosol ensemble. To gain a better understanding of the physical and chemical properties of aerosol particles, single particle methods have been developed.

1.4 Single Particle Techniques

Atmospheric processes are complex and dictate the size, composition, phase, and morphology of aerosol. Oxidation reactions, secondary organic aerosol (SOA) formation, evaporation/condensation, and photochemical processes are influenced by environmental conditions like relative humidity and temperature which can further change the physical and chemical properties of aerosol. While general aerosol techniques provide information on atmospheric reactions, a deeper understanding of the microphysical state of aerosol is needed to holistically understand atmospheric reactions and transformations. For example, the morphology which aerosol adopts will affect its reaction pathway and kinetics. This morphology can also impact the ability to serve as cloud condensation nuclei (CCN). Isolating and studying single aerosol particles will help in unmasking the physical

properties of aerosol that are hidden from general aerosol techniques. The following sections will briefly describe two available experimental techniques used to analyze single aerosol particles through levitation using optical and acoustic methods.

1.4.1 Optical Tweezers

Optical trapping is widely used in several fields like biology, biophysics, and aerosol studies.[44,66,67] This technique is useful because it can trap objects ranging from 1– 10 μm in size (spanning from strands of DNA to small particles). Optical tweezers have been used to study levitated single aerosol particles for extended periods of time with the use of a high powered laser.

Optical Tweezers use a laser beam that is focused through an objective lens onto a particle near the focal point. This point is considered an optical trap and holds the particle in place due to scattering and gradient forces. Scattering forces arise from the radiation pressure of the laser while gradient forces pull the particle towards the focal point.[68–71] This is because photons that make up the laser light carry momentum that is proportional to its energy in the direction of propagation. When the path of laser light is changed, like when it is bent by a particle through reflection and refraction, there is a change in momentum of the laser light. To conserve momentum, the particle must undergo an equal and opposite change in momentum, resulting in force acting on the particle.[68,72] Whispering Gallery Modes (WGMs) that arise from the droplet's interaction with laser light give information about the droplet's size and refractive index, which can in turn provide insight about the droplet's morphology and phase state. This can be used to understand the morphology of secondary organic aerosol (SOA) as explored by Gorkowski *et al.*[44]This study used the

discontinuity in WGMs, size, and refractive index over time to conclude that SOA particles were predominantly core-shelled. This technique has also been used to identify liquid-liquid phase separation (LLPS), partially engulfed and inclusion containing morphology, the evolution of interfacial tension, and the pH of atmospheric aerosol.[44,73] Generally, the continuous interaction with laser light may perturb or cause damage to particles and cannot be used with strongly absorbing particles, therefore other techniques to probe single particles are implemented.

1.4.2 Acoustic Trap

Acoustic levitation provides insight in many fields including biology, pharmacy, and chemistry. This technique is non-destructive and can levitate cells and zebrafish embryos for up to 30 minutes without damage.[74] This makes acoustic levitation advantageous in exploring the properties of soft materials (droplets, foams, emulsion, etc.). The sound fields easily perturb any levitated object, but soft materials can easily and quicky adapt their shape to remain stable while levitated.[75] Acoustic levitation uses the acoustic radiation force created by sound waves that involves a standing wave and potential well of the sound field to trap small objects in a contact-free manner.[75,76] Acoustic waves have frequencies ranging from 1 kHz – 500 MHz leading the trap to levitate droplets ranging from 20 µm – 2 mm.[74,75] While there are several configurations, the most conventional acoustic levitator is the *single axis levitator* made of an emitter and reflector.

Solid and liquid samples are levitated at the potential wells of the sound field. Usually the reflector and/or the emitter is designed concave to improve stability of the levitated droplet.[75] This is because the Bernoulli effect creates instability from acoustic streaming

and the acoustic radiation pressure on the droplet is not uniform. To overcome the non-uniformity, the droplet changes the surface curvature.

This technique is entirely contactless and has been used, in conjunction with microscopy, to study the phase state of organic aerosol. For example, Milsom *et al* studied acoustically levitated oleic acid-sodium oleate particles and probed the physical and chemical changes during ozone and humidity exposure.[77]They found that during humidification the particle enters a core-shell morphology with a disordered liquid-crystalline shell and crystalline core. They also noted that an inert surface layer formed during ozonolysis which led them to conclude that surface active organic species are phase dependent. This technique has also been used to study the transition of saliva droplets to solid aerosol using microscopy as well as the photochemical aging of brown carbon droplets using UV-Vis absorbance measurements.[78,79]

1.4.3 Electrodynamic Balance

As explored in optical tweezers and acoustic traps, a force on the particle is necessary to levitate a particle in place. Another technique, the electrodynamic balance (EDB), uses electric trapping to hold a charged particle in place between a set of electrodes.[12,80] As with optical tweezers and acoustic traps, multiple configurations of an EDB exist which determines the size of particles that specific EDB can probe.[12,80] Typically, an EDB can probe solid and liquid particles ranging from 1 – 100 μm.[12,80] Charged droplets are introduced to the EDB from a droplet-on-demand generator like piezoelectric generator.

Generally, to create droplets a DC pulse voltage is applied to the solution contained at the tip of the generator, causing droplets to be ejected. These droplets can then be

introduced to an EDB through an inductive plate, where they become charged and can be confined in the electric fields of the EDB. The electrodynamic balance (EDB) uses a DC field to counter the gravitational force acting on a charged particle and an AC field to tightly confine the position of a particle.[81] A camera can be used to track the position of a particle where the DC voltage is adjusted through a feedback loop to keep the centralized image of the droplet. A laser can be used to illuminate the particle and light scattering, along with Mie Theory, can determine properties like size and refractive index. This technique has been used to study various properties of aerosol including hygroscopicity, vapor pressure, optical properties, viscosity, and surface tension.[82–86]

Table 1.1. Comparison of presented single particle techniques.

Method	**Size Range / µm**	**Analytical Methods**	**Requirements**	**Advantages**	**Limitations**
Electrodynamic Balance	1 – 10's	Light scattering, Raman, Mass spectrometry, microscopy, electrostatic	Particles must have a net charge	Versatile analysis methods, rapid changes	Charged particles, strong electric fields
Optical Tweezers	5 – 10	Raman, microscopy, light scattering	Spherical particles, non-light absorbing	Strong cavity-enhanced Raman	Sample introduction
Optical Traps	<1 – 10's	Light scattering	Non-light absorbing	Strong cavity-enhanced Raman	Limited analytical methods
Acoustic Traps	10's – 100's	Microscopy, mass spectrometry, light scattering	Large particles	Robust analysis due to large sample	Particle size range

1.5 Overview of Thesis

The electrodynamic balance is used to probe the physical and optical properties of levitated single particles. The following sections will provide a brief overview of each experimental chapter.

1.5.1 Chapter 3: Simultaneous Retrieval of the Size and Refractive Index of Suspended Droplets in a Linear Quadrupole Electrodynamic Balance

In this chapter the application of a broadband light source to illuminate and measure light scattering, in lieu of a laser, was explored. While laser-based methods are used to determine the size, optical properties, and composition of droplets, this is confined to non-absorbing droplets and cannot be applied to droplets that contain photoactive chromophores. The use of a broadband light source with Mie resonance spectroscopy gives information about the droplet size and refractive index (RI), simultaneously. To benchmark the size accuracy, the evaporation of poly(ethylene glycol)s was probed and vapor pressures were compared to literature values. To benchmark the RI, the hygroscopic growth, and deliquescence and efflorescence relative humidities of NaCl were explored. The experimental RIs at these points were compared to literature findings. These data were used to determine the wavelength dependence of the RI of aqueous NaCl using a first-order Cauchy equation to compare to literature data from several techniques. Finally, light absorbing aqueous droplets containing humic acid were explored along with the imaginary component of the RI.

1.5.2 Chapter 4: Hygroscopic Growth, Phase Morphology, and Optical Properties of Model Aqueous Brown Carbon Aerosol

The design and technique developed in Chapters 2 and 3 served as the technique to explore brown carbon (BrC) containing aerosol particles. BrC arise from wildfire emissions and contain light absorbing chromophores which influence the optical scattering properties of particles. BrC may also consist of water-soluble chromophores that are expected to exist in aqueous solution and will exhibit physical properties (size, RI, morphology) that depend on the environmental RH. In this chapter, the RH-dependent properties of 4-nitrocatechol (4-NC) and its mixtures with ammonium sulfate were characterized. The hygroscopic growth of pure 4-NC and its mixtures were determined using mixing rules. The phase transitions in mixed particles were characterized and the relative humidity at the onset of liquid-liquid phase separation was noted. Finally, the imaginary part of the complex refractive index was determined using an effective oscillator model.

1.5.3 Chapter 5: Connecting the Phase State and Volatility of Dicarboxylic Acids at Elevated Temperatures

The design and configuration from Chapter 2 was reconfigured to include heating cartridges to explore vapor partitioning at elevated temperatures. The partitioning of semi-volatile organic molecules between the condensed and vapor phase is necessary for many applications including combustion, industrial spraying and atmospheric processes. Vapor partitioning depends on the molecular interactions and phase state of the condensed material and shows a dependence on temperature. The influence of phase state on the evaporation dynamics of a series of straight-chain dicarboxylic acids across a range of

elevated temperatures (ambient to ~350 K) was probed. Using the rate of evaporation measured from the change in size, the vapor pressure and enthalpy of vaporization were derived. Light scattering data was used to identify the phase state of the particles (crystal or amorphous) allowing vapor equilibrium properties to be connected to a particular state.

1.6 References

(1) Alabsi, W.; Al-Obeidi, F. A.; Polt, R.; Mansour, H. M. Organic Solution Advanced Spray-Dried Microparticulate/Nanoparticulate Dry Powders of Lactomorphin for Respiratory Delivery: Physicochemical Characterization, In Vitro Aerosol Dispersion, and Cellular Studies. *Pharmaceutics* **2020**, *13* (1), 26. https://doi.org/10.3390/pharmaceutics13010026.

(2) Bémer, D.; Fismes, J.; Subra, I.; Blachère, V.; Protois, J.-C. Pesticide Aerosol Characteristics in the Vicinity of an Agricultural Vehicle Cab During Application. *J. Occup. Environ. Hyg.* **2007**, *4* (7), 476–482. https://doi.org/10.1080/15459620701386293.

(3) Mauderly, J. L.; Chow, J. C. Health Effects of Organic Aerosols. *Inhal. Toxicol.* **2008**, *20* (3), 257–288. https://doi.org/10.1080/08958370701866008.

(4) Shiraiwa, M.; Selzle, K.; Pöschl, U. Hazardous Components and Health Effects of Atmospheric Aerosol Particles: Reactive Oxygen Species, Soot, Polycyclic Aromatic Compounds and Allergenic Proteins. *Free Radic. Res.* **2012**, *46* (8), 927–939. https://doi.org/10.3109/10715762.2012.663084.

(5) Pöschl, U.; Shiraiwa, M. Multiphase Chemistry at the Atmosphere–Biosphere Interface Influencing Climate and Public Health in the Anthropocene. *Chem. Rev.* **2015**, *115* (10), 4440–4475. https://doi.org/10.1021/cr500487s.

(6) Ehsanifar, M. Airborne Aerosols Particles and COVID-19 Transition. *Environ. Res.* **2021**, *200*, 111752. https://doi.org/10.1016/j.envres.2021.111752.

(7) Paasonen, P.; Asmi, A.; Petäjä, T.; Kajos, M. K.; Äijälä, M.; Junninen, H.; Holst, T.; Abbatt, J. P. D.; Arneth, A.; Birmili, W.; van der Gon, H. D.; Hamed, A.; Hoffer, A.; Laakso, L.; Laaksonen, A.; Richard Leaitch, W.; Plass-Dülmer, C.; Pryor, S. C.; Räisänen, P.; Swietlicki, E.; Wiedensohler, A.; Worsnop, D. R.; Kerminen, V.-M.; Kulmala, M. Warming-Induced Increase in Aerosol Number Concentration Likely to Moderate Climate Change. *Nat. Geosci.* **2013**, *6* (6), 438–442. https://doi.org/10.1038/ngeo1800.

(8) Pope, F. D.; Braesicke, P.; Grainger, R. G.; Kalberer, M.; Watson, I. M.; Davidson, P. J.; Cox, R. A. Stratospheric Aerosol Particles and Solar-Radiation Management. *Nat. Clim. Change* **2012**, *2* (10), 713–719. https://doi.org/10.1038/nclimate1528.

(9) Jacob, D. J. *Introduction to Atmospheric Chemistry*; Princeton University Press: Princeton, New Jersey, 1999.

(10) George, I. J.; Abbatt, J. P. D. Heterogeneous Oxidation of Atmospheric Aerosol Particles by Gas-Phase Radicals. *Nat. Chem.* **2010**, *2* (9), 713–722. https://doi.org/10.1038/nchem.806.

(11) Hallquist, M.; Wenger, J. C.; Baltensperger, U.; Rudich, Y.; Simpson, D.; Claeys, M.; Dommen, J.; Donahue, N. M.; George, C.; Goldstein, A. H.; Hamilton, J. F.; Herrmann, H.; Hoffmann, T.; Iinuma, Y.; Jang, M.; Jenkin, M. E.; Jimenez, J. L.; Kiendler-Scharr, A.; Maenhaut, W.; McFiggans, G.; Mentel, T. F.; Monod, A.; Prevot, A. S. H.; Seinfeld, J. H.; Surratt, J. D.; Szmigielski, R.; Wildt, J. The Formation, Properties and Impact of Secondary Organic Aerosol: Current and Emerging Issues. *Atmos Chem Phys* **2009**, 82.

(12) Krieger, U. K.; Marcolli, C.; Reid, J. P. Exploring the Complexity of Aerosol Particle Properties and Processes Using Single Particle Techniques. *Chem. Soc. Rev.* **2012**, *41* (19), 6631. https://doi.org/10.1039/c2cs35082c.

(13) Laskin, A.; Laskin, J.; Nizkorodov, S. A. Chemistry of Atmospheric Brown Carbon. *Chem. Rev.* **2015**, *115* (10), 4335–4382. https://doi.org/10.1021/cr5006167.

(14) Lu, Z.; Streets, D. G.; Winijkul, E.; Yan, F.; Chen, Y.; Bond, T. C.; Feng, Y.; Dubey, M. K.; Liu, S.; Pinto, J. P.; Carmichael, G. R. Light Absorption Properties and Radiative Effects of Primary Organic Aerosol Emissions. *Environ. Sci. Technol.* **2015**, *49* (8), 4868–4877. https://doi.org/10.1021/acs.est.5b00211.

(15) Bohren, C. F.; Huffman, D. R. *Absorption and Scattering of Light by Small Particles*; John Wiley and Sons: New York, 1983.

(16) Wu, Y.; Cheng, T.; Zheng, L. Light Absorption of Black Carbon Aerosols Strongly Influenced by Particle Morphology Distribution. *Environ. Res. Lett.* **2020**, *15* (9), 094051. https://doi.org/10.1088/1748-9326/aba2ff.

(17) Stocker, T. F.; Qin, D.; Plattner, G. K.; Tignor, M.; Allen, S. K.; Boschung, J.; Nauels, A.; Xia, Y.; Bex, V.; Midgley, P. M. Climate Change 2013: The Physical Science Basis. Contribution of Working Group I to the Fifth Assessment Report of the Intergovernmental Panel on Climate Change.

(18) Boucher, O. *Atmospheric Aerosols*; Springer Netherlands: Dordrecht, 2015. https://doi.org/10.1007/978-94-017-9649-1.

(19) Colbeck, I.; Lazaridis, M. Aerosols and Environmental Pollution. *Naturwissenschaften* **2010**, *97* (2), 117–131. https://doi.org/10.1007/s00114-009-0594-x.

(20) Lioy, P. J.; Kneip, T. J. Aerosols: Anthropogenic and Natural Sources and Transport: Summary of a Conference. *J. Air Pollut. Control Assoc.* **1980**, *30* (4), 358–361. https://doi.org/10.1080/00022470.1980.10465957.

(21) Tomasi, C.; Lupi, A. Primary and Secondary Sources of Atmospheric Aerosol. In *Atmospheric Aerosols*; Tomasi, C., Fuzzi, S., Kokhanovsky, A., Eds.; Wiley-VCH Verlag GmbH & Co. KGaA: Weinheim, Germany, 2016; pp 1–86. https://doi.org/10.1002/9783527336449.ch1.

(22) Pöschl, U. Atmospheric Aerosols: Composition, Transformation, Climate and Health Effects. *Angew. Chem. Int. Ed.* **2005**, *44* (46), 7520–7540. https://doi.org/10.1002/anie.200501122.

(23) Finlayson-Pitts, B. J.; Pitts, J. N. *Chemistry of the Upper and Lower Atmosphere: Theory, Experiments, and Applications*; Academic Press: San Diego, 2000.

(24) Zhang, Q.; Jimenez, J. L.; Canagaratna, M. R.; Allan, J. D.; Coe, H.; Ulbrich, I.; Alfarra, M. R.; Takami, A.; Middlebrook, A. M.; Sun, Y. L.; Dzepina, K.; Dunlea, E.; Docherty, K.; DeCarlo, P. F.; Salcedo, D.; Onasch, T.; Jayne, J. T.; Miyoshi, T.; Shimono, A.; Hatakeyama, S.; Takegawa, N.; Kondo, Y.; Schneider, J.; Drewnick, F.; Borrmann, S.; Weimer, S.; Demerjian, K.; Williams, P.; Bower, K.; Bahreini, R.; Cottrell, L.; Griffin, R. J.; Rautiainen, J.; Sun, J. Y.; Zhang, Y. M.; Worsnop, D. R. Ubiquity and Dominance of Oxygenated Species in Organic Aerosols in Anthropogenically-Influenced Northern Hemisphere Midlatitudes: UBIQUITY AND DOMINANCE OF OXYGENATED OA. *Geophys. Res. Lett.* **2007**, *34* (13), n/a-n/a. https://doi.org/10.1029/2007GL029979.

(25) Melamed, M. L.; Monks, P. S.; Goldstein, A. H.; Lawrence, M. G.; Jennings, J. The International Global Atmospheric Chemistry (IGAC) Project: Facilitating Atmospheric Chemistry Research for 25 Years. *Anthropocene* **2015**, *12*, 17–28. https://doi.org/10.1016/j.ancene.2015.10.001.

(26) Pilinis, C.; Pandis, S. N.; Seinfeld, J. H. Sensitivity of Direct Climate Forcing by Atmospheric Aerosols to Aerosol Size and Composition. *J. Geophys. Res.* **1995**, *100* (D9), 18739. https://doi.org/10.1029/95JD02119.

(27) Buseck, P. R.; Pósfai, M. Airborne Minerals and Related Aerosol Particles: Effects on Climate and the Environment. *Proc. Natl. Acad. Sci.* **1999**, *96* (7), 3372–3379. https://doi.org/10.1073/pnas.96.7.3372.

(28) Chýlek, P.; Videen, G.; Ngo, D.; Pinnick, R. G.; Klett, J. D. Effect of Black Carbon on the Optical Properties and Climate Forcing of Sulfate Aerosols. *J. Geophys. Res.* **1995**, *100* (D8), 16325. https://doi.org/10.1029/95JD01465.

(29) Andrews, E.; Larson, S. M. Effect of Surfactant Layers on the Size Changes of Aerosol Particles as a Function of Relative Humidity. *Environ. Sci. Technol.* **1993**, *27* (5), 857–865. https://doi.org/10.1021/es00042a007.

(30) Saleh, R.; Marks, M.; Heo, J.; Adams, P. J.; Donahue, N. M.; Robinson, A. L. Contribution of Brown Carbon and Lensing to the Direct Radiative Effect of Carbonaceous Aerosols from Biomass and Biofuel Burning Emissions. *J. Geophys. Res. Atmospheres* **2015**, *120* (19). https://doi.org/10.1002/2015JD023697.

(31) Zhang, Y.; Favez, O.; Canonaco, F.; Liu, D.; Močnik, G.; Amodeo, T.; Sciare, J.; Prévôt, A. S. H.; Gros, V.; Albinet, A. Evidence of Major Secondary Organic Aerosol Contribution to Lensing Effect Black Carbon Absorption Enhancement. *Npj Clim. Atmospheric Sci.* **2018**, *1* (1), 47. https://doi.org/10.1038/s41612-018-0056-2.

(32) Zhao, R.; Lee, A. K. Y.; Huang, L.; Li, X.; Yang, F.; Abbatt, J. P. D. Photochemical Processing of Aqueous Atmospheric Brown Carbon. *Atmospheric Chem. Phys.* **2015**, *15* (11), 6087–6100. https://doi.org/10.5194/acp-15-6087-2015.

(33) Rosenfeld, D.; Sherwood, S.; Wood, R.; Donner, L. Climate Effects of Aerosol-Cloud Interactions. *Science* **2014**, *343* (6169), 379–380. https://doi.org/10.1126/science.1247490.

(34) *Atmospheric Aerosols: Life Cycles and Effects on Air Quality and Climate*; Tomasi, C., Fuzzi, S., Kochanovskij, A. A., Eds.; Wiley series in atmospheric physics and remote sensing; Wiley-VCH Verlag GmbH & Co. KGaA: Weinheim, 2017.

(35) The Southland's War on Smog: Fifty Years of Progress Toward Clean Air (through May 1997). *The Southland's War on Smog: Fifty Years of Progress Toward Clean Air (through May 1997)*.

(36) writer, staff. Essay: From Fires to Pollution, Smog Has Been California's Dark Companion for Centuries. *Los Angeles Times*. online September 14, 2020.

(37) Historical Ozone Air Quality Trend. *Historical Ozone Air Quality Trend*.

(38) David, D. UCR Launches Training for Air Quality, Climate Change Scientists. *The Press-Enterprise*. online March 19, 2022.

(39) Ghori, I. High-Tech Air Quality Research Center Dedicated in Riverside UCR among CARB Partners with Cutting-Edge Research Facility. *UCR News*. online November 19, 2021.

(40) Smith, M. L.; Bertram, A. K.; Martin, S. T. Deliquescence, Efflorescence, and Phase Miscibility of Mixed Particles of Ammonium Sulfate and Isoprene-Derived Secondary Organic Material. *Atmospheric Chem. Phys.* **2012**, *12* (20), 9613–9628. https://doi.org/10.5194/acp-12-9613-2012.

(41) Laskina, O.; Morris, H. S.; Grandquist, J. R.; Qin, Z.; Stone, E. A.; Tivanski, A. V.; Grassian, V. H. Size Matters in the Water Uptake and Hygroscopic Growth of Atmospherically Relevant Multicomponent Aerosol Particles. *J. Phys. Chem. A* **2015**, *119* (19), 4489–4497. https://doi.org/10.1021/jp510268p.

(42) Power, R. M.; Simpson, S. H.; Reid, J. P.; Hudson, A. J. The Transition from Liquid to Solid-like Behaviour in Ultrahigh Viscosity Aerosol Particles. *Chem. Sci.* **2013**, *4* (6), 2597. https://doi.org/10.1039/c3sc50682g.

(43) Marcolli, C.; Krieger, U. K. Relevance of Particle Morphology for Atmospheric Aerosol Processing. *Trends Chem.* **2020**, *2* (1), 1–3. https://doi.org/10.1016/j.trechm.2019.11.008.

(44) Gorkowski, K.; Donahue, N. M.; Sullivan, R. C. Aerosol Optical Tweezers Constrain the Morphology Evolution of Liquid-Liquid Phase-Separated Atmospheric Particles. *Chem* **2020**, *6* (1), 204–220. https://doi.org/10.1016/j.chempr.2019.10.018.

(45) Petters, M. D.; Kreidenweis, S. M. A Single Parameter Representation of Hygroscopic Growth and Cloud Condensation Nucleus Activity. *Atmos Chem Phys* **2007**, 11.

(46) Martin, S. T. Phase Transitions of Aqueous Atmospheric Particles. *Chem. Rev.* **2000**, *100* (9), 3403–3454. https://doi.org/10.1021/cr990034t.

(47) Cappa, C. D.; Lovejoy, E. R.; Ravishankara, A. R. Evidence for Liquid-like and Nonideal Behavior of a Mixture of Organic Aerosol Components. *Proc. Natl. Acad. Sci.* **2008**, *105* (48), 18687–18691. https://doi.org/10.1073/pnas.0802144105.

(48) Moosmüller, H.; Chakrabarty, R. K.; Arnott, W. P. Aerosol Light Absorption and Its Measurement: A Review. *J. Quant. Spectrosc. Radiat. Transf.* **2009**, *110* (11), 844–878. https://doi.org/10.1016/j.jqsrt.2009.02.035.

(49) Horvath, H. Gustav Mie and the Scattering and Absorption of Light by Particles: Historic Developments and Basics. *J. Quant. Spectrosc. Radiat. Transf.* **2009**, *110* (11), 787–799. https://doi.org/10.1016/j.jqsrt.2009.02.022.

(50) Teich, M.; van Pinxteren, D.; Wang, M.; Kecorius, S.; Wang, Z.; Müller, T.; Močnik, G.; Herrmann, H. Contributions of Nitrated Aromatic Compounds to the Light Absorption of Water-Soluble and Particulate Brown Carbon in Different Atmospheric Environments in Germany and China. *Atmospheric Chem. Phys.* **2017**, *17* (3), 1653–1672. https://doi.org/10.5194/acp-17-1653-2017.

(51) Li, X.; Yang, Y.; Liu, S.; Zhao, Q.; Wang, G.; Wang, Y. Light Absorption Properties of Brown Carbon (BrC) in Autumn and Winter in Beijing: Composition, Formation and Contribution of Nitrated Aromatic Compounds. *Atmos. Environ.* **2020**, *223*, 117289. https://doi.org/10.1016/j.atmosenv.2020.117289.

(52) Klodt, A. L.; Adamek, M.; Dibley, M.; Nizkorodov, S. A.; O'Brien, R. E. Effects of the Sample Matrix on the Photobleaching and Photodegradation of Toluene-Derived Secondary Organic Aerosol Compounds. *Atmospheric Chem. Phys.* **2022**, *22* (15), 10155–10171. https://doi.org/10.5194/acp-22-10155-2022.

(53) Chu, B.; Chen, T.; Liu, Y.; Ma, Q.; Mu, Y.; Wang, Y.; Ma, J.; Zhang, P.; Liu, J.; Liu, C.; Gui, H.; Hu, R.; Hu, B.; Wang, X.; Wang, Y.; Liu, J.; Xie, P.; Chen, J.; Liu, Q.; Jiang, J.; Li, J.; He, K.; Liu, W.; Jiang, G.; Hao, J.; He, H. Application of Smog Chambers in Atmospheric Process Studies. *Natl. Sci. Rev.* **2022**, *9* (2), nwab103. https://doi.org/10.1093/nsr/nwab103.

(54) Chen, X.; Hopke, P. K.; Carter, W. P. L. Secondary Organic Aerosol from Ozonolysis of Biogenic Volatile Organic Compounds: Chamber Studies of Particle and Reactive Oxygen Species Formation. *Environ. Sci. Technol.* **2011**, *45* (1), 276–282. https://doi.org/10.1021/es102166c.

(55) Romonosky, D. E.; Li, Y.; Shiraiwa, M.; Laskin, A.; Laskin, J.; Nizkorodov, S. A. Aqueous Photochemistry of Secondary Organic Aerosol of α-Pinene and α-Humulene Oxidized with Ozone, Hydroxyl Radical, and Nitrate Radical. *J. Phys. Chem. A* **2017**, *121* (6), 1298–1309. https://doi.org/10.1021/acs.jpca.6b10900.

(56) Carter, W. P. L.; Pierce, J. A.; Luo, D.; Malkina, I. L. Environmental Chamber Study of Maximum Incremental Reactivities of Volatile Organic Compounds. *Atmos. Environ.* **1995**, *29* (18), 2499–2511. https://doi.org/10.1016/1352-2310(95)00149-S.

(57) He, X.-C.; Tham, Y. J.; Dada, L.; Wang, M.; Finkenzeller, H.; Stolzenburg, D.; Iyer, S.; Simon, M.; Kürten, A.; Shen, J.; Rörup, B.; Rissanen, M.; Schobesberger, S.; Baalbaki, R.; Wang, D. S.; Koenig, T. K.; Jokinen, T.; Sarnela, N.; Beck, L. J.; Almeida, J.; Amanatidis, S.; Amorim, A.; Ataei, F.; Baccarini, A.; Bertozzi, B.; Bianchi, F.; Brilke, S.; Caudillo, L.; Chen, D.; Chiu, R.; Chu, B.; Dias, A.; Ding, A.; Dommen, J.; Duplissy, J.; El Haddad, I.; Gonzalez Carracedo, L.; Granzin, M.; Hansel, A.; Heinritzi, M.; Hofbauer, V.; Junninen, H.; Kangasluoma, J.; Kemppainen, D.; Kim, C.; Kong, W.; Krechmer, J. E.; Kvashin, A.; Laitinen, T.; Lamkaddam, H.; Lee, C. P.; Lehtipalo, K.; Leiminger, M.; Li, Z.; Makhmutov, V.; Manninen, H. E.; Marie, G.; Marten, R.; Mathot, S.; Mauldin, R. L.; Mentler, B.; Möhler, O.; Müller, T.; Nie, W.; Onnela, A.; Petäjä, T.; Pfeifer, J.; Philippov, M.; Ranjithkumar, A.; Saiz-Lopez, A.; Salma, I.; Scholz, W.; Schuchmann, S.; Schulze, B.; Steiner, G.; Stozhkov, Y.; Tauber, C.; Tomé, A.; Thakur, R. C.; Väisänen, O.; Vazquez-Pufleau, M.; Wagner, A. C.; Wang, Y.; Weber, S. K.; Winkler, P. M.; Wu, Y.; Xiao, M.; Yan, C.; Ye, Q.; Ylisirniö, A.; Zauner-Wieczorek, M.; Zha, Q.; Zhou, P.; Flagan, R. C.; Curtius, J.; Baltensperger, U.; Kulmala, M.; Kerminen, V.-M.; Kurtén, T.; Donahue, N. M.; Volkamer, R.; Kirkby, J.; Worsnop, D. R.; Sipilä, M. Role of Iodine Oxoacids in Atmospheric Aerosol Nucleation. *Science* **2021**, *371* (6529), 589–595. https://doi.org/10.1126/science.abe0298.

(58) Huang, Y.; Coggon, M. M.; Zhao, R.; Lignell, H.; Bauer, M. U.; Flagan, R. C.; Seinfeld, J. H. The Caltech Photooxidation Flow Tube Reactor: Design, Fluid Dynamics and Characterization. *Atmospheric Meas. Tech.* **2017**, *10* (3), 839–867. https://doi.org/10.5194/amt-10-839-2017.

(59) Ezell, M. J.; Chen, H.; Arquero, K. D.; Finlayson-Pitts, B. J. Aerosol Fast Flow Reactor for Laboratory Studies of New Particle Formation. *J. Aerosol Sci.* **2014**, *78*, 30–40. https://doi.org/10.1016/j.jaerosci.2014.08.009.

(60) Palm, B. B.; Campuzano-Jost, P.; Ortega, A. M.; Day, D. A.; Kaser, L.; Jud, W.; Karl, T.; Hansel, A.; Hunter, J. F.; Cross, E. S.; Kroll, J. H.; Peng, Z.; Brune, W. H.; Jimenez, J. L. In Situ Secondary Organic Aerosol Formation from Ambient Pine Forest Air Using an Oxidation Flow Reactor. *Atmospheric Chem. Phys.* **2016**, *16* (5), 2943–2970. https://doi.org/10.5194/acp-16-2943-2016.

(61) Leu, M.-T. Laboratory Studies of Interaction between Trace Gases and Sulphuric Acid or Sulphate Aerosols Using Flow-Tube Reactors. *Int. Rev. Phys. Chem.* **2003**, *22* (2), 341–376. https://doi.org/10.1080/0144235031000087282.

(62) Use of a Potential Aerosol Mass (PAM) Flow Reactor for the Measurement of Secondary Organic Aerosol Production from Vehicle Emissions. 40.

(63) Donahue, N. M.; Clarke, J. S.; Demerjian, K. L.; Anderson, J. G. Free-Radical Kinetics at High Pressure: A Mathematical Analysis of the Flow Reactor. *J. Phys. Chem.* **1996**, *100* (14), 5821–5838. https://doi.org/10.1021/jp9525503.

(64) Matthews, P. S. J.; Baeza-Romero, M. T.; Whalley, L. K.; Heard, D. E. Uptake of HO2 Radicals onto Arizona Test Dust Particles Using an Aerosol Flow Tube. *Atmospheric Chem. Phys.* **2014**, *14* (14), 7397–7408. https://doi.org/10.5194/acp-14-7397-2014.

(65) Xu, N.; Collins, D. R. Design and Characterization of a New Oxidation Flow Reactor for Laboratory and Long-Term Ambient Studies. *Atmospheric Meas. Tech.* **2021**, *14* (4), 2891–2906. https://doi.org/10.5194/amt-14-2891-2021.

(66) Ou-Yang, H. D.; Wei, M.-T. Complex Fluids: Probing Mechanical Properties of Biological Systems with Optical Tweezers. *Annu. Rev. Phys. Chem.* **2010**, *61* (1), 421–440. https://doi.org/10.1146/annurev.physchem.012809.103454.

(67) Perkins, T. T. Optical Traps for Single Molecule Biophysics: A Primer. *Laser Photonics Rev.* **2009**, *3* (1–2), 203–220. https://doi.org/10.1002/lpor.200810014.

(68) *Optical Tweezers: Methods and Protocols*; Gennerich, A., Springer Science+Business Media, Eds.; Methods in molecular biology; Humana Press: New York, 2016.

(69) Wang, C.; Pan, Y.-L.; Videen, G. Optical Trapping and Laser-Spectroscopy Measurements of Single Particles in Air: A Review. *Meas. Sci. Technol.* **2021**, *32* (10), 102005. https://doi.org/10.1088/1361-6501/ac0acf.

(70) Gieseler, J.; Gomez-Solano, J. R.; Magazzù, A.; Pérez Castillo, I.; Pérez García, L.; Gironella-Torrent, M.; Viader-Godoy, X.; Ritort, F.; Pesce, G.; Arzola, A. V.; Volke-Sepúlveda, K.; Volpe, G. Optical Tweezers — from Calibration to Applications: A Tutorial. *Adv. Opt. Photonics* **2021**, *13* (1), 74. https://doi.org/10.1364/AOP.394888.

(71) Ashkin, A.; Dziedzic, J. M.; Bjorkholm, J. E.; Chu, S. Observation of a Single-Beam Gradient Force Optical Trap for Dielectric Particles. *Opt. Lett.* **1986**, *11* (5), 288. https://doi.org/10.1364/OL.11.000288.

(72) HongLian, G.; ZhiYuan, L. Optical Tweezers Technique and Its Applications. **2013**, *56* (12), 10.

(73) Sullivan, R. C.; Boyer-Chelmo, H.; Gorkowski, K.; Beydoun, H. Aerosol Optical Tweezers Elucidate the Chemistry, Acidity, Phase Separations, and Morphology of Atmospheric Microdroplets. *Acc. Chem. Res.* **2020**, *53* (11), 2498–2509. https://doi.org/10.1021/acs.accounts.0c00407.

(74) Ozcelik, A.; Rufo, J.; Guo, F.; Gu, Y.; Li, P.; Lata, J.; Huang, T. J. Acoustic Tweezers for the Life Sciences. *Nat. Methods* **2018**, *15* (12), 1021–1028. https://doi.org/10.1038/s41592-018-0222-9.

(75) Zang, D.; Yu, Y.; Chen, Z.; Li, X.; Wu, H.; Geng, X. Acoustic Levitation of Liquid Drops: Dynamics, Manipulation and Phase Transitions. *Adv. Colloid Interface Sci.* **2017**, *243*, 77–85. https://doi.org/10.1016/j.cis.2017.03.003.

(76) Andrade, M. A. B.; Marzo, A.; Adamowski, J. C. Acoustic Levitation in Mid-Air: Recent Advances, Challenges, and Future Perspectives. *Appl. Phys. Lett.* **2020**, *116* (25), 250501. https://doi.org/10.1063/5.0012660.

(77) Milsom, A.; Squires, A. M.; Boswell, J. A.; Terrill, N. J.; Ward, A. D.; Pfrang, C. An Organic Crystalline State in Ageing Atmospheric Aerosol Proxies: Spatially Resolved Structural Changes in Levitated Fatty Acid Particles. *Atmospheric Chem. Phys.* **2021**, *21* (19), 15003–15021. https://doi.org/10.5194/acp-21-15003-2021.

(78) Stiti, M.; Castanet, G.; Corber, A.; Alden, M.; Berrocal, E. Transition from Saliva Droplets to Solid Aerosols in the Context of COVID-19 Spreading. *Environ. Res.* **2022**, *204*, 112072. https://doi.org/10.1016/j.envres.2021.112072.

(79) Jones, S. H.; Friederich, P.; Donaldson, D. J. Photochemical Aging of Levitated Aqueous Brown Carbon Droplets. *ACS Earth Space Chem.* **2021**, *5* (4), 749–754. https://doi.org/10.1021/acsearthspacechem.1c00005.

(80) Reid, J. P. Particle Levitation and Laboratory Scattering. *J. Quant. Spectrosc. Radiat. Transf.* **2009**, *110* (14–16), 1293–1306. https://doi.org/10.1016/j.jqsrt.2009.02.019.

(81) Davies, J. F. Mass, Charge, and Radius of Droplets in a Linear Quadrupole Electrodynamic Balance. *Aerosol Sci. Technol.* **2019**, *53* (3), 309–320. https://doi.org/10.1080/02786826.2018.1559921.

(82) Lee, A. K. Y.; Ling, T. Y.; Chan, C. K. Understanding Hygroscopic Growth and Phase Transformation of Aerosols Using Single Particle Raman Spectroscopy in an Electrodynamic Balance. *Faraday Discuss* **2008**, *137*, 245–263. https://doi.org/10.1039/B704580H.

(83) Krieger, U. K.; Siegrist, F.; Marcolli, C.; Emanuelsson, E. U.; Gøbel, F. M.; Bilde, M.; Marsh, A.; Reid, J. P.; Huisman, A. J.; Riipinen, I.; Hyttinen, N.; Myllys, N.; Kurtén, T.; Bannan, T.; Percival, C. J.; Topping, D. A Reference Data Set for Validating Vapor Pressure Measurement Techniques: Homologous Series of Polyethylene Glycols. *Atmospheric Meas. Tech.* **2018**, *11* (1), 49–63. https://doi.org/10.5194/amt-11-49-2018.

(84) Davis, E. J.; Ravindran, P. Single Particle Light Scattering Measurements Using the Electrodynamic Balance. *Aerosol Sci. Technol.* **1982**, *1* (3), 337–350. https://doi.org/10.1080/02786828208958599.

(85) Song, Y. C.; Haddrell, A. E.; Bzdek, B. R.; Reid, J. P.; Bannan, T.; Topping, D. O.; Percival, C.; Cai, C. Measurements and Predictions of Binary Component Aerosol Particle Viscosity. *J. Phys. Chem. A* **2016**, *120* (41), 8123–8137. https://doi.org/10.1021/acs.jpca.6b07835.

(86) Bzdek, B. R.; Power, R. M.; Simpson, S. H.; Reid, J. P.; Royall, C. P. Precise, Contactless Measurements of the Surface Tension of Picolitre Aerosol Droplets. *Chem. Sci.* **2016**, *7* (1), 274–285. https://doi.org/10.1039/C5SC03184B.

CHAPTER II

Experimental Strategy – Electrodynamic Balance

To fully explore he physical and optical properties of aerosol, it is necessary to maintain the levitated contact-free state of airborne particulate matter. An electrodynamic balance (EDB) can trap and levitate charged single particles using electric fields and allows for a range of spectroscopic probing methods to explore particle properties. The particle will remain suspended and stable in the trap while the forces remain balanced. This chapter will introduce the linear quadrupole EDB (LQ-EDB), which consists of a linear quadrupole electrode configuration, discuss how particles are generated and levitated, and explore spectroscopic analysis methods for particle sizing and measuring optical properties.

2.1. Linear Quadrupole Trap

The principles of the electrodynamic balance (EDB), which uses charge and electric fields to isolate particles, are based on the Millikan oil drop experiment.[1,2] In the Millikan oil drop experiment a charged particle was electrostatically suspended between two electrodes. Advancements have been made to improve the spatial stability of levitated particles, using a DC field to balance the gravitational force and an AC field to locally confine the particle.

Many configurations of the EDB exist and have been used to explore individual aerosol particles. Stability criteria for the particle can be determined using Mathieu's equation which describes the particle motion in an electric field.[3–5] In general, the electric field generated from the AC voltage exerts a force on a confined particle in the vertical and radial directions. These oscillatory forces stabilize the confined particle while an applied DC voltage produces an electrostatic force that balances any net forces on the particle.[3,6,7]

A single particle is stabilized in the trap when the forces acting it are in balance. In the absence of any external forces, other than gravity, the standard force balance equation can be applied to the EDB:

$$mg = \frac{q_1 V_{DC_1} C}{z} \tag{2.1}$$

where m is the mass of the droplet, g is the acceleration due to gravity, q_1 is the charge on the droplet, C is a geometrical constant that accounts for the deviation in electric field from that of an infinite plate electrode and is dependent on the geometrical arrangement of the EDB, z is the distance from the droplet to the electrode, and V_{DC1} is the DC voltage required to balance the gravitational force. Generally, C and q_1 unknown, but are assumed to be fixed for a given droplet at a specific height above the electrode.

Configurations with axisymmetric fields are most popular, like the bi-hyperboloid shaped electrodes (i.e., double ring balance). This configuration generates a static electric field that is used to counter the gravitational force on the particle. Complications arise when trapping the particle. Particle injection is known to be arduous due to a single stability point that needs to match the charge-to-mass ratio and initial velocity vector of the incoming particle.[8] Before trapping, the balance conditions must be close to what is needed to stabilize and confine the entering particle. Once conditions are set, the velocity of the particle entering the trap determines if it will be levitated. If the velocity is too high, the particle will simply pass through the balance, and, if the velocity is too low, the path of the particle path will be changed by the high field gradient outside of the pseudo-potential minimum.[8] The sensitivity of particle trapping and balancing position has led to the use of the linear quadrupole electrodynamic balance (LQ-EDB), which simplifies the initial

particle trapping. In the LQ-EDB, balance conditions for particle confinement are unrelated to the forces of gravity and aerodynamic drag. In addition, the initial velocity of the particle while entering the trap does not affect whether the particle will be stabilized and confined. This is because the particles entering the trap have an initial trajectory that coincides with the central axis of the LQ-EDB. This configuration has been used in several applications.

The LQ-EDB used in this thesis has been adapted from previous experiments, all of which have helped explore the properties of suspended microdroplets.[8,9] The evaporation of single and multicomponent droplets was explored by Hart et al[8] to benchmark the newly built LQ-EDB. They compared computed and experimental light scattering patterns to discern the changing size of the droplet and found the expected linearity between the radius-squared and time and good agreement with modeled and experimental results. This configuration has also served to explore the reaction rate and composition of levitated particles.[10] Jacobs et al[10] coupled their branched quadrupole EDB to a mass spectrometer to explore condensed phase chemical reactions by colliding droplets with different reactants and levitating the merged droplet indefinitely. The composition of levitated droplets was then determined using paper spray mass spectrometry. After using the LQ-EDB to determine the relative mass and density of a particle,[11] it was adapted to explore amorphous phase transitions along with viscosity and diffusion of levitated particles. Richards et al[12] determined the aerosol viscosity of sorbitol and aqueous glucose, identified gel transitions of $MgSO_4$, and explored semi solid gels using a dual balance LQ-EDB with bright field imaging. Generally, the configuration of the LQ-EDB allows for droplets to be easily trapped and levitated indefinitely due to the ease of programming a feedback loop

that uses the balancing DC voltage. This allows for many avenues of exploration into the properties of aerosol droplets to better understand their effects on climate and air quality. The LQ-EDB used in this thesis consisted of four stainless steel rods in a square pattern, as depicted in Figure 2.1.

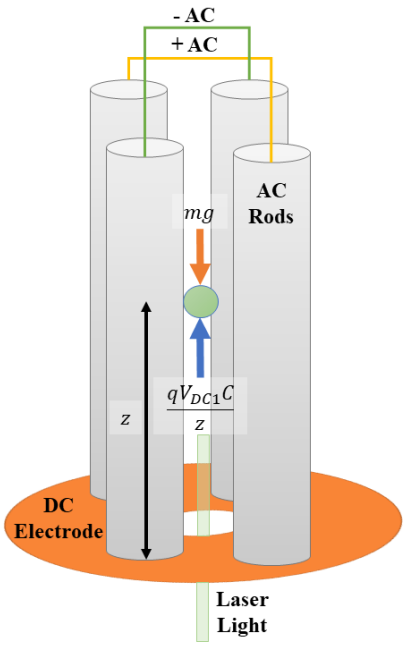

Figure 2.1: Schematic of linear quadrupole electrodynamic balance with opposing AC voltages. Droplet is centrally confined by the resulting pseudo potential well and vertically positioned by the repulsive force from the DC plate.

Each rod had a diameter of 6 mm and length 15 cm and were diagonally separated by 12 mm. Each rod was mounted on an endcap and enclosed inside an aluminum chamber. An alternating current (600 – 1200 V) was applied to diagonal rod pairs. The alternating current created an electric field and pseudo-potential well to centrally confine the charged particle. The configuration of this LQ-EDB allowed for particles in the range of 3 – 20 μm to be easily trapped and suspended for extended periods of time, facilitating the exploration

of the physical and chemical properties of aerosol, such as hygroscopic growth, liquid-liquid phase separation in particles and evaporation of semi-volatile species.

2.2. Droplet Generation and Levitation

A piezoelectric microdroplet dispenser (Microfab MJ-ABP-01) with either a 30 or 50 µm orifice was positioned ~ 25 mm away from the chamber was used to generate droplets ranging from 3 – 20 µm in radius. The concentration of the starting solution determined the equilibrated size of the levitated "dry" droplet. To estimate the size of the levitated droplet, the volume of the "wet" droplet was found using the dispenser droplet radius. Generally, a microdroplet dispenser with a 30 µm orifice produces droplets with a 25 µm radius. After the volume of the "wet" droplet was found, the volume of the "dry" (levitated) particle was found using the calculated dry mass. Once the "wet" droplet was injected into the linear quadrupole electrodynamic balance (LQ-EDB) all excess solvent was evaporated within seconds until the particle equilibrated with its surroundings.

About 12 µL of the starting solution was loaded into the reservoir of the dispenser using a micropipette. A pulse voltage was applied to the microdroplet dispenser causing the pizeoelectric crystal to compress around the solution, as depicted in Figure 2.2.

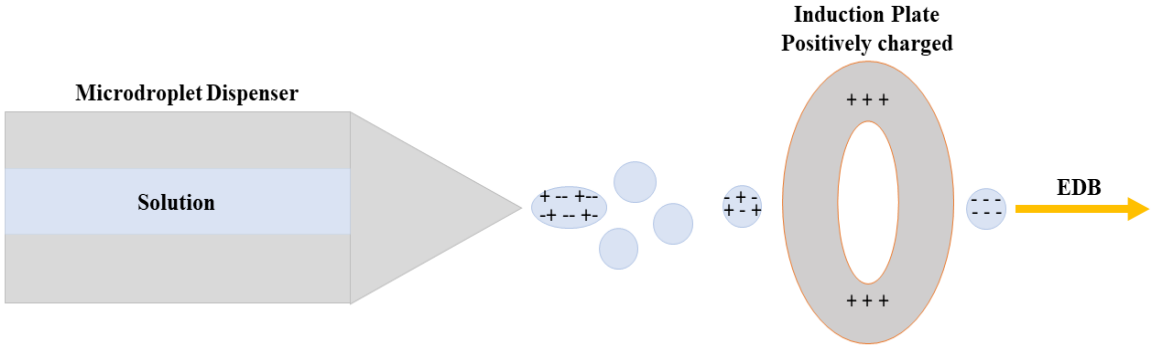

Figure 2.2: Droplets generated by microdroplet dispenser and charged by induction plate.

The compressed solution forms a liquid jet at the tip of the dispenser. An external induction electrode with an applied voltage between 150 – 500 V was positioned ~ 25 mm away from the microdroplet dispenser. Charge separation was induced as the jet of liquid exits the dispenser and breaks down into single droplets that move towards the induction electrode. The droplets enter the LQ-EDB with a net charge in the range 20 – 200 fC, depending on the voltage applied to the induction electrode.[9,11] Once in the LQ-EDB, the droplet becomes centrally confined and if no other forces are acting on the particle, it will fall centrally along the axis of rods due to gravity. A disc electrode, positioned in the center of the chamber, with an applied DC voltage of 30 to 300 V, produces a repulsive electrostatic force on the particle that balances vertically acting forces (gravity and drag) to hold the particle in place, as described by Equation 2.1. If more than one droplet enters the LQ-EDB, the electric polarity imposed on the particles results in trapped particles with similar charge and causes particles to space themselves apart along the central axis, as depicted in Figure 2.3.

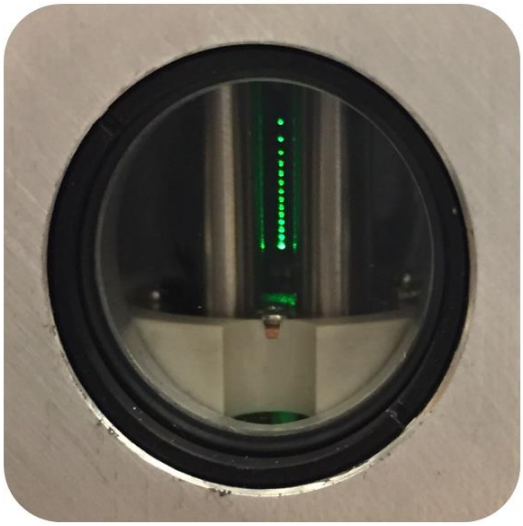

Figure 2.3: Stack of particles suspended in the LQ-EDB. Particle separation due to repulsion. Picture courtesy of Dr. James F. Davies.

Changing the DC voltage changes the vertical position of the particles. The particle was visualized using a CMOS camera and its position was stabilized and maintained using a PID feedback loop initiated through the LabVIEW control software, which adjusted the DC voltage accordingly.

2.2.1 Environmental Control

The environmental condition of the chamber was controlled by the introduction of a mixture of dry and humidified nitrogen at a total flow rate of 200 sccm through the top of the chamber. The resulting relative humidity (RH) was monitored in real time with an RH sensor. The temperature of the chamber was assumed to be that of the laboratory (18 – 22 ^{o}C) but could be monitored using an external temperature probe.

2.2.2 Environmental Monitoring

The deliquescence RH of well characterized salts were used to calibrate the RH probe. Salts are very hygroscopic, meaning they can uptake and lose water easily. Hygroscopic salts have well-defined deliquescence and efflorescence RHs.[13] The efflorescence RH is the point at which the salt exists as a solid crystal with no associated water, while the deliquescence RH is the point at which the solid crystal uptakes water from its surroundings and becomes aqueous. The deliquescence RHs of NaCl, LiCl, and $(NH_4)_2SO_4$ were experimentally determined using solid particles of a specific salt. Each particle was separately exposed to a gradual increase in RH until the deliquescence RH (75.5, 11, and ~80 % RH for NaCl, LiCl, and $(NH_4)_2SO_4$, respectively) was reached.[14,15] The experimental deliquescence RH and RH probe voltage at the deliquescence RH were noted and calibrated against the known deliquescence RHs.

To visualize particles in the chamber, a 532 nm Gem laser with a beam width of ~ 1mm and power ~ 10 mW was used for illumination. Once the particles were trapped and vertically positioned, the laser was turned off and a broadband LED was used to illuminate and stabilize the particle through the duration of an experiment. Either a red (620 – 680 nm) or white (400 – 450; 500 – 680 nm) LED was used to illuminate the particle. A schematic of the LED light path to the LQ-EDB chamber is presented in Figure 2.4.

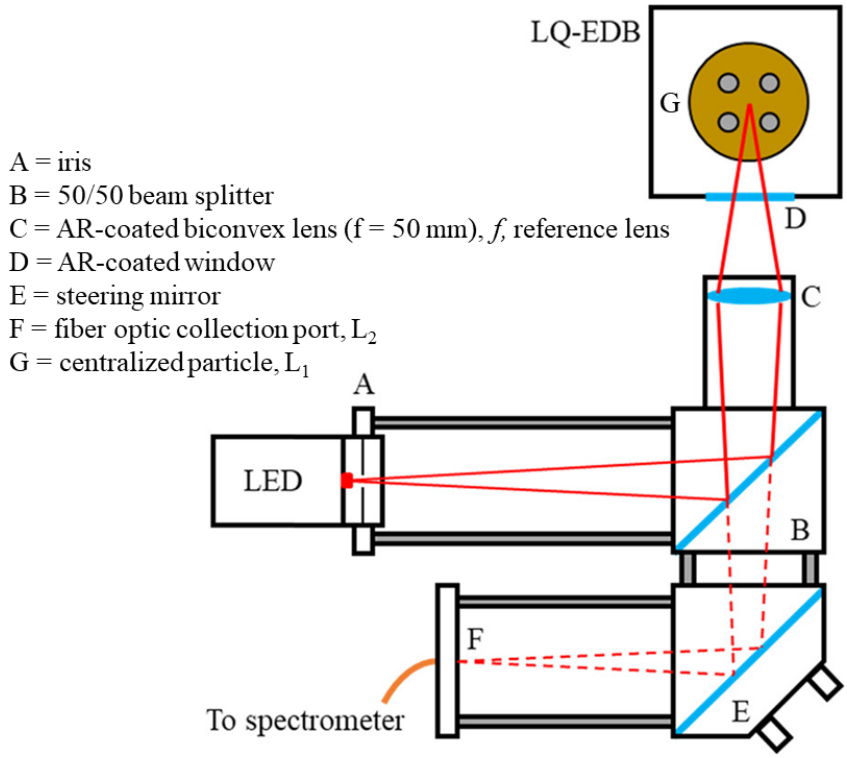

Figure 2.4: Schematic of Mie Resonance Spectroscopy design. Red or White LED is used to illuminate the levitated droplet in the chamber. Figure reproduced from Price et al,[16] with permission.

The light from the LED passes through an iris, A, with a diameter < 1 mm that is positioned ~ 5 mm from the diode, as illustrated in Figure 2.4. The light then passes through a 50:50 beam splitter, B, and the reflected light was focused through with anti-reflective coated biconvex lens, C, with focal length of 50 mm onto the levitated particle. Once the light was focused onto the particle, G, the backscattered light over the angular range of approximately 170 – 190º was collected by lens C, focused through the beam splitter, and guided by a steering mirror, E, into a fiber optic cable, F.

The position of the fiber optic cable was determined based on the position of the suspended particle relative to the lens using the thin lens equation:

$$\frac{1}{f} = \frac{1}{L_1} + \frac{1}{L_2} \tag{2.2}$$

Where *f* is the focal length of the biconvex lens (C, Fig. 4), L_1 is the position of the particle, and L_2 is the position of the fiber optic cable. The collected backscattered light was delivered to the 25 µm entrance slit of a Raman spectrometer (Fergie, Princeton Instruments) configured with 1200 grooves/mm grating positioned for a wavelength range of 560 – 680 nm and resolution of 0.26 nm. The spectrograph was calibrated using emission wavelengths of a neon light source from Princeton Instruments.

2.3. Mie Resonance Spectroscopy

When light interacts with a homogeneous spherical particle, the light can resonate within the optical cavity and is emitted at specific wavelengths. Light can undergo multiple internal reflections in the optical cavity causing light intensity to build up. Light is eventually emitted from the optical cavity at specific wavelengths. The back scattered light from levitated particles was collected and delivered to a spectrometer (Princeton Instruments) with a resolution of 0.26 nm, giving rise to a Mie resonance spectrum, as shown in Figure 2.5. These peaks, or morphology dependent resonances (MDR), arise from either the coupling of inelastic scattered light (Raman) from a laser or from the elastically scattered light produced from external illumination by a broadband light source.[17,18] In Figure 2.5, a red LED (620 – 680 nm) was focused onto the levitated particle and the back

scattered light was collected in the spectrometer and a Mie resonance spectrum was generated.

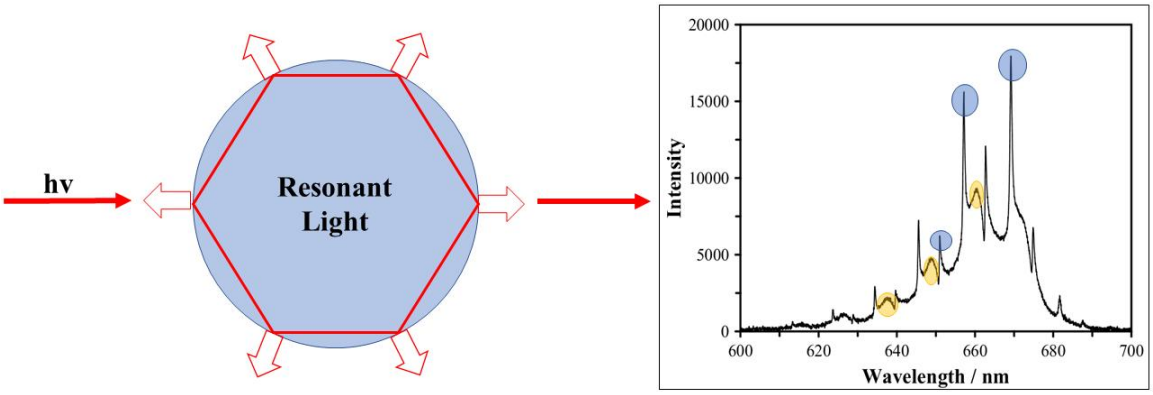

Figure 2.5: Broadband LED interaction with a 5 µm particle. Resulting Mie resonance spectrum contains two mode orders: 2nd (blue) and 3rd (yellow).

The wavelength position of each MDR is characteristic of the size of the particle and its refractive index (RI). The width of the MDR, however, depends on the mode order and light absorbing properties, as described by Mie Theory.[17,19] In a typical spectrum, as in Figure 2.5, MDRs rest on top of the reflected light from the surface of the particle. Each MDR is uniquely described by mode number (*n*), a mode order (*l*), and a polarization of either transverse electric (TE) or transverse magnetic (TM). The mode orders that are observed are dependent on the size of the particle and the depth the light penetrates the particle.[17,18] The spectrum in Figure 2.5 is that of a typical levitated particles (~ 5 µm) which contains second (blue) and third (yellow) order modes. Particles with a larger radius give rise to a spectrum that contains MDRs with higher mode orders. Smaller particles (< 2 µm) contain mostly first mode order MDRs because light resonates close to the surface, resulting in sharp MDRs with widths so narrow they are below the sensitivity of our

spectrometer and cannot be visualized. The full experimental spectrum, however, may also be compared to Mie Theory simulations using the output size and RI in the code from Bohren and Huffman,[20] as shown in Figure 2.6. The experimental spectrum for an ammonium sulfate particle is shown in black, while the simulation using experimental outputs is shown in orange. There is good agreement between the two spectra confirming that the MDRs are 3rd and 4th mode order giving a particle size of ~ 6700 nm and RI of 1.392 at 86 % RH.

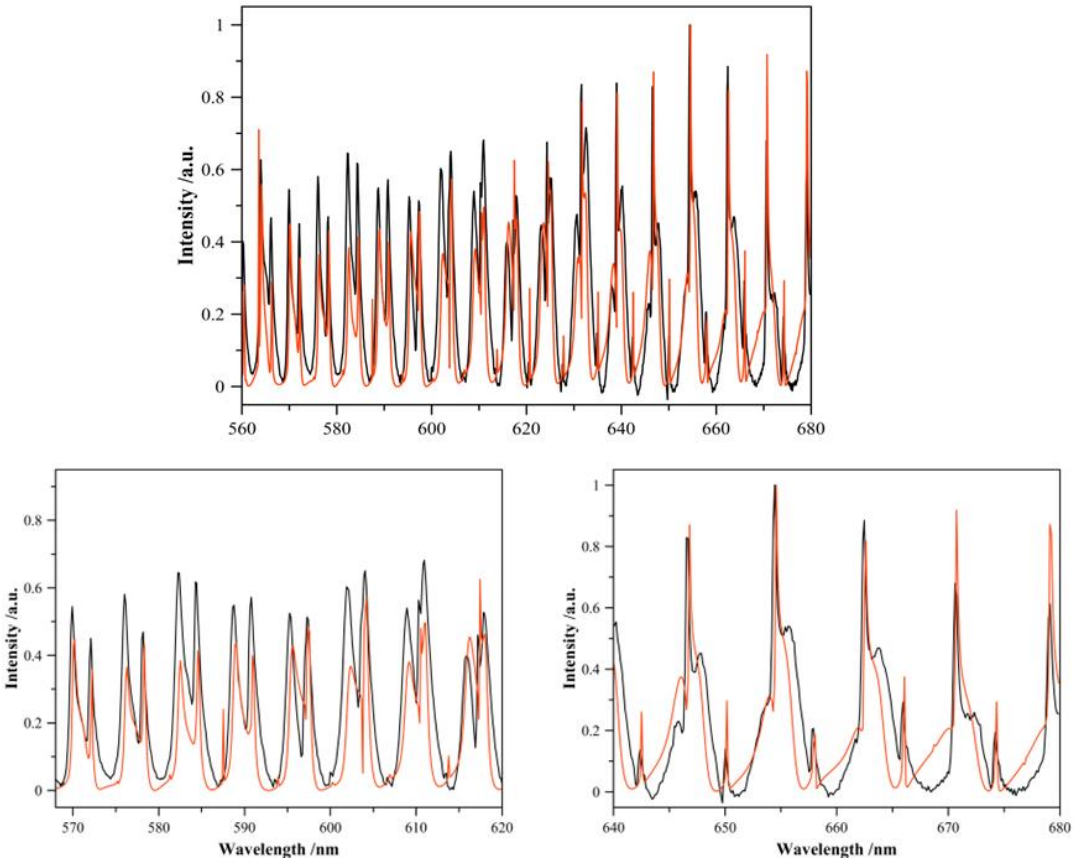

Figure 2.6: Comparison of experimental (black) and simulated (orange) spectra for a pure ammonium sulfate droplet from a white LED (top: 560-680 nm). Zoomed in comparison of simulated and experimental fit on bottom panel (570-620 and 640-680).

2.4 Particle Sizing

Finding the size and refractive index (RI) of a particle using morphology dependent resonances through Mie Theory can be complex and time consuming if a high level of accuracy is desired. In this work the fitting algorithm, MRFIT, was used to simultaneously derive the size and refractive index of a particular particle. This algorithm essentially performs a quick grid search that varies the size and RI, resulting in ideal uncertainties in size and RI of ± 1.1 nm and ± 0.00043, respectively.[18] Applied to our experimental methods using a LQ-EDB with a broadband light source, the experimental uncertainty in size and RI of a particle is ± 5 nm and RI ± 0.002 – 0.005, respectively.

Spectra collected from levitated particles were background subtracted and normalized to a baseline fit over the spectrum. The baseline was generated using a narrow smoothing function based on the Savitzky-Golay filter that enhanced the sharp peaks in the spectrum. Each MDR was found using a built-in peak search algorithm in LabVIEW followed by a polynomial fit to find peak centers. Peak centers were then sent to the MRFIT software developed by Preston and Reid.[18] MRFIT uses the experimental peak centers to find the best-fit of size and wavelength dependent RI from a library of Mie Theory results. The best-fits were found by minimizing the sum of squared residuals between the calculated and experimental resonance peak positions. Dispersion in RI was accounted for using a two-term Cauchy equation:

$$RI(\lambda) = m_0 + \frac{m_1}{\lambda^2} \tag{2.3}$$

where m_0 and m_1 are values found using MRFIT. This equation is an empirical relation describing the wavelength dependence of RI. Figure 2.7 shows how the RI varies for a

typical sample. Results from Cotterell et al[21] used a global fit of the Cauchy dispersion model to show best-fit Cauchy dispersion curves for inorganic compounds commonly found in aerosol. They showed that the RI, at a given RH, increased slightly in shorter wavelengths.

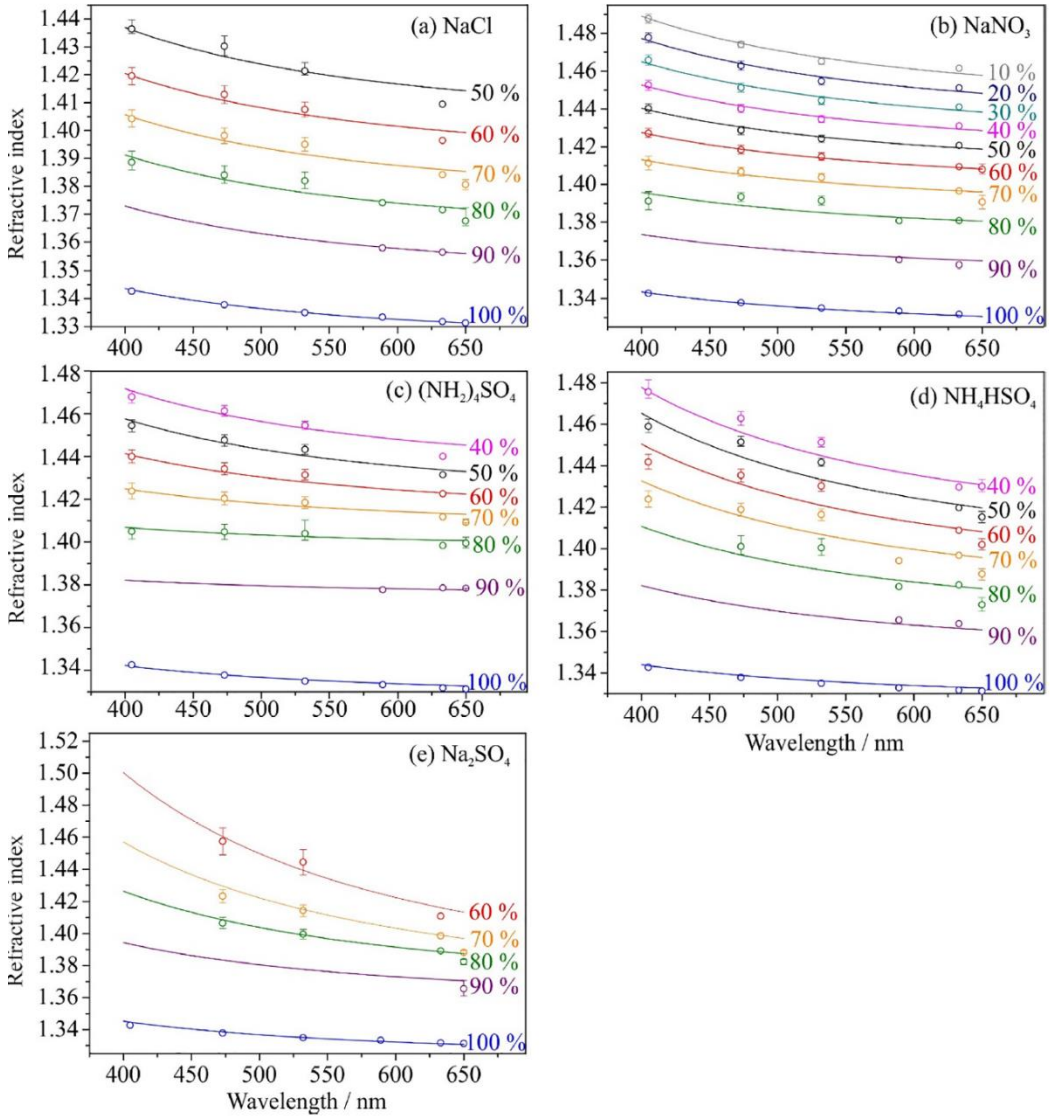

Figure 2.7: Best-fit Cauchy dispersion curves for common atmospheric salts. Figure reproduced from Cotterell et al.[21]

While there are multiple configurations of the EDB, all designs use electric fields to confine and stabilize a particle. Prior to the LQ-EDB, configurations like the double ring balance were difficult to use in that trapping was unpredictable. The LQ-EDB improved the trapping ability and the stability of a suspended particle. The environmental conditions, mainly RH, in this LQ-EDB is controlled by introducing a mixture of dry and humidified nitrogen. Coupled a broadband light source, the LQ-EDB used throughout this thesis is able to determine the size and RI of levitated particles using the sizing algorithm, MRFIT, within ± 5 nm and RI ± 0.002 – 0.005, respectively.[19] This allowed for the exploration of light absorbing particles and semi-volatile species.

2.5 References

(1) Millikan, R. A. XXII. A New Modification of the Cloud Method of Determining the Elementary Electrical Charge and the Most Probable Value of That Charge. Lond. Edinb. Dublin Philos. Mag. J. Sci. **1910**, 19 (110), 209–228. https://doi.org/10.1080/14786440208636795.

(2) Millikan, R. A. The Isolation of an Ion, a Precision Measurement of Its Charge, and the Correction of Stokes's Law. Science **1910**, 32 (822), 436–448. https://doi.org/10.1126/science.32.822.436.

(3) Davis, E. J. A History of Single Aerosol Particle Levitation. Aerosol Sci. Technol. **1997**, 26 (3), 212–254. https://doi.org/10.1080/02786829708965426.

(4) On the Electrodynamic Balance. Proc. R. Soc. Lond. Ser. Math. Phys. Sci. **1992**, 437 (1900), 237–266. https://doi.org/10.1098/rspa.1992.0060.

(5) Zheng, F.; Laucks, M. L.; Davis, E. J. AERODYNAMIC PARTICLE SIZE MEASUREMENT BY ELECTRODYNAMIC OSCILLATION TECHNIQUES. J. Aerosol Sci. **2000**, 31 (10), 1173–1185. https://doi.org/10.1016/S0021-8502(00)00023-9.

(6) Davis, E. J.; Ray, A. K. Single Aerosol Particle Size and Mass Measurements Using an Electrodynamic Balance. J. Colloid Interface Sci. **1980**, 75 (2), 566–576. https://doi.org/10.1016/0021-9797(80)90478-6.

(7) Davis, E. J.; Schweiger, G. The Airborne Microparticle: Its Physics, Chemistry, Optics, and Transport Phenomena; Springer Berlin: Berlin, 2013.

(8) Hart, M. B.; Sivaprakasam, V.; Eversole, J. D.; Johnson, L. J.; Czege, J. Optical Measurements from Single Levitated Particles Using a Linear Electrodynamic Quadrupole Trap. Appl. Opt. **2015**, 54 (31), F174. https://doi.org/10.1364/AO.54.00F174.

(9) Haddrell, A. E.; Davies, J. F.; Yabushita, A.; Reid, J. P. Accounting for Changes in Particle Charge, Dry Mass and Composition Occurring During Studies of Single Levitated Particles. J. Phys. Chem. A **2012**, 116 (40), 9941–9953. https://doi.org/10.1021/jp304920x.

(10) Jacobs, M. I.; Davies, J. F.; Lee, L.; Davis, R. D.; Houle, F.; Wilson, K. R. Exploring Chemistry in Microcompartments Using Guided Droplet Collisions in a Branched Quadrupole Trap Coupled to a Single Droplet, Paper Spray Mass Spectrometer. Anal. Chem. **2017**, 89 (22), 12511–12519. https://doi.org/10.1021/acs.analchem.7b03704.

(11) Davies, J. F. Mass, Charge, and Radius of Droplets in a Linear Quadrupole Electrodynamic Balance. Aerosol Sci. Technol. **2019**, 53 (3), 309–320. https://doi.org/10.1080/02786826.2018.1559921.

(12) Richards, D. S.; Trobaugh, K. L.; Hajek-Herrera, J.; Davis, R. D. Dual-Balance: Electrodynamic Trap as a Microanalytical Tool for Identifying Gel Transitions and Viscous Properties of Levitated Aerosol Particles. Anal. Chem. **2020**, 92 (4), 3086–3094. https://doi.org/10.1021/acs.analchem.9b04487.

(13) Boucher, O. Atmospheric Aerosols; Springer Netherlands: Dordrecht, 2015. https://doi.org/10.1007/978-94-017-9649-1.

(14) Biskos, G.; Malinowski, A.; Russell, L. M.; Buseck, P. R.; Martin, S. T. Nanosize Effect on the Deliquescence and the Efflorescence of Sodium Chloride Particles. Aerosol Sci. Technol. **2006**, 40 (2), 97–106. https://doi.org/10.1080/02786820500484396.

(15) Gao, Y.; Chen, S. B.; Yu, L. E. Efflorescence Relative Humidity for Ammonium Sulfate Particles. J. Phys. Chem. A **2006**, 110 (24), 7602–7608. https://doi.org/10.1021/jp057574g.

(16) Price, C. L.; Bain, A.; Wallace, B. J.; Preston, T. C.; Davies, J. F. Simultaneous Retrieval of the Size and Refractive Index of Suspended Droplets in a Linear Quadrupole Electrodynamic Balance. J. Phys. Chem. A **2020**, 124 (9), 1811–1820. https://doi.org/10.1021/acs.jpca.9b10748.

(17) Bain, A.; Rafferty, A.; Preston, T. C. Determining the Size and Refractive Index of Single Aerosol Particles Using Angular Light Scattering and Mie Resonances. J. Quant. Spectrosc. Radiat. Transf. **2018**, 221, 61–70. https://doi.org/10.1016/j.jqsrt.2018.09.026.

(18) Preston, T. C.; Reid, J. P. Accurate and Efficient Determination of the Radius, Refractive Index, and Dispersion of Weakly Absorbing Spherical Particle Using Whispering Gallery Modes. J. Opt. Soc. Am. B **2013**, 30 (8), 2113. https://doi.org/10.1364/JOSAB.30.002113.

(19) Preston, T. C.; Reid, J. P. Determining the Size and Refractive Index of Microspheres Using the Mode Assignments from Mie Resonances. J Opt Soc Am A 32 (11), 2210–2217.

(20) Bohren, C. F.; Huffman, D. R. Absorption and Scattering of Light by Small Particles; John Wiley and Sons: New York, 1983.

(21) Cotterell, M. I.; Willoughby, R. E.; Bzdek, B. R.; Orr-Ewing, A. J.; Reid, J. P. A Complete Parameterisation of the Relative Humidity and Wavelength Dependence of the Refractive Index of Hygroscopic Inorganic Aerosol Particles. Atmospheric Chem. Phys. **2017**, 17 (16), 9837–9851. https://doi.org/10.5194/acp-17-9837-2017.

CHAPTER III

Simultaneous Retrieval of the Size and Refractive Index of Suspended Droplets in a Linear Quadrupole Electrodynamic Balance

3.1. Introduction

Single particle levitation is a common tool used to study the optical, physical and chemical properties of suspended aerosol droplets.[1–3] Methods using optical traps and electrodynamic balances (EDB's) have been developed to measure hygroscopic growth, chemical reactivity, surface tension, viscosity, refractive index, light absorption coefficients, diffusion coefficients and phase morphology.[4–11] The use of light scattering methods to determine the size of levitated droplets is common.[12–18] However, light scattering from a droplet depends on both its size and complex refractive index (RI), hence optical properties must either be known, estimated or simultaneously measured. Spectroscopic sizing methods have been developed that use the phenomenon of morphology-dependent resonances (MDR's) that appear as peaks at characteristic wavelengths in measured spectra.[1,19] Light at the wavelength that excites these modes is scattered more efficiently and sampling this light with a spectrometer reveals intense enhancements in the spectrum. The wavelength position of an MDR is a sensitive function of the size of the droplet and its RI, while the MDR linewidth will depend on the mode order and the light absorbing properties of the droplet, as described by Mie theory.[20] Spectroscopic approaches allow for the simultaneous retrieval of both size and RI for spherical homogeneous droplets and it has been shown that size, RI and wavelength dispersion properties may be measured with very high precision and accuracy for droplets

from 100's nm to around 10 μm.[13] In addition, recent work has focused on identifying homogeneous, core-shell and partially engulfed phase morphologies through analysis of MDR's.[21,22]

There are several methods that are often employed in order to generate and measure MDR's in suspended droplets. One method, most commonly used in optical tweezers, observes MDR's produced due to coupling of inelastic (Raman) scattered light in the droplet illuminated by the trapping laser.[8,12,23–27] The MDR's appear as stimulated peaks on top of the spontaneously scattered Raman band, typically arising from the OH stretch of water or the CH stretch of organic molecules. The intensity of Raman scattering is very low, and these measurements are only possible due to the high laser fluence on the droplet necessary for optically trapping and the efficient collection of Raman scattered light through the laser focusing objective. Highly sensitive Raman spectrometers are employed and spectra are typically collected with an exposure time of ~1s and <0.1 nm resolution, allowing sharp MDR peaks to be resolved. In samples containing fluorescent molecules, laser illumination produces fluorescence light, at intensities far greater than Raman scattered light, that also result in MDR's in the measured spectrum of a droplet.[28]

An alternative route to producing MDR's in a droplet is via external illumination of the droplet with a broadband light source. Instead of relying on light produced by optical processes within the droplet, in this method light from an LED (or other light source such as a Xenon arc lamp) is focused onto the droplet. Light is reflected from the surface and scattered through the droplet. At wavelengths commensurate with an MDR, light will be scattered more efficiently. A detector placed in the backscatter direction will observe

reflected light from the droplet, with a spectrum characteristic of the illumination source, along with intense scattered peaks corresponding to MDR's – termed the Mie resonance spectrum. This method is more versatile than Raman and fluorescence approaches as any wavelength range may be used and spectroscopically inert samples may be probed. Studies have adopted experimental configuration using narrow (10's nm width) and broadband light sources (100's nm width), with recent work demonstrating that UV illumination may be used to determine the size of sub-micron droplets.[13] Broadband light scattering has been used in both optical traps and electrodynamic balance systems, with its lesser reliance on an efficient illumination or collection interface allowing the approach to be implemented with relative ease.[1,13,14,29–31]

In analyzing the spectral information from these approaches, MDR's are assigned a mode number (n), a mode order (l), and either a transverse electric (TE) or transverse magnetic (TM) polarization. These assignments describe a particular MDR in the spectrum and are uniquely associated with poles in the Mie scattering coefficients and, for a given wavelength, will correspond to a radius and RI. Therefore, either the measured wavelength position of the MDR's or the full spectrum can be compared to predictions from Mie theory in order to ascertain the size and RI combination that best describes the spectrum. Using the algorithms of Preston and Reid, this process can be achieved in real-time during an experiment or in rapid offline analysis of measured data, allowing size, RI and wavelength dispersion properties of non-light absorbing droplets to be determined simultaneously.[25,29,32]

In this work, we describe simultaneous measurements of size and refractive index using MDR's generated in droplets held in a linear quadrupole electrodynamic balance (LQ-EDB). Compared to sizing methods often employed in EDB studies, this approach has much improved precision and accuracy, and allows optical properties to be investigated in the absence of laser illumination. To demonstrate effective retrieval of size when RI is constant (it remains unconstrained in the fitting process), we measure the evaporation rate of a homologous series of ethylene glycol droplets and determine vapor pressures to compare with literature data. We then explore the accuracy and reproducibility of the technique by studying the size and RI of deliquesced NaCl droplets, which have a well-defined solute concentration and known environmental relative humidity (RH) within 0.1%. Through these data we further explore the wavelength and RH-dependence of the RI and compare with literature parameterizations derived from measurements at specific wavelengths. Finally, we explore the imaginary component of the complex refractive index through measurements of broadband light scattering from light-absorbing samples of humic acid sodium salt and NaCl. We discuss the implications of these data for characterizing the light absorbing properties of chromophores found in brown carbon aerosol.

3.2. Experimental Methods

3.2.1. Sample Preparation

The chemicals used in this study were purchased and used without further purification. Evaporation measurements were made for a homologous series of polyethylene glycols (n = 3 – 6): triethylene glycol (≥ 99%, Sigma-Aldrich), tetraethylene glycol (99%, Sigma-

Aldrich), pentaethylene glycol (98%, Sigma-Aldrich), and hexaethylene glycol (97%, Sigma-Aldrich). Hygroscopic growth and deliquescence measurements were performed on droplets containing sodium chloride (≥ 99%, Fisher Chemical). Solutions were prepared at a range of mass concentrations, from 0.5 gL^{-1} to 3 gL^{-1}, in HPLC grade water (Fisher Chemical). The resulting solutions were filtered using a 0.2 µm syringe filter (VWR International) and stored in pre-cleaned glass vials. Light-absorbing sample solutions of humic acid sodium salt (Sigma-Aldrich) and NaCl were prepared in a 1:1 ratio by mass.

To generate droplets, approximately 12 µL of solution was delivered to a microdroplet dispenser (Microfab MJ-ABP-01, 30 µm orifice). A voltage pulse (up to 30 V and 30 µs duration) was applied to the dispenser to eject a single droplet on the order of 25 µm in radius into the trapping region of a linear quadrupole electrodynamic balance (LQ-EDB) for levitation. Following evaporation of excess solvent water, a final droplet size on the order of 5 µm remained.

3.2.2. Droplet Levitation

A LQ-EDB is used to trap and levitate droplets (from ~ 1 µm to 10's µm in size) in a controlled environmental chamber using electric fields. The technique has been previously discussed and a brief summary will be presented.[18,33–35] The LQ-EDB setup consists of four parallel stainless-steel rods with an AC voltage applied in a quadrupole configuration. The resulting oscillating electric field confines a charged droplet along the axis of the rods. The rods are mounted on end caps and enclosed in an aluminum chamber. An induction electrode (at 200 – 500 V) mounted external to the chamber is used to give droplets a net charge as they emerge from the orifice of the microdroplet dispenser. The droplet, with a

charge of 50 – 200 fC,[18,35] travels horizontally through the rods and becomes confined along the central axis of the LQ-EDB. If no other forces are acting on the droplet, it will fall freely along the axis of the rods due to gravity. A disc electrode with an applied DC voltage (30 – 300 V) positioned in the center of the chamber produces a repulsive electrostatic force on the droplet that balances vertically acting forces (gravity and drag) to hold the droplet in place.

In this work, the environmental conditions of the droplet were controlled by the introduction of a mixture of dry and humidified nitrogen at a total flow rate of 200 sccm into the top of the chamber. The RH in the chamber was monitored using a RH sensor (Honeywell, HIH-4602-L series) located on the gas flow inlet to the chamber. The sensor was calibrated using the deliquescence RH of sodium chloride and lithium chloride particles. For this calibration, solids particles of NaCl and LiCl were separately exposed to a slowly increasing RH approaching their deliquescence RH (75.5% and 11% for NaCl and LiCl, respectively).[36] At the deliquescence RH, water uptake by the particle leads to formation of a spherical aqueous droplet, with clear indicators in the light scattering pattern. The RH probe voltage at this point was noted and calibrated against the known deliquescence RH. The temperature was maintained at ambient and laboratory temperature was monitored using an external temperature probe (Sensor Push). In the experiments reported here, the temperature was in the range of 18 – 22 °C.

The gas flow through the chamber was exhausted through an open port at the bottom of the chamber, which also allows laser light to pass upwards through the chamber to illuminate the droplet. The trapped droplet is illuminated using a 532 nm laser (Laser

Quantum Gem) with a 1 mm beam width, operating at a power of around 50 mW. The laser light scattering from the droplet was recorded with a CMOS camera (Thorlabs DCC1545) and used to stabilize the droplet position by varying the DC voltage in a PID feedback loop initiated through the LabVIEW control software. For droplets that exhibit slow mass variations with time, a feedback loop is not necessary and levitation at a fixed position is achieved without laser illumination.

3.2.3. Mie Resonance Spectroscopy

Mie resonance spectra were obtained from levitated droplets by illumination with a broadband LED and detected using a Raman spectrometer (FERGIE, Princeton Instruments). A schematic of the setup is shown in Figure 3.1. Mie resonance methods using the algorithm of Preston and Reid[25] have been used to simultaneously probe the size and wavelength-dependent RI (RI(λ)) of droplets in several optically levitated systems.[1,14,29] However, while Mie resonance spectroscopy has been performed on droplets in an EDB,[1,37,38] the simultaneous detection of size and RI(λ) has not been demonstrated until now.

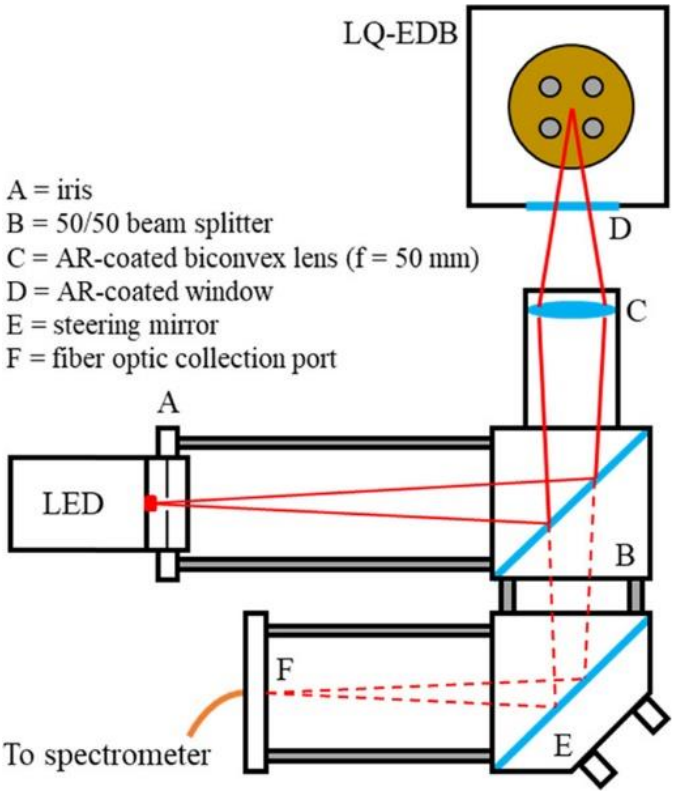

Figure 3.1: Light from an LED (Thorlabs MCWHL5 – white, or M660L4 – red) passes through an iris with diameter <1 mm positioned ~5 mm from the diode. A beam splitter reflects 50% of the incident light through an AR-coated biconvex lens (C, f = 50 mm) and into the LQ-EDB chamber through an AR coated window. The light is focused at around 75 mm from lens C onto the droplet held in the trap. Backscattered light from the droplet follows the same optical path, focused by lens C and passing through the beam splitter, reflecting off a steering mirror and brought to focus at the inlet to a fiber optic. Additional reflections and transmissions are omitted for clarity.

A red LED (620-680 nm, Thorlabs M660L4) was used to illuminate the droplet for evaporation measurements, while a white LED (400-450 nm; 500-680 nm, color temperature of 6500 K, Thorlabs MCWHL5) was used to illuminate the droplet during deliquescence and hygroscopic measurements. The light is unpolarized in both illumination scenarios. As discussed later, the wider wavelength range associated with the white LED improves the determination of RI(λ). An iris was used to aperture the light from the LED (Figure 3.1A), which was reflected off a 50:50 beam splitter and focused by an AR-coated biconvex lens (C, f = 50 mm). The divergent light was focused through an AR

coated window into the chamber to a point around 70 mm from the lens to illuminate the droplet. The configuration in Figure 3.1 was found to be optimal for illuminating the droplet and resolving its backscattered signal against background reflections. Backscattered light over the angular range 170 – 190˚ was collected from the droplet by lens C, focused through the beam splitter and guided, using a steering mirror, into a fiber optic cable (200 µm core). The axial position of the fiber optic cable was estimated based on the position of the droplet relative to the lens using the thin lens equation:

$$\frac{1}{f} = \frac{1}{L_1} + \frac{1}{L_2} \tag{3.1}$$

where f is the focal length of the lens (50 mm), L_1 is the position of the droplet (70 mm), and L_2 is the position of the fiber optic cable. Based on equation 1, the fiber optic was placed approximately 175 mm from the droplet and its position subsequently optimized.

A 20-stranded fiber optic cable (each strand with a 25 µm core diameter) delivered the light to the 25 µm entrance slit of the Raman spectrometer configured with a 1200 groove/mm grating positioned for a wavelength range of 560-680 nm. The resolution of the spectrometer was about 0.26 nm and spectra were collected with a 1 s exposure time. The spectrograph was calibrated in this wavelength range using the emission wavelengths of a neon light source (Princeton Instruments).

3.2.4. Spectra Analysis and Sizing

Following data collection, spectra were processed by background-subtraction and normalization to a baseline fit over the spectrum. The baseline was generated from either a narrow smoothing function based on the Savitzky-Golay filter, to improve the identification of sharp peaks in the spectrum, or broadband smoothing, used to also identify

broader peaks. Each MDR in the spectra was then found using the built-in peak search algorithm in LabVIEW followed by a polynomial fit to the identified peaks to accurately find the centers.

The MDR wavelengths were then delivered to the MRFIT[25] software, which determines the radius and wavelength-dependent refractive index of best-fit through the method of least squares (minimizing the sum of squared-residuals between the calculated and experimental resonance peak positions). This provides the best fit of size, RI, and dispersion for the droplet.[25,29] The dispersion in the RI was accounted for using a two-term Cauchy equation:

$$RI(\lambda) = m_0 + \frac{m_1}{\lambda^2} \tag{3.2}$$

where m_0 and m_1 are values determined using MRFIT. RI values reported in this work are given for a wavelength of 589 nm unless otherwise stated.

3.2.5. Influence of LED Illumination Intensity

To verify that the droplet is not significantly perturbed due to heating by LED illumination, a sample of containing equal parts NaCl and NaHA was sampled over a range of supply current to the LED, from 0.2A to 1.2A. This varies the light intensity by a factor of ~6 and the resulting Mie resonance spectra were observed (Figure 3.2). Despite the large change in illumination intensity, very little change in the spectrum was observed, indicating the extent of heating does not significantly perturb the liquid-vapor equilibrium of water and no change in size occurs. This is in stark contrast to the effect of laser illumination at 532 nm, which results in a large change in the spectrum for even low power unfocused laser light.

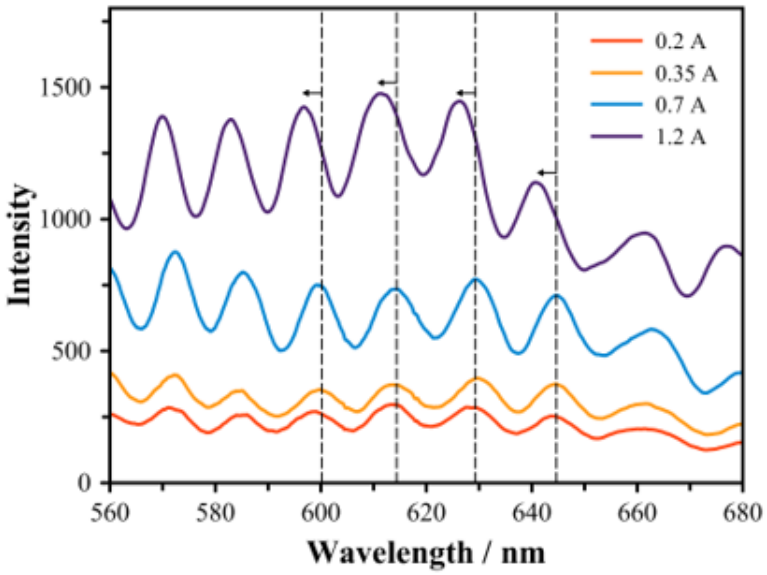

Figure 3.2: A droplet containing equal parts NaCl and NaHA at 75% RH was exposed to increasing intensity of light from the white LED illumination source, as represented by the illumination current. Very little change in the (unnormalized) spectrum was observed indicating no significant heating of the droplet. The arrows show a small shift in peak position at 1.2 A, however this is attributed to small changes in the RH in the chamber rather than heating of the droplet.

3.2.6. Spectral Range of Deliquescence Measurements

Figure 3.3(A-E) shows the spectra used in the analysis of the deliquescence of NaCl droplets detailed in Table 3.1. The shaded regions indicate the range that was used in the sizing analysis, chosen due to the possibility for unambiguous identification of pairs of TE and TM modes in a given mode order and number. Other parts of the spectrum show sharp peaks atop broader peaks, and this can cause complications in the peak fitting process leading to a greater level of uncertainty in the results.

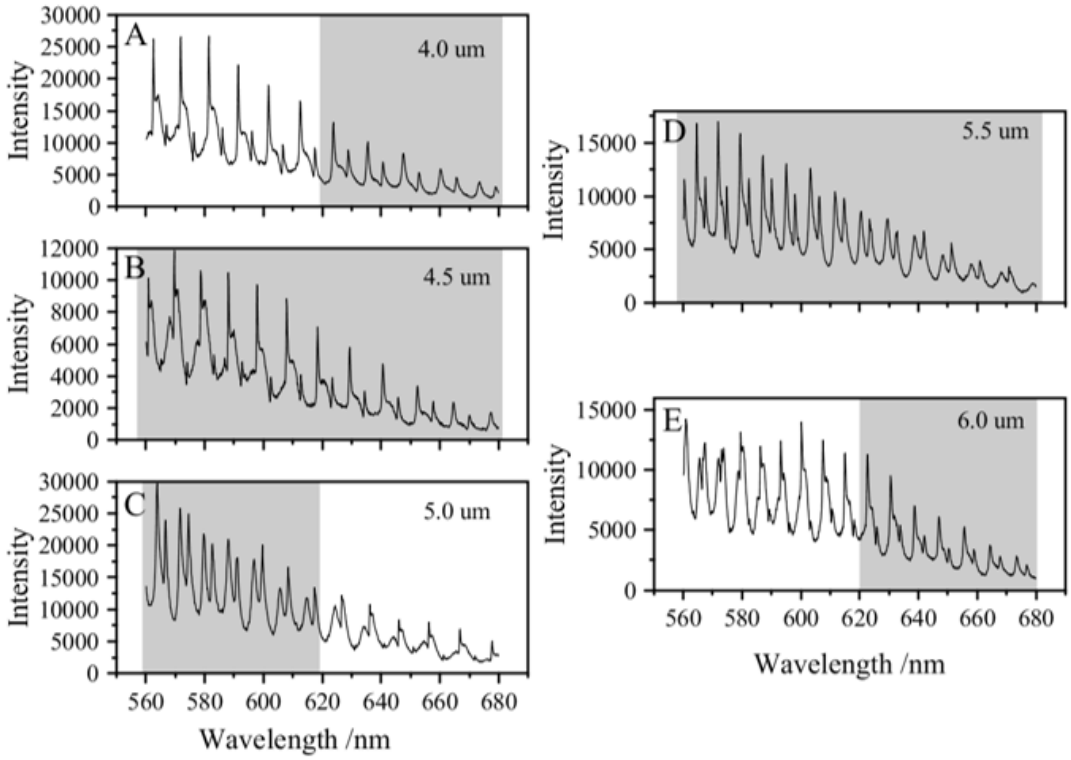

Figure 3.3: Mie resonance spectra for NaCl(aq) droplets at the deliquescence RH, indicating the wavelength range used in the fitting process. The results are shown in Table 3.1.

3.3. Results and Discussion

3.3.1. Single Component Evaporation of Homologous Series of Glycols

Measurements on the evaporation of single component organic droplets were made using the LQ-EDB. The size of the droplet was measured over time using Mie resonance spectroscopy in order to determine the vapor pressure from the evaporation rate. The RI was also determined using the Mie resonance method. The compounds studied were tri-, tetra-, penta-, and hexaethylene glycol and both their RI and resulting vapor pressure were compared to literature values. This study did not include ethylene glycol or diethylene glycol since both compounds evaporate rapidly upon entering the chamber due to their high vapor pressure.

Experiments were performed under dry conditions to ensure that the gas phase pressure of the evaporating glycol is zero and eliminate the potential for fluctuations in RH that might lead to reversible water uptake. In Figure 3.4A, we show the RI of pentaethylene glycol measured during the evaporation of a ~5300 nm droplet over 2000 s. The RI remained constant over the course of the experiment, indicating a pure single component droplet. The experimental RI was measured to be about 0.007 higher than the literature values (~1.462 at 25 ˚C) reported by Mori,[39] Wohlfarth et al.[40] and Gallaugher and Hibbert.[41] The size evolution of the pentaethylene glycol droplet is shown in Figure 3.4B and a representative comparison of the measured spectra with a simulation using Mie theory, using the parameters derived from MRFIT, is shown in 3.4C.

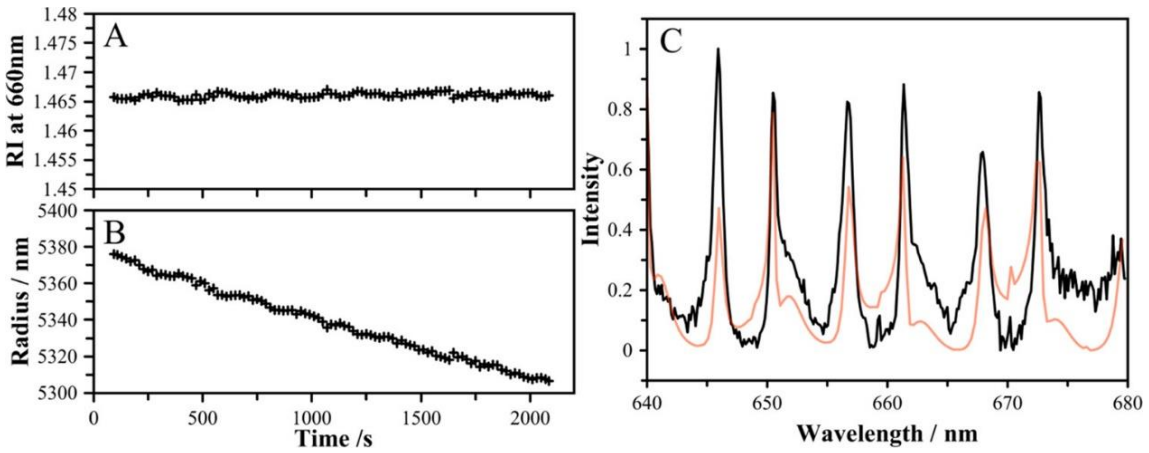

Figure 3.4: (A) The RI of pentaethylene glycol determined from a ~5500 nm droplet evaporating under dry conditions in the LQ-EDB illuminated with the deep red LED. (B) The corresponding radius of the droplet determined using MRFIT. (C) A comparison of the experimental Mie resonance spectrum (black) to the best-fit prediction (light red) using the input variables derived from MRFIT.

To determine the vapor pressure, we must determine the evaporation rate, in this case defined as the slope of the radius-squared with time, as shown in Figure 3.5A for the evaporation of a pentaethylene glycol droplet. Under isothermal conditions, the mass flux of component *i* in an arbitrary droplet may be related to the vapor pressure according to:

$$\frac{dm_i}{dt} = \frac{4\pi a M_i D_i}{RT}\left(p_{i,\infty} - p_{i,a}\right) \tag{3.3}$$

where m_i is the mass of species *i* in the droplet, *a* is the radius, M_i is the molecular mass of *i*, D_i is the gas phase diffusion coefficient of *i* (taken from Krieger et al.[42]), *R* is the gas constant, *T* is the temperature, $p_{i,\infty}$ is the environmental partial pressure of *i*, and $p_{i,a}$ is the partial pressure of *i* at the surface of the droplet. For a single component, this expression may be simplified and re-framed using the evaporation rate according to:

$$\frac{da^2}{dt} = -\frac{2MDp_{sat}}{\rho RT} \tag{3.4}$$

where ρ is the density of the droplet, also taken from Krieger el al.[42], p_{sat} is the vapor pressure, and the *i* subscript is omitted from other terms. Using equation 3.4, we determined the vapor pressure from the experimental evaporation rates and compare these to those reported by Krieger et al. in Figure 3.5B. The results from this work underpredict the vapor pressure compared to the literature values, which is likely due to the difference in temperature at which the measurements were taken. Experiments were performed at a laboratory temperature of approximately 294 K, while literature values are reported at 298 K. To account for this difference, the Clausius-Clapeyron equation was used to find the vapor pressure at 298 K, resulting in vapor pressures slightly higher than the literature values. The enthalpy of vaporization was taken from Krieger et al.[42] The temperature in the lab was not fixed, and fluctuations of 1-2 K are common that could affect these

temperature corrections, leading to uncertainties. For example, when correcting the vapor pressure for pentaethylene glycol with a temperature of 296 K using the Clausius-Clapeyron equation, the literature and experimental vapor pressures are brought to agreement. Thus, while there is some uncertainty in our data due to temperature (which may be up to ±7% due to a ±2 K variation in temperature), we are in agreement with the literature values within the range of temperatures typically encountered over the course of an experiment.

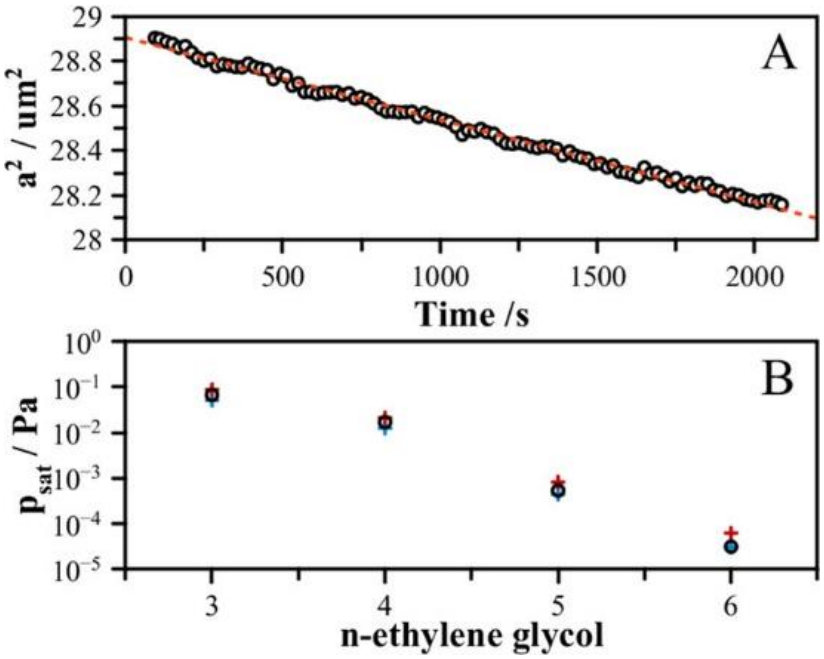

Figure 3.5: (A) The change in radius-squared over time for a pentaethylene glycol droplet. A linear fit to these data (red dash line) reveal an evaporation rate of -3.67×10^{-4} μm^2 s^{-1}. The evaporation rate was used to calculate the vapor pressures according to Equation 3.4. (B) Literature values[42] at 298 K (black circles) are compared to the vapor pressure at the experiment temperature (blue crosses) and the temperature-corrected vapor pressure (red crosses) using the Clausius-Clapeyron equation, as described in the text.

During these measurements, it was consistently observed that for the longer chain glycols, there is a period of more rapid evaporation in the initial period of the measurement. This is shown in Figure 3.6A for a droplet of hexaethylene glycol. There are two phases of

evaporation, the first of which (0 - 5000 s) is attributed to either the slow evaporation of water or a shorter chain glycol and the second of which (>5000 s) is assumed to arise from the evaporation of the pure organic compound. Initial loss of water following the introduction of the droplet is observed to occur within a few seconds and, in the absence of diffusion limitations due to high viscosity affecting the rate of evaporation, it would be expected that there is no residual water in the droplet after this time. Following this initial loss of water (not measured), the droplet loses around 9% of its mass during the first 5000 s. If this were due to water, then a measurable change in RI would be expected on the order of 0.01 based on a simple mass fraction analysis. However, this is not observed and the RI only changes by around 0.003, which is on the order of the precision of the measurement (Figure 3.6B). Thus, we conclude that the initial rapid loss of mass is dominated by organic contaminants present in the glycol, such as shorter chain glycol species. These effects do not affect the calculation of the vapor pressure as the droplet is measured over sufficiently long periods to ensure single component evaporation when determining the evaporation rate.

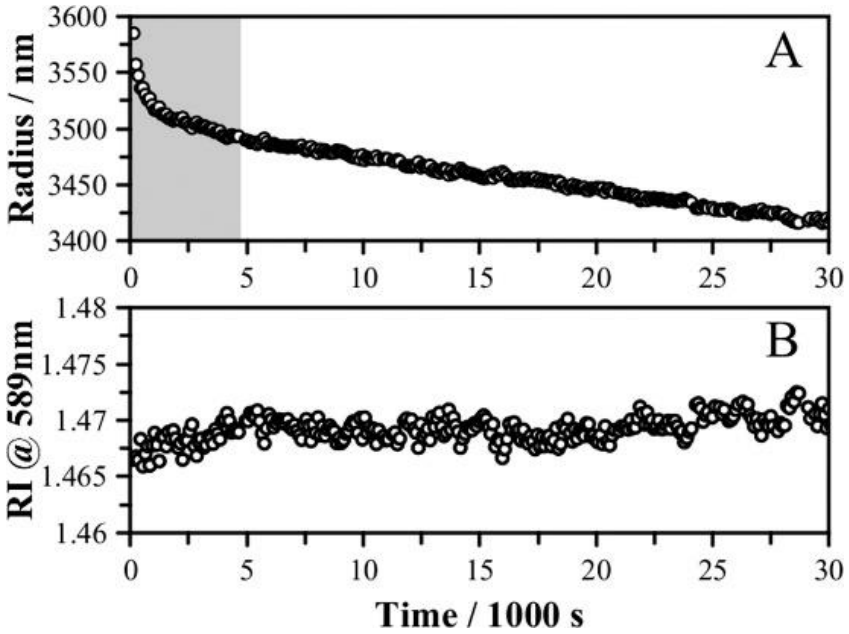

Figure 3.6: (A) Evaporation of a hexaethylene glycol droplet exhibiting two evaporation regimes, as described in the text. The rapid evaporation observed in the first 5000 s is shown in the gray shaded region. (B) The RI was observed to change over time, with a small increase observed in the initial 5000 s before a constant value was approached for the remainder of the measurement.

3.3.2. Aqueous Inorganic Droplets at Fixed RH

Single component n-ethylene glycol droplets provide a sample with a fixed RI and evolving size, and we have shown that these may be effectively measured using the Mie resonance approach. In the case of a hygroscopic droplet exposed to a high RH, the size and RI will be a function of the amount of solute and associated water. The RH can be measured using capacitance probes; however, these typically exhibit an uncertainty in the range of 1 – 3%, which can be significant. In order to benchmark the Mie resonance method further, we performed measurements on NaCl droplets at their deliquescence RH. First, we confine aqueous NaCl droplets at high RH in the LQ-EDB and then lowered the RH to efflorescence the sample and form solid NaCl particles. The RH was then increased slowly to around 75.5% RH where the particle will absorb water from the vapor phase and

deliquesce to once again form an aqueous droplet. By raising the RH in the chamber slowly, the RH experienced by the droplet is maintained at its deliquescence RH for up to a minute after water uptake, allowing the Mie resonance spectra to be measured under well-defined conditions.

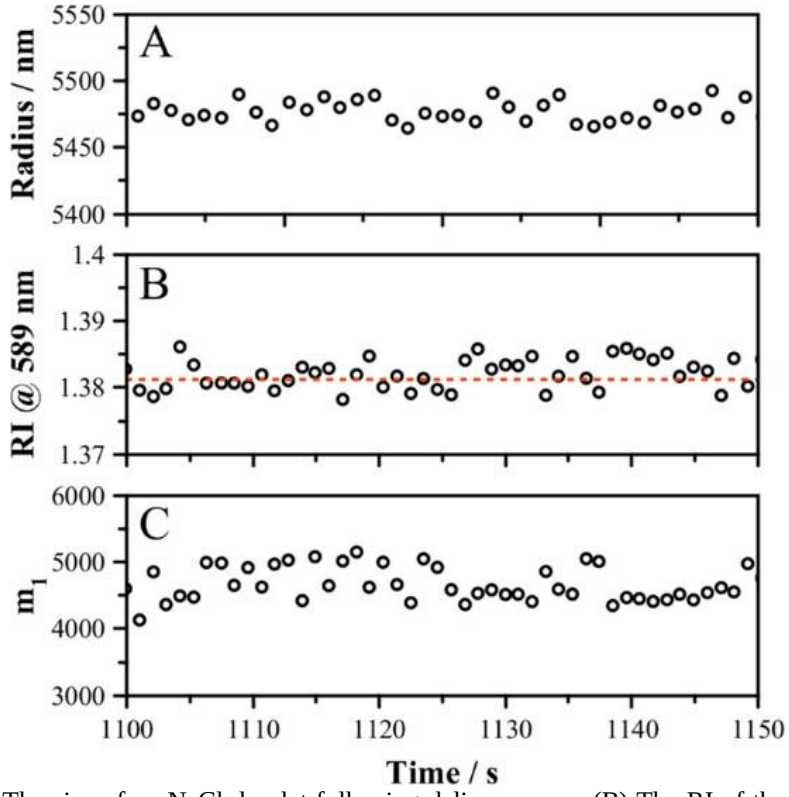

Figure 3.7: (A) The size of an NaCl droplet following deliquescence. (B) The RI of the droplet just after deliquescence. The reported value from the literature is shown by the red-dash line.[43] (C) The dispersion parameter (m1) in the Cauchy equation (Equation 3.2) for the droplet following deliquescence.

For these experiments, a white LED was used to produce a spectrum over a wider range of wavelengths (560 – 680 nm). Figure 3.7 shows the radius, RI at 589 nm, and wavelength dispersion of an NaCl droplet immediately after deliquescence. Figure 3.7A shows the radius across ~50 s of data, with points collected at 1 Hz, exhibiting an average of 5476 nm and a standard deviation of 8 nm. Figure 3.7B shows the RI determined at 589 nm, with

an average of 1.382 and a standard deviation of 0.002. The literature RI at the deliquescence point of NaCl is 1.381, according to the parameterization of Cotterell et al.,[43] which compares well with our experimental observations. Figure 3.7C shows the dispersion term (m_1) in the RI after deliquescence, with an average value of 4670 nm^{-2} and a standard deviation of 250 nm^{-2}.

Since a broader wavelength range was implemented for these measurements, there are more MDR peaks supplied to the MRFIT algorithm. However, due to the resolution of spectrometer, it is sometimes challenging to distinguish the precise location of a peak as resonances from multiple mode orders may be overlapping. For this reason, only peaks from a mode order corresponding to the sharpest peaks were used, and the wavelength range was selected to aid in the assignment of these sharp peaks. The appropriate wavelength ranges were chosen depending on the size and RI combination and are indicated in Figure 3.3. Table 3.1 shows data for deliquesced NaCl droplets across several sizes. Four measurements were taken at each size and the reported error represents the average standard deviation in the scatter of the data for all four trials. Firstly, we note that the RI for each size droplet is within the uncertainty, and thus report (as expected) that there is no size dependency to the RI at the deliquescence RH. Table 3.1 shows the wavelength range and mode orders that were used to size droplets. Despite the choice of wavelength range, the results are consistent within the quoted ranges of uncertainty.

Table 3.1. Measurements were performed on NaCl(aq) droplets over a range of sizes.

Radius / nm	StDev / nm	RI @ 589 nm	StDev	λ range / nm	Modes used
4230	2	1.386	0.001	620-680	2^{nd} & 3^{rd}
4410	8	1.385	0.002	560-680	2^{nd} &3^{rd}
5120	14	1.382	0.003	560-620	2^{nd} & 3^{rd}
5490	12	1.382	0.006	560-680	2^{nd}& 3^{rd}
6200	6	1.384	0.001	620-680	3^{rd}

3.3.3. Hygroscopic Growth and the Wavelength-Dependence of RI

The variation in droplet size and solute concentration with RH due to hygroscopic growth leads to a change in the RI. Here, we report the variation of the RI with the RH, as shown in Figure 3.8A between an RH of ~55% and 90%. The droplet was held at each RH for 10 minutes and increments of 10% in RH were imposed. The data points represent the average of the data for both the increasing and decreasing RH direction and were taken from the time over which the RH was stable at each set point. The RH was measured using a capacitance probe and exhibits an error of ±2%. The RI decreases with increasing RH as the droplet becomes more dilute, tending towards an RI of 1.333 (for pure water) at 100% RH. The predicted trend in RI as a function of RH from the Cotterell et al.[43] parameterization and the oscillator model of Bain et al.[44] are shown for comparison. (Note that the parameterization from Cotterell et al. is an empirical model, while the oscillator model from Bain et al. models the far-UV molecular transitions that give rise the refractive index in the visible region for molecules that do not strongly absorb in this region.) There is generally good agreement across the range within the uncertainty of the measurements, however there is a notable deviation from the oscillator model at low RH. In addition, we

compare to the experimental observations reported by Bain et al. using a similar light scattering method in a counter-propagating optical trap. We observe close agreement to the Cotterell parameterization at low (~55%) and high RH (>80%) but observe deviations towards a larger RI around 60-80% RH. These discrepancies likely arise from uncertainties in the RH probes, which are known to exhibit some non-linearity in their response versus RH.

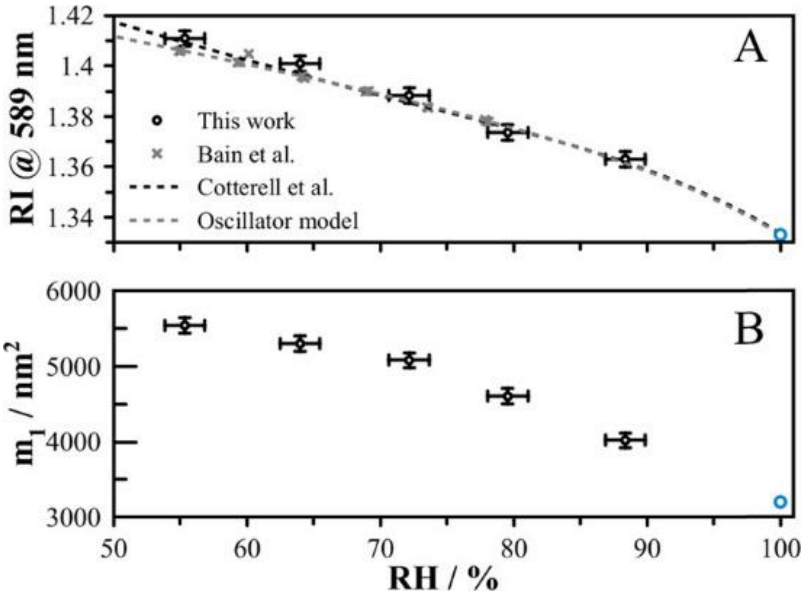

Figure 3.8: (A) The wavelength dependence of the RI of NaCl as a function of RH (black points) compared to the predictions of Cotterell et al. (black dash line) and the oscillator model of Bain et al.[44]. Experimental points from Bain et al.[44] are shown as gray crosses. Others sources of literature data (CRC Handbook and Millard and Seaver[45]) follow the Cotterell trend at sub-saturated RH (>75% RH) and are not shown explicitly for clarity. The y-error bars of ±0.003 account for the standard deviation in the RI for a typical measurement while the x-errors bar show the uncertainty in the RH from the probes. The value for pure water is shown in blue at 100% RH. (B) The dispersion term (m_1) as a function of RH shows a clear trajectory towards the value of ~3200 nm^2 determined for pure water (blue point) shown at 100% RH.

Figure 3.8B shows the measured dispersion coefficient (m_1) as a function of RH. The wide wavelength range (560 – 680 nm) allows the change in m_1 to be readily resolved, and shows a decrease with increasing RH. The dispersion coefficient for water using the Cauchy equation to first order is 3200 nm^2,[46] consistent with the trend of our data towards 100%

RH. These data are tabulated in Table 3.2. Using these values, the wavelength-dependence of the RI across the range of measured RH may be compared with the multi-dimensional parameterization (i.e. RI as a function of RH and wavelength) of Cotterell et al. and Bain et al. Figure 3.9A depicts the RI as a function of wavelength at different RHs, showing the expected curve based on measured Cauchy parameters (dashed line) compared with the prediction from Cotterell et al., shown as a shaded range to account for the ± 2% uncertainty in RH in our measurements. Figure 3.9B shows the equivalent plot using the oscillator model predictions of Bain et al. The data points at 589 nm show the uncertainty in our measured values at a fixed wavelength and reflect the uncertainty range associated with our Cauchy extrapolation. It is clear from these data that while there are some deviations, the measured data agree with the literature within the range of uncertainties for these experiments.

Table 3.2. RI properties of NaCl(aq) as a function of RH.

RH / %	**RI @ 589**	**Dispersion (m_1) / nm^2**
55	1.411	5539
64	1.401	5296
72	1.388	5077
80	1.373	4600
88	1.363	4019

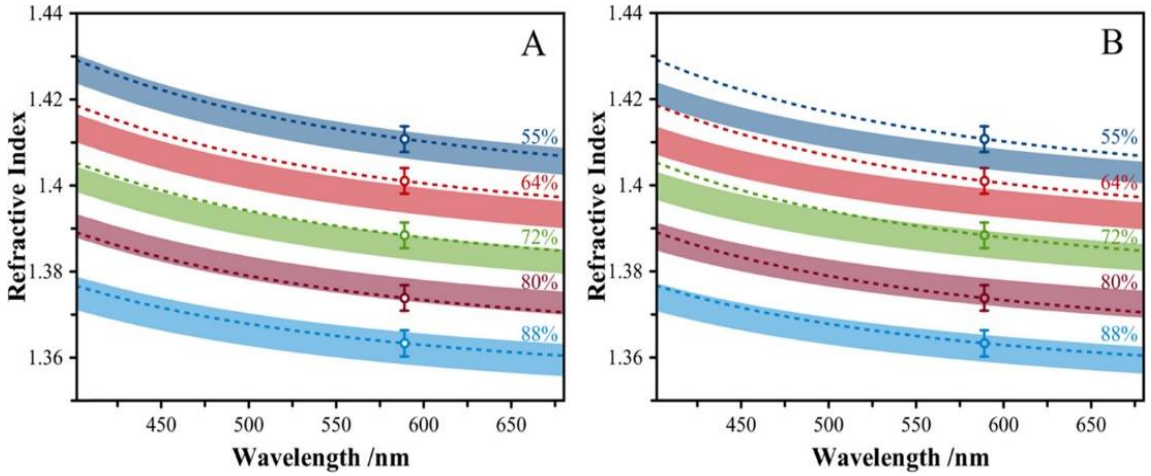

Figure 3.9: (A) The wavelength-dependence of the RI of NaCl for a range of RH conditions. The shaded region shows the model prediction from Cotterell et al. and depicts the range of RI associated with a ±2 % uncertainty in RH. Data points show the measured RI at 589 nm and include representative errors bars. The m_0 and m_1 values determined experimentally were used to predict the wavelength-dependence using the Cauchy equation (Equation 3.2) extrapolated to 400 nm (dash lines). (B) Figure details as per Figure 3.9A, with shaded region derived from the oscillator model fit of Bain et al.[44]

3.3.4. Light Absorbing Aerosol Droplets

The Mie resonance technique has been shown to be capable of measuring the size and wavelength-dependent RI in evaporating single component droplets and hygroscopic samples over a range of RH conditions. These samples contain only species that do not strongly absorb visible light. Recent studies have shown that Mie resonance spectroscopy may also reveal the absorption coefficient of droplets containing light-absorbing material.[8,25,47,48] In order to further test the LQ-EDB setup, humic acid sodium salt (NaHA), a strongly absorbing species, was chosen to explore the effect of absorbance on the Mie resonance spectrum. Figure 3.10 illustrates the preliminary results of these experiments. Figure 3.10A shows the Mie resonance spectrum of an aqueous NaCl droplet in which the MDR peaks are sharp and well-defined. These resonance positions can be fitted, as discussed above, in order to determine the size and RI of the particle. Figure 3.10B shows

a spectrum of a particle containing both NaCl and NaHA, normalized against the LED spectrum and scaled between 0 and 1. Both spectra were collected at an RH of approximately 75%. When NaHA is present in the sample the sharp Mie resonances become broadened and the scattering intensity decreases, resulting in a poorer signal to noise ratio than was observed in panel A. These broad features cannot be fit using resonance positions. A simulated spectrum for a sphere of radius 5432 nm, real part of the RI = $1.47+3425/\lambda^2 + 1.25x10^{-8}/\lambda^4$ and imaginary part of the RI = 0.011 is shown for comparison (the imaginary part of the RI is proportional to the product of the molar attenuation coefficient, the molar concentration and the wavelength). The measured and simulated spectrum are compared between 560-680 nm and show good agreement in terms of both the feature positions and their linewidths, as well as the general trend towards decreasing scattering intensity from long to short wavelengths. When compared to simulations with a smaller imaginary RI of 0.003, we begin to see fine structure in the spectrum that is not observed experimentally. This places a lower bound on the value of the imaginary RI. When comparing to a larger value of the imaginary RI of 0.025, we see little change in the structure of the spectrum, indicating that resolving values of the imaginary RI above this may be challenging. While the positions of the features do not change when increasing the imaginary part of the RI from 0.011 to 0.025, the shape of the background does. Using correlation analysis in a full spectrum fit routine may allow for better precision in determining the imaginary part of the RI. Indeed, it may become necessary to utilize the intensity of the scattered signal to further constrain the level of absorption for more strongly absorbing samples. This would require the signal be

normalized against an external standard, such as a non-absorbing droplet sampled under the same illumination conditions.

To verify that the droplet does not experience significant heating under LED illumination, measurements were made across a range of illumination intensity for the mixed NaCl and NaHA particle at 75% RH. The sample is aqueous under these conditions and any heating would result in a change in the liquid-vapor equilibration of water and a corresponding change in the spectrum. However, as shown in Figure 3.2, no significant change in the spectral shape was observed when the illumination current was increased from 0.2 A to 1.2 A, indicating for these samples there is minimal heating.

Overall, the combination of LQ-EDB levitation and broadband light scattering shows promise for the investigation of species that absorb visible light. However, more work is required to develop algorithms for spectral fitting in order to simultaneously determine (i) the size, (ii) the wavelength-dependent real part of the RI and (iii) the wavelength-dependent imaginary part of the RI for strongly absorbing particles.

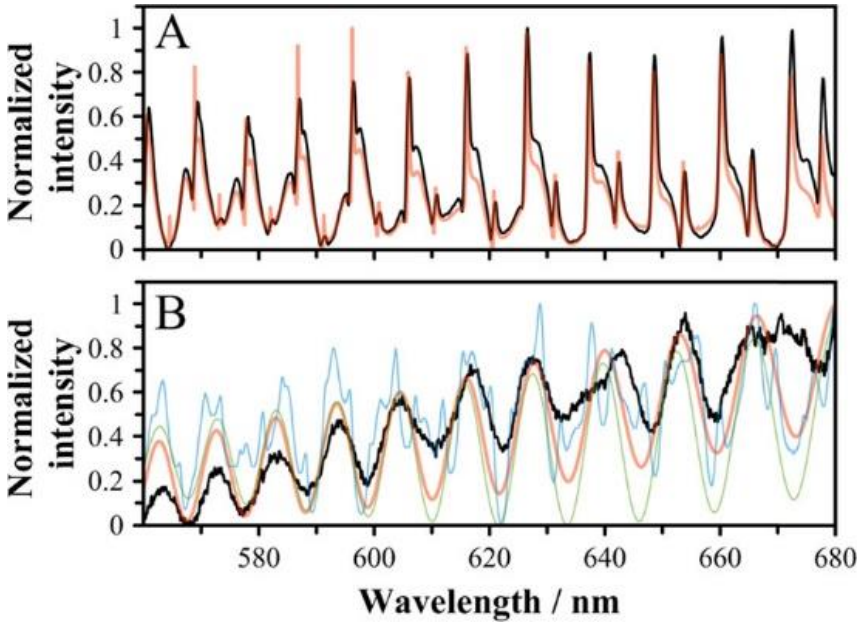

Figure 3.10: (A) Broadband Mie resonance spectrum of an NaCl droplet at 75% RH along with the best-fit simulated spectrum with radius 4571 nm and real part of the RI 1.365+4200/ λ^2 (light red). All 2nd and 3rd order modes seen in the experiment are reproduced by the simulation, while 1st order modes are omitted in the simulation for clarity. (B) A similarly sized droplet of NaCl and NaHA, showing significant broadening of the peaks and a loss of fine structure. Simulated spectrum shown in light red for a sphere of radius 5432 nm, real part of the RI = $1.47+3425/\lambda^2+1.25\text{x}10^{-8}/\lambda^4$ and imaginary part of the RI = 0.011. Light blue shows an imaginary RI of 0.003 and light green a value of 0.025.

3.4. Conclusions

In this work we demonstrate the accurate retrieval of droplet size and refractive index using Mie resonance spectroscopy applied to single droplets levitated in an LQ-EDB. Although Mie resonance spectroscopy is much more commonly used in optical-based traps, there are advantages to applying this method to electrodynamically confined droplets in an EDB. The dynamic range of droplet size spans from 10's μm to sub- μm, the composition can be well controlled using droplet-on-demand methods, and laser-based probing is not necessary, allowing light-sensitive samples to be studied.

The advantage of Mie resonance spectroscopy over typical laser-light scattering approach comes from the ability to simultaneously determine size, RI and wavelength-

dispersion with high accuracy. For non-absorbing samples, we can determine the radius to within ±0.1% (approximately ±10 nm), the RI to within ±0.2% (approximately ±0.003), and the first-order dispersion term to within ±5% (approximately ±200 nm^2). The precision we achieve is slightly less than the optimal precision of the method (±2 nm in radius and ±0.05% in RI[19]) due to the finite resolution to which the modes are detected, but compares favorably with a range of other methods for determining RI in droplets.[49] When using a broadband light source, the entire wavelength-dependence of the RI may be measured for a sample in a single experiment, facilitating a broad exploration of the dependence of refractive index on RH, temperature and chemical environment. In particular, illumination into the UV/vis spectral range will provide optical properties relevant for the interactions of tropospheric and stratospheric aerosol with solar radiation.

We have further demonstrated that Mie resonance spectroscopy may be applied to sample droplets containing light-absorbing species. Due to the lack of laser illumination, these methods do not significantly perturb the physical state due to sample heating, allowing the physical and chemical characteristics of light-absorbing samples to be explored. Preliminary measurements also show that there is sufficient information available in the Mie resonance spectrum to quantify size and both the real and imaginary parts of the RI for light-absorbing samples, but further work is necessary to fully constrain the accuracy of the method. Many key physicochemical properties of aerosol, which are routinely measured in non-absorbing samples using levitation-based methods, are not available for aerosol containing light-absorbing compounds. This work demonstrates that these systems may be effectively explored using the combination of methods presented

here, allowing a molecularly-resolved insight into the properties of light-absorbing components of the atmosphere, such as brown carbon.

3.5. References

(1) Zardini, A. A.; Krieger, U. K.; Marcolli, C. White Light Mie Resonance Spectroscopy Used to Measure Very Low Vapor Pressures of Substances in Aqueous Solution Aerosol Particles. *Opt. Express* **2006**, *14* (15), 6951. https://doi.org/10.1364/OE.14.006951.

(2) Bzdek, B. R.; Reid, J. P. Perspective: Aerosol Microphysics: From Molecules to the Chemical Physics of Aerosols. *J. Chem. Phys.* **2017**, *147* (22), 220901. https://doi.org/10.1063/1.5002641.

(3) Krieger, U. K.; Marcolli, C.; Reid, J. P. Exploring the Complexity of Aerosol Particle Properties and Processes Using Single Particle Techniques. *Chem. Soc. Rev.* **2012**, *41* (19), 6631. https://doi.org/10.1039/c2cs35082c.

(4) Cotterell, M. I.; Mason, B. J.; Carruthers, A. E.; Walker, J. S.; Orr-Ewing, A. J.; Reid, J. P. Measurements of the Evaporation and Hygroscopic Response of Single Fine-Mode Aerosol Particles Using a Bessel Beam Optical Trap. *Phys Chem Chem Phys* **2014**, *16* (5), 2118–2128. https://doi.org/10.1039/C3CP54368D.

(5) Lee, A. K. Y.; Chan, C. K. Single Particle Raman Spectroscopy for Investigating Atmospheric Heterogeneous Reactions of Organic Aerosols. *Atmos. Environ.* **2007**, *41* (22), 4611–4621. https://doi.org/10.1016/j.atmosenv.2007.03.040.

(6) Bzdek, B. R.; Power, R. M.; Simpson, S. H.; Reid, J. P.; Royall, C. P. Precise, Contactless Measurements of the Surface Tension of Picolitre Aerosol Droplets. *Chem. Sci.* **2016**, *7* (1), 274–285. https://doi.org/10.1039/C5SC03184B.

(7) Power, R. M.; Simpson, S. H.; Reid, J. P.; Hudson, A. J. The Transition from Liquid to Solid-like Behaviour in Ultrahigh Viscosity Aerosol Particles. *Chem. Sci.* **2013**, *4* (6), 2597. https://doi.org/10.1039/c3sc50682g.

(8) Miles, R. E. H.; Walker, J. S.; Burnham, D. R.; Reid, J. P. Retrieval of the Complex Refractive Index of Aerosol Droplets from Optical Tweezers Measurements. *Phys. Chem. Chem. Phys.* **2012**, *14* (9), 3037. https://doi.org/10.1039/c2cp23999j.

(9) Knox, K. J.; Reid, J. P. Ultrasensitive Absorption Spectroscopy of Optically-Trapped Aerosol Droplets. *J. Phys. Chem. A* **2008**, *112* (42), 10439–10441. https://doi.org/10.1021/jp807418g.

(10) Rafferty, A.; Gorkowski, K.; Zuend, A.; Preston, T. C. Optical Deformation of Single Aerosol Particles. *Proc. Natl. Acad. Sci.* **2019**, *116* (40), 19880–19886. https://doi.org/10.1073/pnas.1907687116.

(11) Haddrell, A.; Rovelli, G.; Lewis, D.; Church, T.; Reid, J. Identifying Time-Dependent Changes in the Morphology of an Individual Aerosol Particle from Its Light Scattering Pattern. *Aerosol Sci. Technol.* **2019**, *53* (11), 1334–1351. https://doi.org/10.1080/02786826.2019.1661351.

(12) Mitchem, L.; Reid, J. P. Optical Manipulation and Characterisation of Aerosol Particles Using a Single-Beam Gradient Force Optical Trap. *Chem. Soc. Rev.* **2008**, *37* (4), 756. https://doi.org/10.1039/b609713h.

(13) David, G.; Esat, K.; Ritsch, I.; Signorell, R. Ultraviolet Broadband Light Scattering for Optically-Trapped Submicron-Sized Aerosol Particles. *Phys. Chem. Chem. Phys.* **2016**, *18* (7), 5477–5485. https://doi.org/10.1039/C5CP06940H.

(14) Ward, A. D.; Zhang, M.; Hunt, O. Broadband Mie Scattering from Optically Levitated Aerosol Droplets Using a White LED. *Opt. Express* **2008**, *16* (21), 16390. https://doi.org/10.1364/OE.16.016390.

(15) Davis, E. J.; Ravindran, P. Single Particle Light Scattering Measurements Using the Electrodynamic Balance. *Aerosol Sci. Technol.* **1982**, *1* (3), 337–350. https://doi.org/10.1080/02786828208958599.

(16) Carruthers, A. E.; Walker, J. S.; Casey, A.; Orr-Ewing, A. J.; Reid, J. P. Selection and Characterization of Aerosol Particle Size Using a Bessel Beam Optical Trap for Single Particle Analysis. *Phys. Chem. Chem. Phys.* **2012**, *14* (19), 6741. https://doi.org/10.1039/c2cp40371d.

(17) Davies, J. F.; Haddrell, A. E.; Reid, J. P. Time-Resolved Measurements of the Evaporation of Volatile Components from Single Aerosol Droplets. *Aerosol Sci. Technol.* **2012**, *46* (6), 666–677. https://doi.org/10.1080/02786826.2011.652750.

(18) Davies, J. F. Mass, Charge, and Radius of Droplets in a Linear Quadrupole Electrodynamic Balance. *Aerosol Sci. Technol.* **2019**, *53* (3), 309–320. https://doi.org/10.1080/02786826.2018.1559921.

(19) Preston, T. C.; Reid, J. P. Determining the Size and Refractive Index of Microspheres Using the Mode Assignments from Mie Resonances. *J Opt Soc Am A 32* (11), 2210–2217.

(20) Bohren, C. F.; Huffman, D. R. *Absorption and Scattering of Light by Small Particles*; John Wiley and Sons: New York, 1983.

(21) Gorkowski, K.; Donahue, N. M.; Sullivan, R. C. Emulsified and Liquid–Liquid Phase-Separated States of α-Pinene Secondary Organic Aerosol Determined Using Aerosol Optical Tweezers. *Environ. Sci. Technol.* **2017**, *51* (21), 12154–12163. https://doi.org/10.1021/acs.est.7b03250.

(22) Gorkowski, K.; Donahue, N. M.; Sullivan, R. C. Aerosol Optical Tweezers Constrain the Morphology Evolution of Liquid-Liquid Phase-Separated Atmospheric Particles. *Chem* **2020**, *6* (1), 204–220. https://doi.org/10.1016/j.chempr.2019.10.018.

(23) Haddrell, A. E.; Miles, R. E. H.; Bzdek, B. R.; Reid, J. P.; Hopkins, R. J.; Walker, J. S. Coalescence Sampling and Analysis of Aerosols Using Aerosol Optical Tweezers. *Anal. Chem.* **2017**, *89* (4), 2345–2352. https://doi.org/10.1021/acs.analchem.6b03979.

(24) Gorkowski, K.; Beydoun, H.; Aboff, M.; Walker, J. S.; Reid, J. P.; Sullivan, R. C. Advanced Aerosol Optical Tweezers Chamber Design to Facilitate Phase-Separation and Equilibration Timescale Experiments on Complex Droplets. *Aerosol Sci. Technol.* **2016**, *50* (12), 1327–1341. https://doi.org/10.1080/02786826.2016.1224317.

(25) Preston, T. C.; Reid, J. P. Accurate and Efficient Determination of the Radius, Refractive Index, and Dispersion of Weakly Absorbing Spherical Particle Using Whispering Gallery Modes. *J. Opt. Soc. Am. B* **2013**, *30* (8), 2113. https://doi.org/10.1364/JOSAB.30.002113.

(26) Symes, R.; Sayer, R. M.; Reid, J. P. Cavity Enhanced Droplet Spectroscopy: Principles, Perspectives and Prospects. *Phys. Chem. Chem. Phys.* **2004**, *6* (3), 474. https://doi.org/10.1039/b313370b.

(27) Reid, J. P.; Meresman, H.; Mitchem, L.; Symes†, R. Spectroscopic Studies of the Size and Composition of Single Aerosol Droplets. *Int. Rev. Phys. Chem.* **2007**, *26* (1), 139–192. https://doi.org/10.1080/01442350601081899.

(28) Pastel, R.; Struthers, A. Measuring Evaporation Rates of Laser-Trapped Droplets by Use of Fluorescent Morphology-Dependent Resonances. *Appl. Opt.* **2001**, *40* (15), 2510. https://doi.org/10.1364/AO.40.002510.

(29) Bain, A.; Rafferty, A.; Preston, T. C. Determining the Size and Refractive Index of Single Aerosol Particles Using Angular Light Scattering and Mie Resonances. *J. Quant. Spectrosc. Radiat. Transf.* **2018**, *221*, 61–70. https://doi.org/10.1016/j.jqsrt.2018.09.026.

(30) Lew, L. J. N.; Ting, M. V.; Preston, T. C. Determining the Size and Refractive Index of Homogeneous Spherical Aerosol Particles Using Mie Resonance Spectroscopy. *Appl. Opt.* **2018**, *57* (16), 4601. https://doi.org/10.1364/AO.57.004601.

(31) Steimer, S. S.; Krieger, U. K.; Te, Y.-F.; Lienhard, D. M.; Huisman, A. J.; Luo, B. P.; Ammann, M.; Peter, T. Electrodynamic Balance Measurements of Thermodynamic, Kinetic, and Optical Aerosol Properties Inaccessible to Bulk Methods. *Atmospheric Meas. Tech.* **2015**, *8* (6), 2397–2408. https://doi.org/10.5194/amt-8-2397-2015.

(32) Rafferty, A.; Preston, T. C. Measuring the Size and Complex Refractive Index of an Aqueous Aerosol Particle Using Electromagnetic Heating and Cavity-Enhanced Raman Scattering. *Phys. Chem. Chem. Phys.* **2018**, *20* (25), 17038–17047. https://doi.org/10.1039/C8CP02966K.

(33) Hart, M. B.; Sivaprakasam, V.; Eversole, J. D.; Johnson, L. J.; Czege, J. Optical Measurements from Single Levitated Particles Using a Linear Electrodynamic Quadrupole Trap. *Appl. Opt.* **2015**, *54* (31), F174. https://doi.org/10.1364/AO.54.00F174.

(34) Hart, M. B.; Sivaprakasam, V.; Czege, J.; Eversole, J. D. Using a Linear Electrodynamic Quadrupole as a Particle Trap. In *Optics in the Life Sciences Congress*; OSA: San Diego, California, 2017; p OtM3E.2. https://doi.org/10.1364/OTA.2017.OtM3E.2.

(35) Woźniak, M.; Derkachov, G.; Kolwas, K.; Archer, J.; Wojciechowski, T.; Jakubczyk, D.; Kolwas, M. Formation of Highly Ordered Spherical Aggregates from Drying Microdroplets of Colloidal Suspension. *Langmuir* **2015**, *31* (28), 7860–7868. https://doi.org/10.1021/acs.langmuir.5b01621.

(36) Biskos, G.; Malinowski, A.; Russell, L. M.; Buseck, P. R.; Martin, S. T. Nanosize Effect on the Deliquescence and the Efflorescence of Sodium Chloride Particles. *Aerosol Sci. Technol.* **2006**, *40* (2), 97–106. https://doi.org/10.1080/02786820500484396.

(37) Soonsin, V.; Zardini, A. A.; Marcolli, C.; Zuend, A.; Krieger, U. K. The Vapor Pressures and Activities of Dicarboxylic Acids Reconsidered: The Impact of the Physical State of the Aerosol. **2010**. https://doi.org/10.5194/acpd-10-20515-2010.

(38) Lienhard, D. M.; Huisman, A. J.; Bones, D. L.; Te, Y.-F.; Luo, B. P.; Krieger, U. K.; Reid, J. P. Retrieving the Translational Diffusion Coefficient of Water from Experiments on Single Levitated Aerosol Droplets. *Phys. Chem. Chem. Phys.* **2014**, *16* (31), 16677. https://doi.org/10.1039/C4CP01939C.

(39) Mori, Sadao. Response Correction of Differential Refractometer for Polyethylene Glycols in Size Exclusion Chromatography. *Anal. Chem.* **1978**, *50* (12), 1639–1643. https://doi.org/10.1021/ac50034a017.

(40) *Refractive Indices of Organic Liquids*; Lechner, M. D., Ed.; Landolt-Börnstein - Group III Condensed Matter; Springer-Verlag: Berlin/Heidelberg, 1996; Vol. 38B. https://doi.org/10.1007/b85533.

(41) Gallaugher, A. F.; Hibbert, H. Studies on Reactions Relating to Carbohydrates and Polysaccharides. XLIX. Molecular Weight, Molar Refraction, Freezing Point and Other Properties of the Polyethylene Glycols and Their Derivatives [1]. *J. Am. Chem. Soc.* **1936**, *58* (5), 813–816. https://doi.org/10.1021/ja01296a040.

(42) Krieger, U. K.; Siegrist, F.; Marcolli, C.; Emanuelsson, E. U.; Gøbel, F. M.; Bilde, M.; Marsh, A.; Reid, J. P.; Huisman, A. J.; Riipinen, I.; Hyttinen, N.; Myllys, N.; Kurtén, T.; Bannan, T.; Percival, C. J.; Topping, D. A Reference Data Set for Validating Vapor Pressure Measurement Techniques: Homologous Series of Polyethylene Glycols. *Atmospheric Meas. Tech.* **2018**, *11* (1), 49–63. https://doi.org/10.5194/amt-11-49-2018.

(43) Cotterell, M. I.; Willoughby, R. E.; Bzdek, B. R.; Orr-Ewing, A. J.; Reid, J. P. A Complete Parameterisation of the Relative Humidity and Wavelength Dependence of the Refractive Index of Hygroscopic Inorganic Aerosol Particles. *Atmospheric Chem. Phys.* **2017**, *17* (16), 9837–9851. https://doi.org/10.5194/acp-17-9837-2017.

(44) Bain, A.; Rafferty, A.; Preston, T. C. The Wavelength-Dependent Complex Refractive Index of Hygroscopic Aerosol Particles and Other Aqueous Media: An Effective Oscillator Model. *Geophys. Res. Lett.* **2019**, *46* (17–18), 10636–10645. https://doi.org/10.1029/2019GL084568.

(45) Millard, R. C.; Seaver, G. An Index of Refraction Algorithm for Seawater over Temperature, Pressure, Salinity, Density, and Wavelength. *Deep Sea Res. Part Oceanogr. Res. Pap.* **1990**, *37* (12), 1909–1926. https://doi.org/10.1016/0198-0149(90)90086-B.

(46) Daimon, M.; Masumura, A. Measurement of the Refractive Index of Distilled Water from the Near-Infrared Region to the Ultraviolet Region. *Appl. Opt.* **2007**, *46* (18), 3811. https://doi.org/10.1364/AO.46.003811.

(47) Shepherd, R. H.; King, M. D.; Marks, A. A.; Brough, N.; Ward, A. D. Determination of the Refractive Index of Insoluble Organic Extracts from Atmospheric Aerosol over the Visible Wavelength Range Using Optical Tweezers. *Atmospheric Chem. Phys.* **2018**, *18* (8), 5235–5252. https://doi.org/10.5194/acp-18-5235-2018.

(48) Bain, A.; Preston, T. C. Mie Scattering from Strongly Absorbing Airborne Particles in a Photophoretic Trap. *J. Appl. Phys.* **2019**, *125* (9), 093101. https://doi.org/10.1063/1.5082157.

(49) Mason, B. J.; King, S.-J.; Miles, R. E. H.; Manfred, K. M.; Rickards, A. M. J.; Kim, J.; Reid, J. P.; Orr-Ewing, A. J. Comparison of the Accuracy of Aerosol Refractive Index Measurements from Single Particle and Ensemble Techniques. *J. Phys. Chem. A* **2012**, *116* (33), 8547–8556. https://doi.org/10.1021/jp3049668.

CHAPTER IV

Hygroscopic Growth, Phase Morphology, and Optical Properties of Model Aqueous Brown Carbon Aerosol

4.1. Introduction

Aerosol in the atmosphere have direct and indirect effects on climate due to their role in cloud formation, light scattering, ice nucleation, and chemistry.[1,2] Aerosol particles may scatter and/or absorb incoming solar radiation, leading to cooling or warming effects depending on chemical composition.[3,4] Light-absorbing aerosol are a major product of biomass burning. In recent years, the extent of wildfires has increased, leading to the destruction of thousands of acres of land, increased health risks, and the emission of significant quantities of light-absorbing aerosol.[5–7] Wildfires have global impacts and knowledge of the properties and composition of emitted gaseous compounds and aerosol particles is required to fully understand their effects.[8,9] Recent studies also reveal that climate change may cause wildfires to increase in number globally, further prompting the need to more fully understand wildfire emissions.[5,10–12] A major component of emissions from biomass burning and wildfires are black carbon particles, which are strongly light-absorbing and contribute to the global radiation balance by absorption across the full solar spectral range.[13] Recent studies have also identified light-absorbing organic carbon compounds in aerosol produced in biomass burning. These compounds are classified as brown carbon (BrC) and absorb strongly at wavelengths <450 nm, leading to solutions of BrC appearing brown. BrC aerosol lead to decreased visibility and have a warming effect in atmosphere.[14,15] BrC may also be emitted due to coal combustion, automobile traffic,

and biomass burning, or produced via secondary oxidation reactions in the atmosphere.[9,16–22]

The chemical components of BrC particles include oxygenated functional groups, polycyclic aromatics, and nitrated groups.[13,23,24] Nitrated aromatic compounds (NAC), such as nitrophenols, nitroguaiacols, and nitrocatechols, are of interest because of their strong absorptive tendencies and their formation from VOC precursors, such as toluene and phenol, during both daytime (•OH + NO_2•) and nighttime (•OH + NO_3•) processes.[23,25,26] Although the insoluble components of BrC typically dominate light absorption, around 70% of BrC is water soluble and will experience hygroscopic interactions in the atmosphere in response to the ambient relative humidity.[27–29] Thus, the optical properties of water soluble BrC will depend on specific chemical composition and the environmental conditions. Additionally, BrC compounds can undergo oxidative aging via reactions with ozone and other oxidants, evolving the aerosol properties over time and leading to changes in the extent of light absorption.[30–32] Researchers have also noted that the co-emission of BC and BrC with inorganic material, such as sulfates, leading to particles containing a mix of organic and inorganic material.[28] Such mixtures may experience transitions to phase separated morphologies or other amorphous states at low relative humidity (RH).[33–35] Phase separated core-shell particles, for example, may enhance absorption through the lensing effect, motivating research on the physical properties and phase morphology of mixed BrC aerosol with inorganic species.[13,18,36]

Knowledge of the effects of RH on the physical and optical properties of particles containing BrC chromophores is limited. Indeed, recent modeling studies have indicated

the overestimation of absorptive contributions of BrC in their analyses, with RH and phase effects possibly contributing to some of the differences between modelled and measured light scattering.[21,37] In this study, we measure the hygroscopic growth of pure 4-nitrocatechol (4-NC), a commonly identified component of BrC used here as a proxy,[26,38] using a linear quadrupole electrodynamic balance (LQ-EDB) coupled with Mie resonance spectroscopy. Micron-sized particles were levitated in an electric field and probed as a function of RH to reveal their size, optical properties, and evolving phase morphology. Typical particle sizes used with this method fall within 3 to 10 μm to ensure sufficient spectral information was available to accurately characterize size and optical properties. Particles smaller than 3 μm do not show sufficient spectral features in the wavelength range of interest, while particles larger that 10 μm show a lot of detail leading to difficulties in finding unique solutions. These sizes are large compared to atmospheric particles, but studies have shown size-dependent morphologies only become important at <100 nm and the conclusions derived from this work may be generally applied to a broad size range of particles.[33,39] We classify the extent of water uptake via radial growth factors and report changes in optical properties through the complex refractive index. To further explore how BrC chromophores behave in internal mixtures, we explore the hygroscopicity and phase morphology of a series of mixtures of 4-NC with ammonium sulfate, characterizing optical properties and identifying phase transitions. Finally, we explore the imaginary component of the complex refractive index using an effective oscillator model to derive how the absorption properties vary with wavelength and composition.

4.2. Methods

4.2.1. Sample Preparation and Chemicals

All chemicals in this study were purchased and utilized without additional purification. Hygroscopic growth, deliquescence, and phase separation measurements were conducted using particles containing 4-nitrocatechol (Sigma-Aldrich, 97.0 % purity), ammonium sulfate (VWR Analytical, ≥ 99.0 % purity), and lithium chloride (Sigma-Aldrich, ≥ 99.0 % purity). Pure component solutions were prepared at concentrations of 4 to 6 g/L, and solutions of ammonium sulfate and 4-nitrocatechol were prepared in mole ratios of 1:1, 2:1, 4:1, and 5:1 at total solute concentrations of 4 to 6 g/L. Compounds were weighed and dissolved in HPLC water (Fisher Chemical), filtered with a 0.2 µm syringe filter (VWR International), and stored in a pre-cleaned glass vial. Approximately 12 µL of solution was introduced to a microdroplet dispenser (Microfab MJ-ABP-01, 30 µm orifice) to produce droplets for introduction into the LQ-EDB.

4.2.2. Experimental Setup

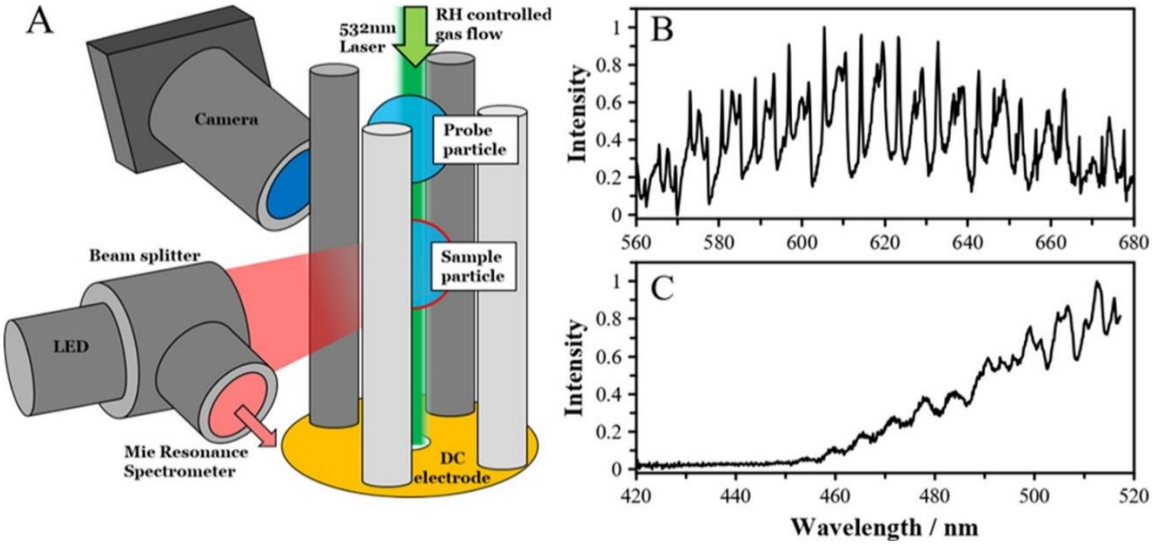

Figure 4.1: (A) Schematic experimental configuration for the hygroscopic growth and phase measurements reported in this work. Laser light was used to visualize droplet during initial trapping and was not required for Mie resonance spectroscopy. (B) Mie resonance spectrum for pure 4-NC at ~90% RH recorded at 560 – 680 nm. (C) The same pure 4-NC particle at 90% recorded at 420 – 520 nm.

4.2.2.1. Particle Levitation

A linear quadrupole electrodynamic balance (LQ-EDB) was used to levitate single or multiple particles for extended periods of time using electric fields as previously described.[40] The process is briefly summarized here. Dilute sample droplets were generated from a microdroplet dispenser in the presence of an induction electrode, at 200 to 500 V, to impart a net charge of 10 to 100 fC onto the emerging droplet as it was introduced into the LQ-EDB chamber.[40,41] A 532 nm laser (Laser Quantum Gem) with a 0.9 mm beam width and operating power of less than 5 mW was used to illuminate droplets in the chamber for verification of trapping, but was disabled for measurements. The droplets entered the quadrupole electrode arrangement with applied AC voltages generating an electric field confining them to the central axis. The droplets fell freely along the axis of

the rods due to gravity and came to rest in a linear stack above a disc electrode placed in the center of the chamber. An applied DC voltage (30 - 300 V) created a repulsive electrostatic force that balanced net forces on the droplets and maintained the stack in a fixed position. Excess solvent evaporated from the droplets and the resulting particles attained equilibrium with the chamber conditions.[1] A CMOS camera (Thorlabs DCC1545) was used to image particles and stabilize the position by varying the DC voltage through a PID feedback loop, programmed using LabVIEW software.

4.2.2.2. Environmental Monitoring – Dual Droplet Method

The relative humidity (RH) in the chamber was controlled by introducing a mixture of dry and humidified nitrogen at a total flow rate of 200 cm^3/min. The RH in the chamber was monitored using a dual-droplet method, with a lithium chloride probe particle, for the duration of each measurement.[42] In the dual-droplet method, two separate dispensers and induction electrodes are used to introduce two chemically distinct droplets. The resulting probe and sample particles are confined together, and the relative humidity experienced by the probe is the same as the sample. The particles controllably switch positions for sampling via Mie resonance spectroscopy and the size response of the sample informs the RH in the chamber with high accuracy and precision.

4.2.2.3. Mie Resonance Spectroscopy

A white LED (Thorlabs MCWHL6 with 6500 K output) was used to illuminate the particle of interest for Mie resonance spectroscopy. Backscattered light from the particle was collected by fiber optic and delivered to a Raman spectrometer (FERGIE, Princeton Instruments) configured with a 1200 groove/mm grating and resolution of 0.26 nm. Spectra

contain light reflected from the surface of the particle and light that is resonant within the spherical cavity, creating intense peaks in the spectra that are characteristic of the size and optical properties of the sample. Spectra were collected with a 1 s exposure time from both the levitated sample and probe particles. The particles were switched every 10 seconds for the duration of the experiment. Spectra obtained across red wavelengths (Figure 4.1B) were analyzed offline to find the center of each resonance peak using a peak search algorithm. The wavelength positions were analyzed using the algorithms of Preston and Reid to find the radius and wavelength-dependent real component of the complex refractive index via a least-squares minimization process.[43–45] To validate results, simulations of the full spectra were generated using Mie theory code for a visual comparison to experimental spectra.[46] Changes in the Mie resonance spectra were used to identify phase transitions, as discussed further in the results. Spectra obtained at shorter wavelengths (Figure 4.1C) showed a significant influence of light absorption and were used to characterize the imaginary component of the complex refractive index.

4.2.3. Light-Induced Perturbations in 4-NC Particles

Due to the light-absorbing properties of BrC chromophores, careful illumination of the sample is required. Under illumination by 532 nm laser light, significant heating can occur leading to perturbations in the particle properties due to changes in temperature. Figure 4.2 shows a comparison of the size of a pure 4-NC particle with unfocused laser and focused LED illumination at different powers.

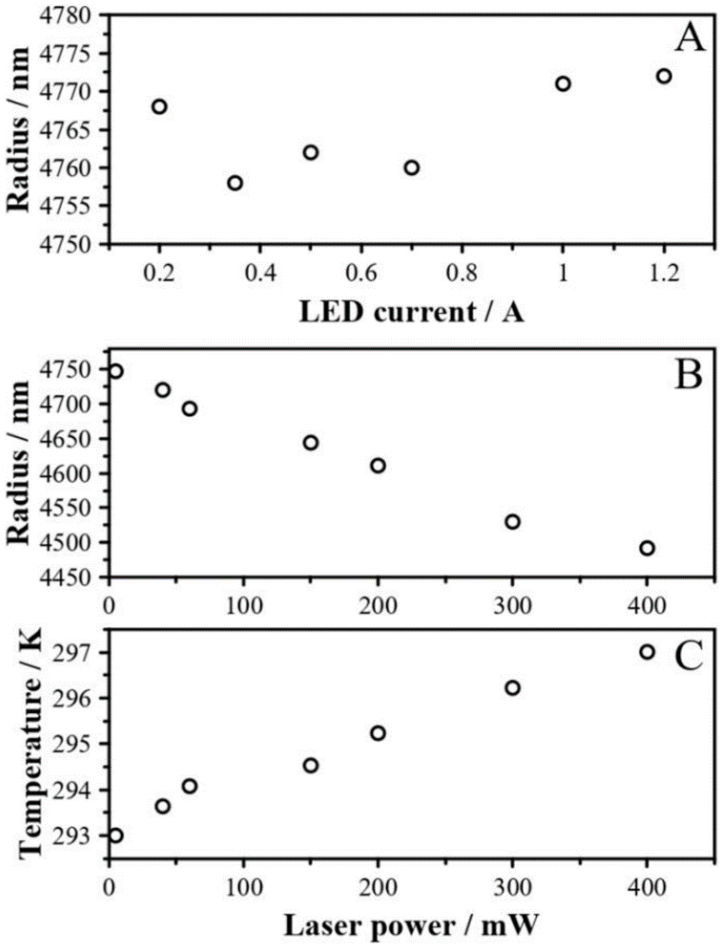

Figure 4.2: (A) Measured radius of a 4-nitrocatechol particle at 85% RH exposed to LED illumination across the full range of supplied electrical current (proportional to the power). (B) The same 4-NC particle exposed to increasing illumination from a 532nm unfocused CW laser. (C) Using the hygroscopic response of the particle, reported later, the temperature of the laser-illuminated particle was inferred as described in the text.)

The LED illumination source was used for Mie resonance spectroscopy, and particles show a constant size up to the full rated output power of 1430 mW, with a current of 1.2 A. In reality, the power incident on the particle was orders of magnitude below this value due to the optical arrangement, focal spot size, and particle size. Thus, while these measurements demonstrate that no influence of LED illumination occurred for these studies, they do not preclude LED illumination from having an effect in different optical arrangements. Laser

illumination was used for visual verification of the particle in the trap, and particles exposed to an environmental RH of 85% show a decrease in size as the laser power was increased from 5 mW up to 400 mW (Figure 4.2B). As with LED illumination, the power incident on the particle is much less as the laser light was not focused. The beam diameter was 0.9 mm, allowing us to estimate the power incident on the particle to be approximately 0.05 mW at maximum power. The decrease in particle size can be associated with the temperature of the particle, as shown in Figure 4.2C. The vapor pressure of water above the aqueous particle must be in equilibrium with the water vapor pressure of the environment, which is determined by the RH. Thus, if the temperature of the particle increases, the water activity in the particle must decrease to maintain equilibrium. The temperature of the particle and the environment can be separated, giving:

$$p^{\circ}(T_{part}) = \frac{\frac{RH}{100}}{a_w} p^{\circ}(T_{env}) \tag{4.1}$$

where $p^{\circ}$is the saturation vapor pressure of water and a_w is the water activity, which is related to the solute concentration and the hygroscopicity of the particle (as determined later). The GF for pure 4-NC (reported in a later section) was used to determine a_w, and the vapor pressure of water as a function of temperature is known.[44] At 5 mW, the particle temperature shows negligible deviation from ambient conditions of 293 K and, as the laser power is increased, the estimated temperature increases up to 297 K at 400 mW. Efflorescence of the particle was observed at higher laser powers, indicating the potential for significant perturbations to the system if high illumination intensities are used. To avoid the heating of the sample, only light from the LED was used to collect spectra in both the red and blue regions for the experiments discussed subsequently.

4.2.4. Electrostatic Determination of Dry Size

For hygroscopic growth measurements, an indication of the dry particle size is required in order to determine a radial growth factor (GF). The dry size is difficult to determine experimentally since the particle is no longer spherical and homogenous under dry conditions. In the LQ-EDB, the weight of the particle and the drag force applied from the air flow are strongly linked to the size of the particle. The drag force of the particle is much larger than the weight at the size range measured here. For a particle with a 5 μm radius and a density of 1 g/cm^3, the weight force is 5.1×10^{-12} N and the Stokes drag force under the applied 0.1 m/s gas flow is 1.6×10^{-10} N. Thus, the electrostatic force contributes primarily to balancing the drag force on the particle. Given that the drag force scales with the radius, the DC voltage will be strongly weighted towards a linear proportionality with radius. Under the assumption that the shape factor is 1 (or close to 1), the ratio of the DC voltage at a specific RH (75.5% - the deliquescence RH of NaCl, or 80% RH, the deliquescence RH of ammonium sulfate) to the DC voltage at the efflorescence RH may be used to estimate the GF (Figure 4.3). This was used in conjunction with the measured size at the noted RH to find the dry size of the particles, and subsequently the GF for any RH was determined.

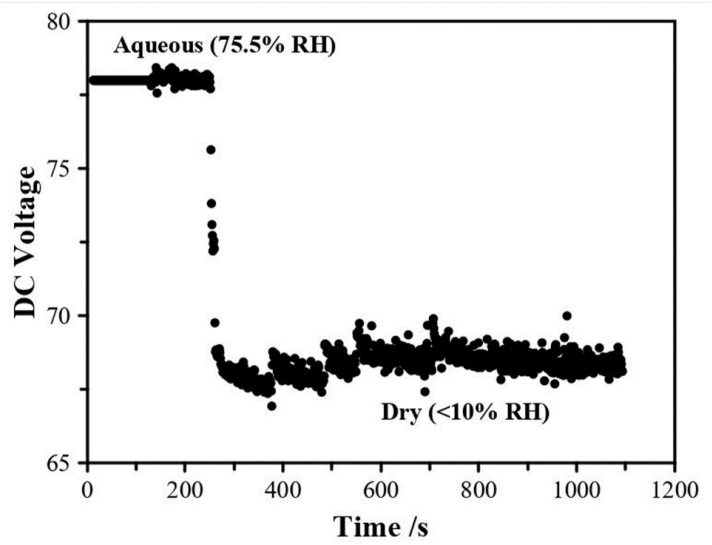

Figure 4.3: To determine the dry size, the voltage generating the electrostatic force was found for an aqueous particle at 75.5% RH and under dry conditions. The drift in voltage following efflorescence is due to small changes in the gas flow velocity as the RH was stepped down to dry conditions. As described in the main text, the drag force is much greater than the weight, and the voltage was assumed to be proportional to the radius.

4.3. Results and Discussion

4.3.1. Pure 4-Nitrocatechol Particles

4-Nitrocatechol (4-NC) was chosen for study here as a proxy for light-absorbing water-soluble BrC organic compounds. 4-NC is water soluble due to its oxygenated functional groups and appears mustard yellow in an aqueous solution. Here, we characterize its hygroscopic properties, phase transitions, and optical properties as a function of RH. To ensure the sample was not perturbed due to the optical probing methods, we first explored the influence of LED and laser illumination on the properties of the particle and report these results in the Figure 4.2. Briefly, while laser illumination was observed to produce measurable changes in the size due to an increase in the particle temperature, LED illumination had no effect. Thus, the laser was disabled for the subsequent measurements reported here.

4.3.1.1. Hygroscopic Growth of 4-NC Particles

The presence of hydrophilic chemical moieties in 4-NC allows for reversible hygroscopic interactions with water vapor and 4-NC particles will experience hygroscopic growth as a function of RH due to the uptake and loss of water. The size of the levitated 4-NC particles was measured as a function of RH in a dual-droplet measurement conducted with a LiCl probe particle to monitor the RH. The hygroscopic growth cycle was performed to a minimum RH of 73% and maximum RH of 95 %, with <0.2% uncertainty in the reported RH using the dual-droplet method. The RH was stepped down 0.5% every 30 s to produce a pseudo-continuous RH change. Other experiments used larger RH steps that caused efflorescence of the pure 4-NC droplet at RH >73%, but below 73% RH efflorescence was observed randomly regardless of the size of the RH change steps.

As described previously, the dry size of the particle was found using the ratio of DC voltages at two known RH conditions to estimate a GF at 75.5% and subsequently determine the dry size from the measured particle size at this RH. The dry size was then used to calculate the GF for a range of RH. Figure 4.4A shows the GF as a function of RH for pure 4-NC over the range in which particles existed in a liquid aqueous state. From these data, we calculate the κ parameter from κ-Köhler theory. The growth factor depends on κ according to:

$$GF = \left(\frac{a_w(1-\kappa)-1}{a_w-1}\right)^{\frac{1}{3}} \quad (4.2)$$

where a_w is water activity and $\kappa = \sum_i V_i\kappa_i$. V_i represents the volume fraction of i in the dry particle and κ_i is the hygroscopicity parameter of component i. κ quantifies the

hygroscopic properties of aerosol particles, approximating the influence of a range of physiochemical factors such as solubility, molecular weight, and non-ideal mixing. Measurements of κ in subsaturated RH conditions can show a variation with RH, reflecting the challenges of simplifying high concentration aqueous solutions to a single parameter. Indeed, a single value of κ, as shown in Figure 4.4A, cannot reproduce the observed hygroscopic growth and a linear dependence on RH is observed. The value of κ approached at high RH, shown in Figure 4.4, assuming a linear trend, is on the order of 0.03. A linear trend is not always observed, however, and significant discontinuities in κ at high RH have been observed, limiting the broad use of this metric in predicting CCN activity, for example.[47] Based on the O/C ratio of 0.667 and the work of Rickards et al.,[48] the estimated κ would fall in the range 0.12 ± 0.01, while the ideal κ value derived from the ratio of the molar volume of 4-NC to the molar volume of water, yields a value of 0.19. The measured value is lower than both of these and may reflect uncertainties in the extrapolation of κ to saturated RH conditions, or molecular interactions specific to 4-NC that lead to weaker interactions with water, such as intermolecular H-bonding between NO_2 and OH groups.

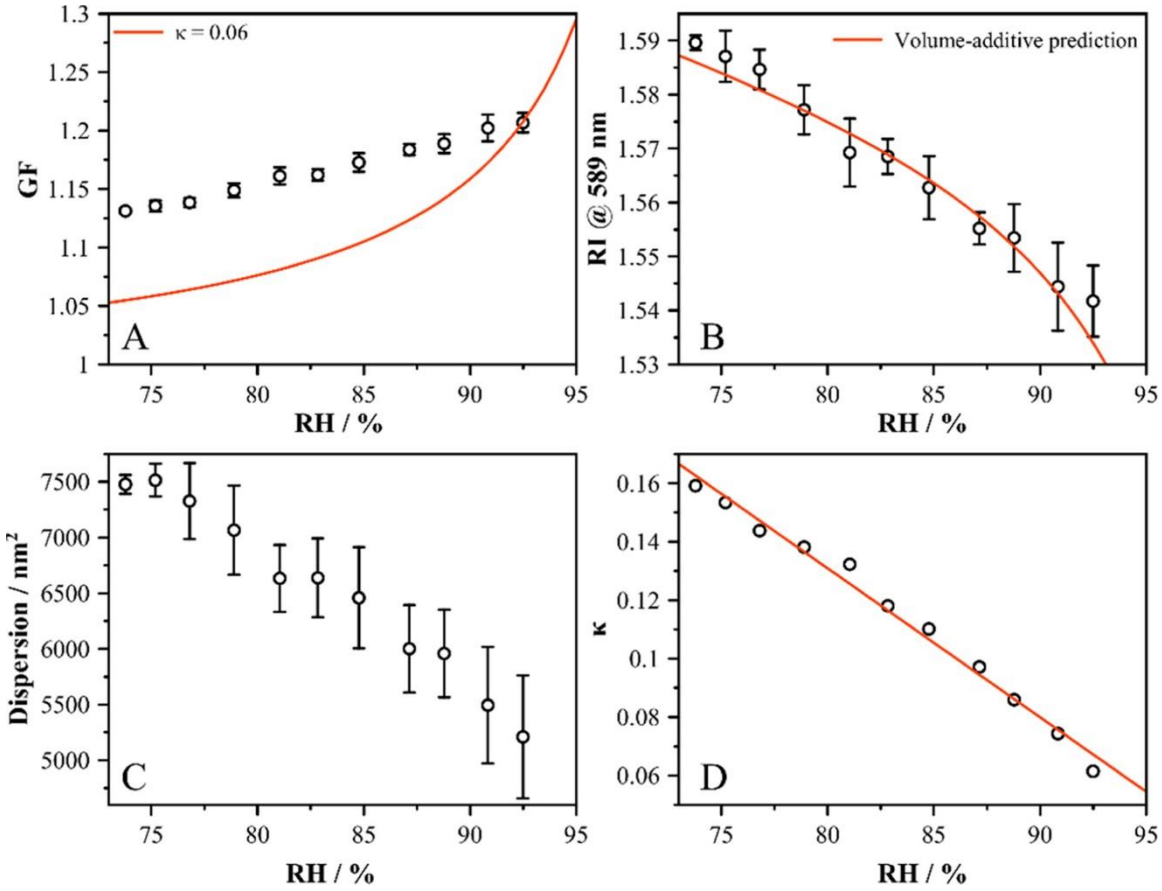

Figure 4.4: (A) Radial growth factor (GF) of pure 4-nitrocatechol versus RH. The prediction from κ-Köhler theory is shown in red using a fixed value determined at the highest measured RH. (B) Real part of the refractive index ($n(\lambda) = n_0 + \frac{n_1}{\lambda^2}$) as a function of RH. (C) Dispersion parameter (n_1) as a function of RH. Error bars for panels A-C are derived from the standard deviations in each parameter from binning the data in 2% steps. (D) The κ parameter was calculated at every measured point yielding a linear parameterization ($\kappa = 0.5384 - 0.0051 \times RH$).

4.3.1.2. Efflorescence and Deliquescence of 4-NC Particles

4-NC particles spontaneously effloresced under a range of RH conditions when subjected to large RH changes. To constrain the efflorescence point, smaller RH changes, in steps of ~0.5%, were made until efflorescence was observed. Even with smaller RH steps, 13 particles were seen to effloresce in the range from 40 to 80 %, with 7 particles efflorescing within the 40 – 50 % range and the remaining 6 particles efflorescing in the 59 – 80 %

range. After efflorescence, the RH was slowly increased up to ~93 % to explore the deliquescence RH. However, even when particles were left at a high RH for more than 30 min (and up to ~12 hours), deliquescence was not observed. These observations indicate a large hysteresis in the deliquescence/efflorescence behaviour of 4-NC, with a deliquescence RH likely much close to saturation than was achieved in the measurements reported here. This behavior is consistent with other low solubility organic molecules, such as succinic acid, which deliquesce in the range 99 to 100% RH.[49,50] The solubility of 4-NC is less than that of succinic acid, implying that the DRH of 4-NC is likely to be close to 100%. These observations point to an irreversible efflorescence process under ambient RH conditions, and likely only close to saturated or cloud forming RH conditions would be sufficient to solubilize the dried particles.

4.3.1.3. Optical Properties of 4-NC at 589 nm

In addition to the size of the particles varying with RH, changes in the optical properties are expected. As RH is decreased the refractive index is expected to rise since the concentration of the solute in the particle increases. The real part of the RI as a function of wavelength is treated using a 1st order Cauchy expression to account for the wavelength dispersion of the RI:

$$n(\lambda) = n_0 + \frac{n_1}{\lambda^2} \quad (4.3)$$

where n_0 and n_1 are Cauchy coefficients output from the Mie resonance peak fitting algorithm. We report the RI at a wavelength of 589 nm (i.e. $n(589nm)$) in Figure 4.4B. The RI spans a range of 1.59 to 1.54 going from low and high RH. The RI of pure 4-NC is predicted by a chemical property estimator (ACD/Labs Percepta Platform - PhysChem

Module via chemspider.com) to be 1.668, however direct measurements are not available. An estimate of the pure component RI may be found using a volume-fraction mixing rule relationship, which has been shown to be effective for estimating the real part of the RI:[51]

$$RI = \frac{1}{rgf^3} \times RI_{sol} + \frac{rgf^3 - 1}{rgf^3} \times RI_{H_2O} \quad (4.4)$$

where rgf is the radial growth factor, RI_{H_2O} is the RI of pure water, and RI_{sol} is the RI of the solute 4-NC. The value of the latter was varied to achieve agreement of the measured and predicted RI across the whole range of measured growth factors, revealing an RI of the pure component to be ~1.70 at 589 nm. The volume-additive prediction is shown in Figure 4.4B based on this value.

Figure 4.4C shows the change in the dispersion over the RH range studied. The dispersion coefficients, n_0 and n_1, were fitted values in the Mie resonance analysis. Although the dispersion is high compared to aqueous salts, which show values around 2000 – 4000 nm^2, it is not unexpected that a light-absorbing component would show a stronger wavelength dependence. It is important to note that while the Cauchy dependence works well in the wavelength range of 560 to 680 nm, it is not appropriate to extrapolate this dependence to shorter wavelengths, where absorption becomes more intense, and the Cauchy dependence breaks down. We discuss the imaginary part of the refractive index in a later section.

4.3.2. Internally-Mixed Particles of 4-Nitrocatechol and Ammonium Sulfate

In the atmosphere aerosol particles consist of multiple components. To reproduce this chemical complexity, ammonium sulfate (AS) was added in known quantities to 4-NC. In this section, we identify the effect of AS on the hygroscopicity, phase and optical properties of 4-NC particles.

4.3.2.1. Hygroscopic Growth of Mixed Particles

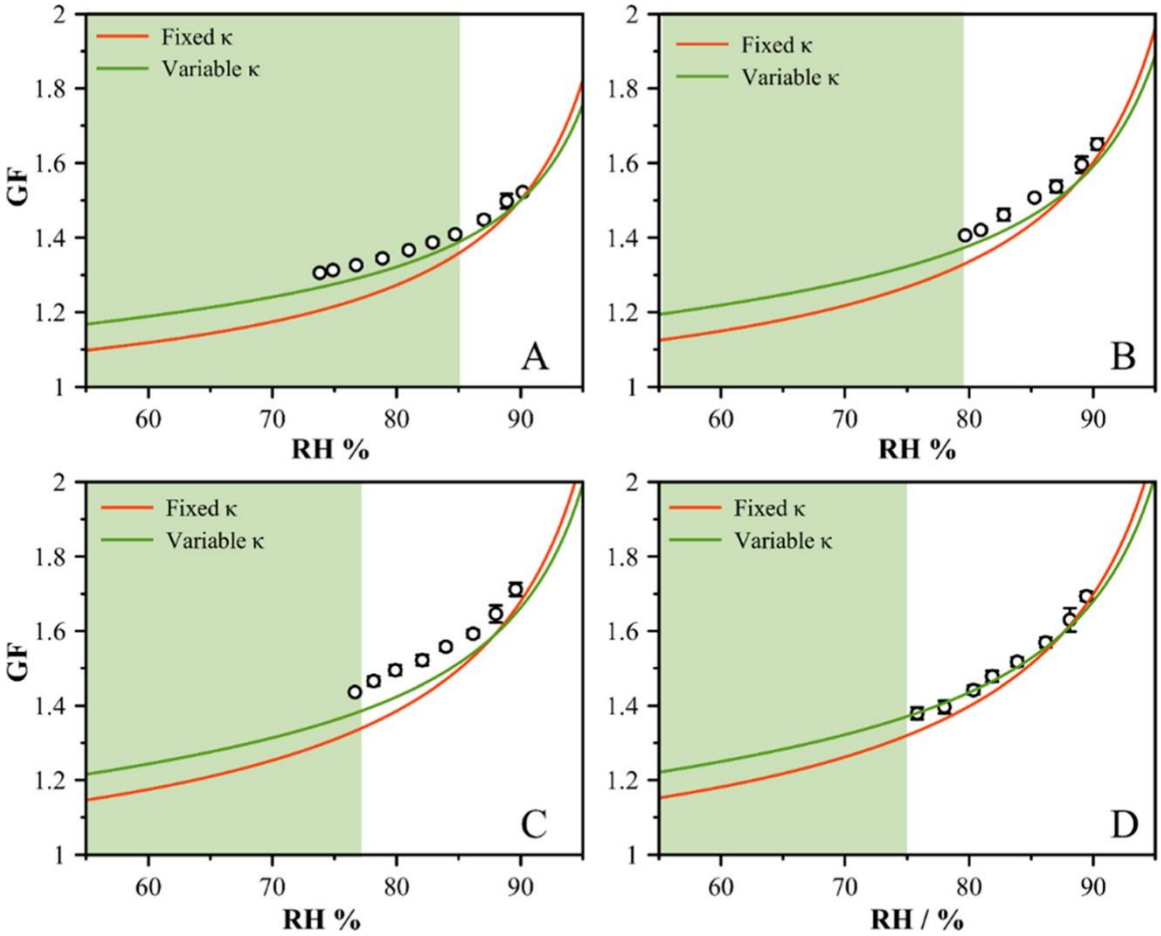

Figure 4.5: Hygroscopic growth of mixed 4-nitrocatechol and ammonium sulfate particles. (A) 1:1, (B) 1:2, (C) 1:4, and (D) 1:5. The green shaded region indicates the region where phase separation is observed, and thus indicates where the GF becomes less reliable. The red line shows the estimated GF using κ-Köhler theory and fixed values of κ, while the green line shows a RH-dependent κ with $\kappa_{4NC}(RH)$ reported in Figure 4.4, and $\kappa_{AS}(RH) = 1.2142 - 0.0079 \times RH$, derived from E-AIM.[52]

As expected, due to the addition of a hygroscopic salt, an equimolar mixture of 4-NC and AS resulted in particles that show more significant hygroscopic growth. Over the course of performing measurements that spanned a broad range of RH, regions were identified in which particles exhibited phase transitions, denoted by shading in Figure 4.5. These phase transitions, discussed later, limited the range of RH that robust hygroscopic growth data could be derived due to interference with the Mie resonance spectra. Figure 4.5A-D shows the hygroscopic growth curves determined for 1:1, 1:2, 1:4 and 1:5 molar mixtures of 4-NC to AS. The trend towards greater hygroscopic growth continues as more AS is added to the particle. We can establish a crude prediction for the radial growth factor based on κ-Köhler theory, using a volume-fraction mixing rule combined with the pure component κ for 4-NC and AS. In the previous section, we reported κ for pure 4-NC and, using the literature value of κ for AS of 0.53,[53] we calculate the predicted GF for each mixture using a volume mixing rule.[53] Results are shown in Figure 4.5. In all four mixtures, the predicted GF lines up well with experimental values at high RH but deviates as RH decreases. As established, the value of κ is not constant in sub-saturated conditions for 4-NC and AS. Using a linear expression for κ as a function of RH for both 4-NC and AS, we can estimate a more accurate value to represent the hygroscopic growth across the measured range. These predictions are also shown in Figure 4.5 and reveal closer agreement to the measured data across the entire RH range, although the model still underpredicts the hygroscopicity relative to measurements in most cases, with good agreement only observed at high AS loading in the particle. This indicates potential interactions between AS and 4-NC

molecules in solution that influence how they interact with water. The GF could not be measured at lower RHs due to the onset of phase separation in each of the mixtures.

The real part of the refractive index at 589 nm and the dispersion parameters for these mixtures are reported in Figure 4.6 and 4.7, respectively, and follow the expected trends given the additional water present as the amount of AS is increased.

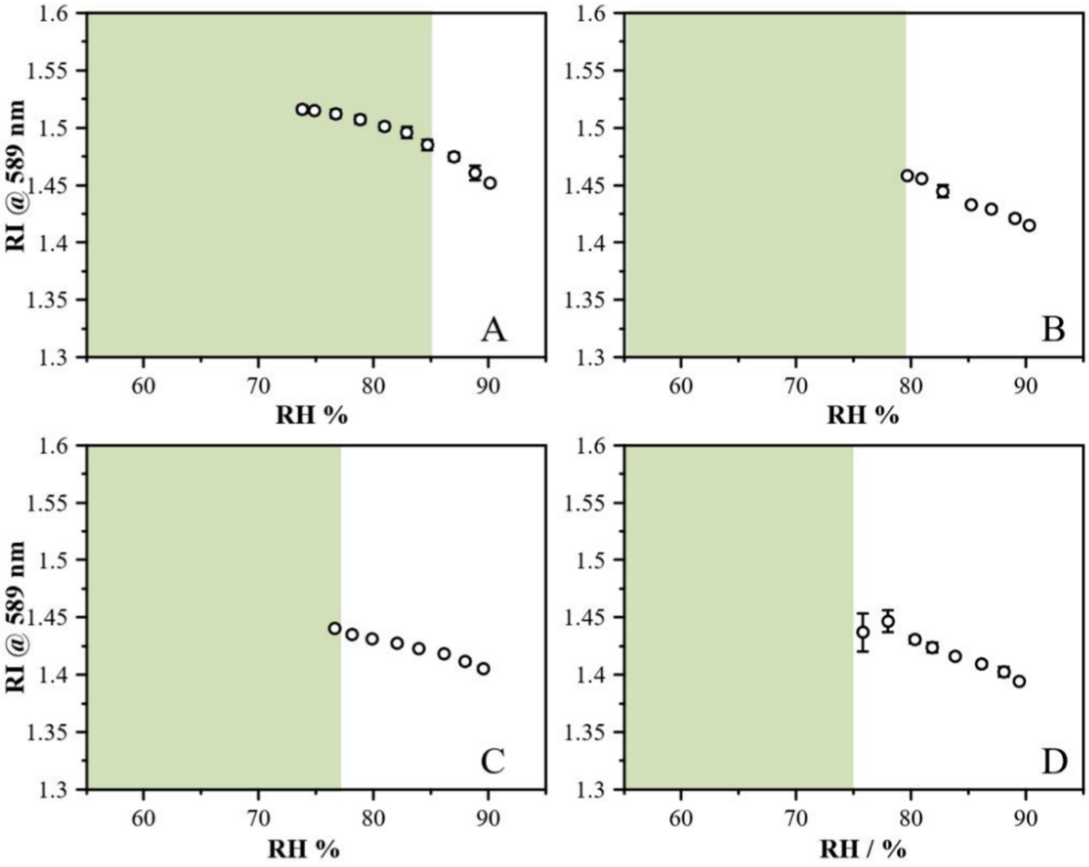

Figure 4.6: The RI ($(n(589nm)$) of 1:1, 2:1, 4:1 and 5:1 mixtures (A through D respectively) of AS to 4-NC as a function of RH. The green shaded region indicates where the particles enter phase separated states.

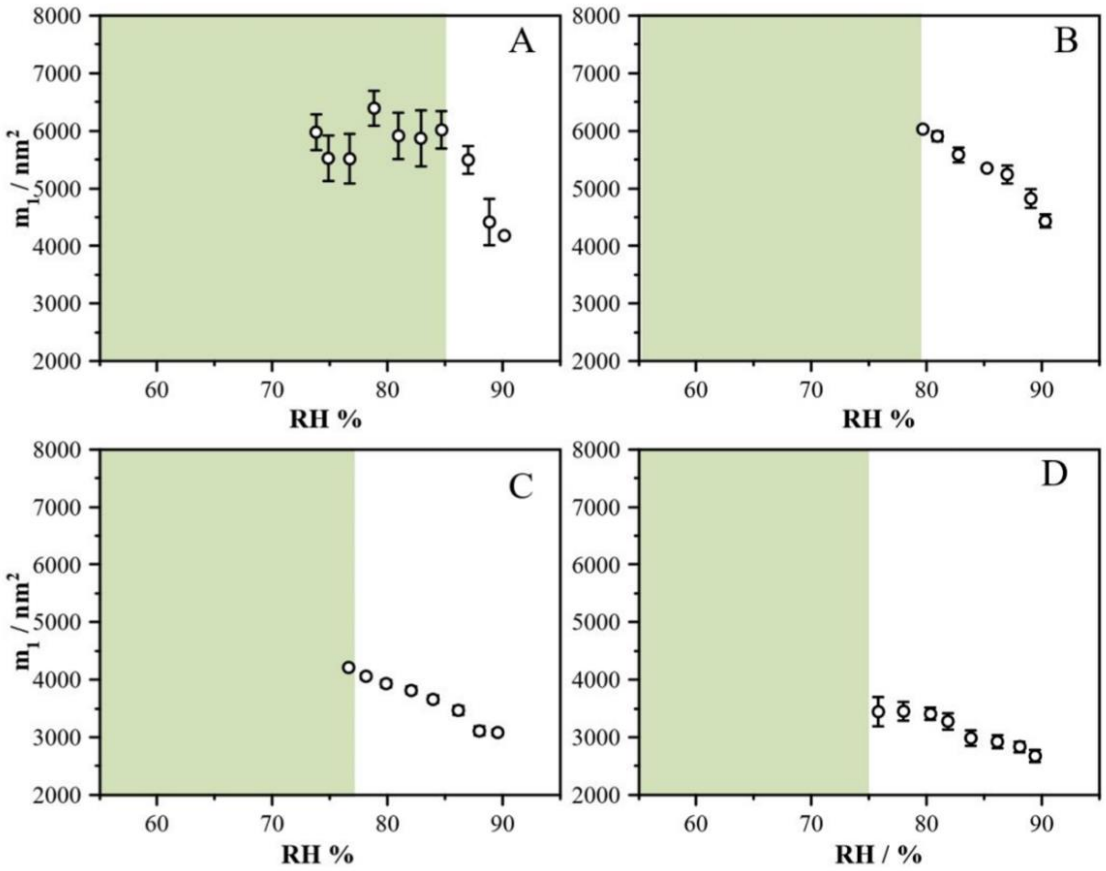

Figure 4.7: The dispersion (m_1) of 1:1, 2:1, 4:1 and 5:1 mixtures (A through D respectively) of AS to 4-NC as a function of RH. The green shaded region indicates where the particles enter phase separated states.

4.3.2.2. Phase Separation in Particles Containing 4-NC and AS

Due to the presence of low solubility organic species and an inorganic component, deviations from a well-mixed homogenous particle may occur as the RH decreases and phase separation may arise.[34,54] Phase separation in the particle will cause changes in the measured Mie resonance spectra and derived results.[54,55] The possible morphologies that may be identified from the changes to Mie resonance spectra include core-shell, in which spectra retain sharp peaks but the derived size and optical data show anomalies due to light scattering at the liquid-liquid boundary, and partially engulfed / aggregated, where a

breakdown of the scattering pattern indicate a loss of sphericity or the disruption of the particle surface due to solid aggregates. Full efflorescence is identified from a complete loss of structure in the Mie resonance spectrum. In this section we describe the phase separation as liquid-liquid phase separation (LLPS), although a precise determination of the different phases is not possible.

Table 4.1. Measured onset RH (sRH) of LLPS in particles containing AS and 4-NC. Uncertainties represent the standard deviation in repeat measurements.

AS:4-NC	Mole fraction of AS	SRH (%)
1:1	0.5	85 ± 1.9
2:1	0.66	80 ± 1.5
4:1	0.80	78 ± 2.5
5:1	0.83	76 ± 2.5

In each mixture the onset of LLPS is identified, with evidence for each shown in Figures 4.8 – 11. According to previous work by Stewart et al.[55] the onset of LLPS can be inferred from changes in the appearance of the morphology-dependent resonances (MDR's) in the Mie resonance spectrum or in the results of the sizing algorithm. A core-shell structure is indicated by the retention of strong sharp peaks with a discontinuity in output parameters, such as dispersion or the error in the fit. Complete loss of MDR's indicates a loss of sphericity, while a broadening of MDR's points to a partially engulfed structure that returns a smooth surface but is not purely spherical, or the presence of light scattering aggregates that disrupt the optical cavity. By considering these factors, we interpret our observations and assign LLPS transitions as core-shell or partially engulfed, noting in the latter case that aggregate scattering may also lead to similar observations. Repeat measurements on particles showed these transitions were reproducible at the same RH. As the AS component

is increased, the LLPS onset RH (SRH) is lowered, as reported in Table 4.1. The 5:1 mixture showed the lowest SRH (~76%), which was found due to an anomalous shift in dispersion from 4000 nm^2 to 3500 nm^2 and subsequent increase in fitting error below 77 % from the MRFIT results (Figure 4.8). The spectra itself did not show a visible difference once this RH was reached, indicating this formed a core-shell morphology.

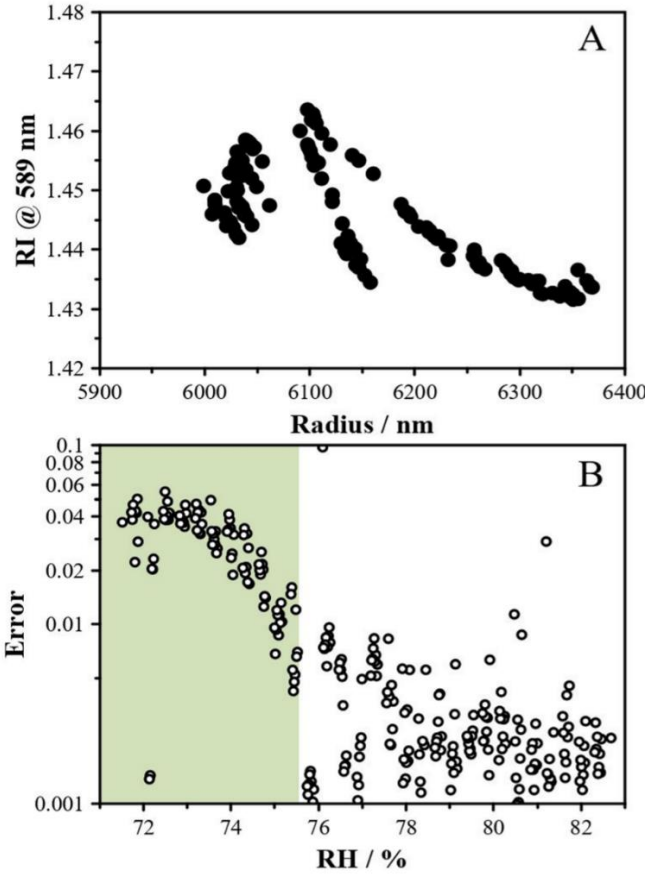

Figure 4.8: (A) The radius and RI for a mixed particle containing 5:1 ammonium sulfate and 4-nitrocatechol, by mole. For a homogeneous sphere, the size and RI would be expected to vary monotonically. The observed deviation from this indicates a breakdown of sizing due to phase separation. (B) The increase in error in the peak fitting process indicates deviation from a homogeneous sphere, support a phase transition at ~76% RH.

The 4:1 mixture showed a clear increase in the fitting error, indicating a phase transition at 78% RH (Figure 4.9), with a loss of spectral detail below 76%, indicating initially the

formation of a core-shell morphology that on continued drying transitioned to a partially engulfed morphology.

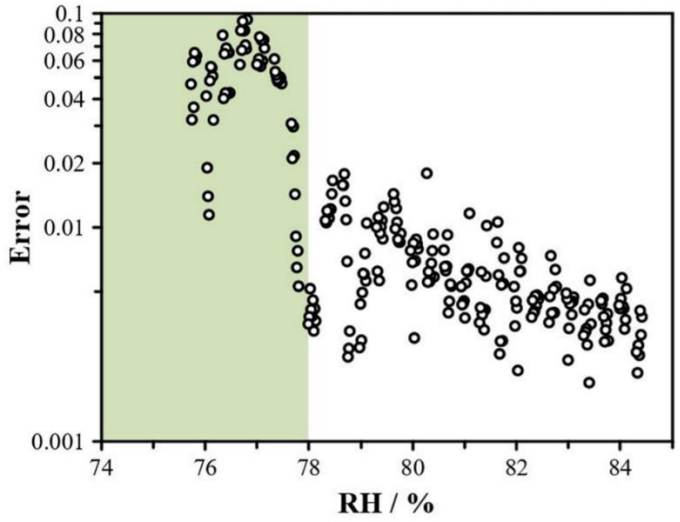

Figure 4.9: The error in the peak fitting process for 4:1 AS:4-NC particles shows an increase at 78% RH, indicating the onset of phase separation.

In the case of the 2:1 mixture, the spectra showed visible changes between at around 80% RH (Figure 4.10), indicating LLPS to a partially engulfed morphology or one containing aggregates of material that scatter light and disrupt the resonant cavity of the particle.

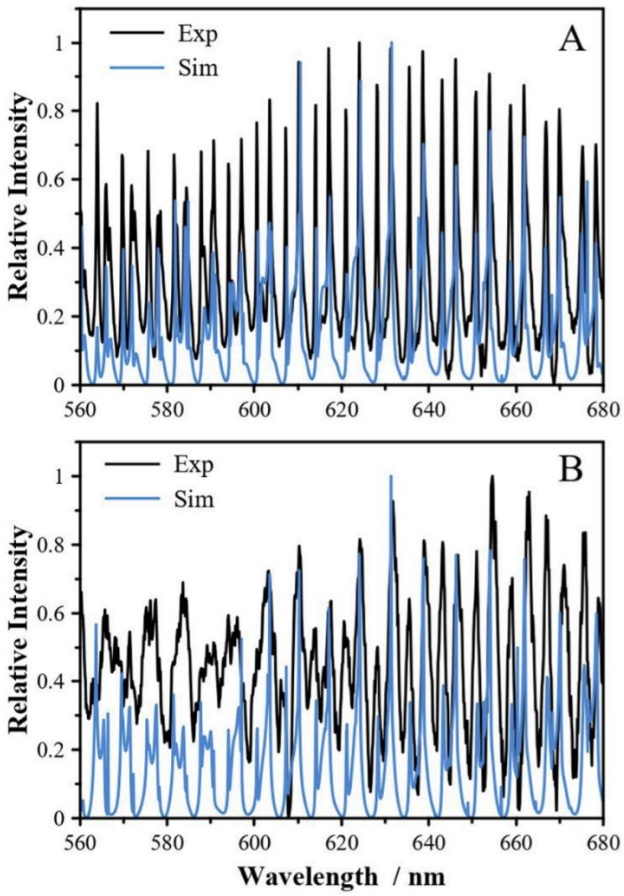

Figure 4.10: (A) Prior to phase separation, 2:1 AS:4-NC particles show clear Mie spectra with accurate size results at 81% RH (B) Following phase separation, the spectra breaks down, indicating a loss of sphericity and the formation of a partially engulfed morphology, or the formation of large aggregates that scatter light and disrupt the standing waves forming resonance peaks. This occurs at an RH of 80%.

In all cases, an increase in RH led to attainment of spectra indicating homogeneous well-mixed particles, revealing these LLPS transitions to be reversible. The 1:1 mixture did not show clear indications of a phase transition and instead showed a continuous trend in both the size and RI as RH was varied. The spectra showed no discernable changes in peak shape, but an anomalous plateau in the dispersion, shown in Figure 4.11, indicated LLPS may occur at around 85%.

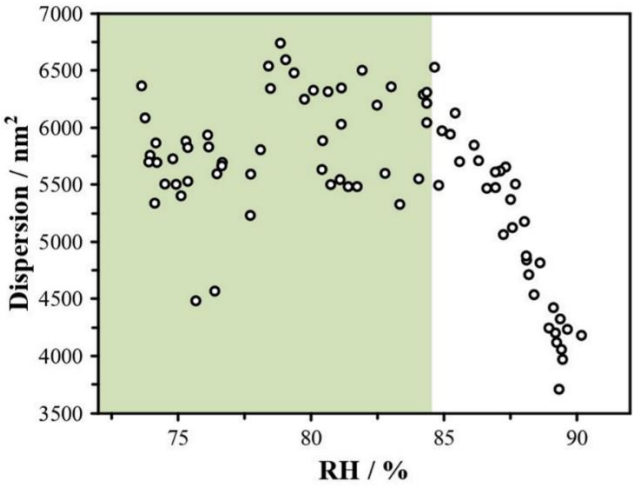

Figure 4.11: The reported dispersion for 1:1 4-NC:AS particles shows a plateau below 85% RH, indicating possible phase separation. Given the evidence presented in the other mixtures, a phase transformation at this RH is expected.

These observations support the 1:1 mixture forming a core-shell morphology where the resonant light is confined to the outer shell. With a core-shell structure, sharp MDR's are present allowing for the retrieval of size and RI, and accounting for the data shown in Figure 4.7A where the growth factor is still determined even in the LLPS region. MDRs become non-existent around 73% for 1:1 mixture, at which point size and RI are no longer retrieved since the particle is no longer homogenous. The 2:1 and 4:1 mixture exhibit a more obvious transformation in which the spectra, size, RI, and dispersion breakdown, supporting a transition from an aqueous to core-shell to partially engulfed morphology. The morphology adopted following LLPS will depend on the size of the particle and the spreading coefficient of the outer phase, which depends on the surface and interfacial tensions.[55,56] It is likely that the surface tension of the organic rich phase is greater than the salt rich phase, leading to a configuration with the organic on the outside. A partially engulfed morphology will arise when the interfacial tension is larger than the difference in

the surface tension between the salt and organic rich phases. Transitions from core-shell to partially engulfed may arise due to the dependence of the surface tension and interfacial tension on the composition, controlled by the RH.

Overall, these measurements indicate that SRH shifts to lower RH as the amount of inorganic material is increased, although the dependence is not strong. While a mass fraction dependence is not typically observed in organic-inorganic mixtures,[57] the dependence here likely arises due to the large dilution that occurs on addition of ammonium sulfate, given the large increase in average particle hygroscopicity. Although the water activity remains unchanged, as this is determined by the RH, the amount of water increases significantly and the activity of the solute is likely to change, leading to changes in the transition conditions. Additionally, we also observe transitions to different phase separated states, which may be ascribed to the different particle compositions and varying amounts of water due to the varying RH of the transition.[58,59] In mixtures of hydrophobic and hydrophilic components, a preference towards semi-engulfed morphologies is observed.[55,60]

4.3.2.3. Efflorescence and Deliquescence of Mixed Particles

An additional phase transition to a dry particle state was observed in all mixtures in the RH range of 22 – 42 %, with 15 out of the 22 particles effloresing within 22 – 33 % range. In general, the RH was lowered gradually to avoid spontaneous efflorescence as seen with pure 4-NC. Pure 4-NC typically effloresced within the RH range of 40 – 50 %, contributing to the idea that efflorescence in the mixtures is dominated by the presence of ammonium sulfate, which effloresces at around 32 – 42 % RH.[61,62] The addition of 4-NC lowered the

efflorescence point further than that of pure ammonium sulfate, but the effect did not clearly scale with the amount of 4-NC. This supports the idea that after phase separation occurs, the inorganic rich phase, in which efflorescence initiates, consists of the same composition at all mixing ratios.

Following efflorescence, all particles were exposed to an RH of approximately 95 % to identify the deliquescence RH. At 95% the 1:1, 2:1, and 4:1 mixtures showed spectra that contained a fluctuating mix of sharp and broad peaks. This is consistent with partial deliquescence of the AS, with solid 4-NC that resists solvation and scatters light randomly. Full deliquescence was not observed over the timescales explored here (several hours). The 5:1 mixture showed similar results but was observed to fully deliquesce occasionally (in two of six measured particles), indicating that the additional water content associated with the AS may be sufficient to solubilize the 4-NC. The four particles that did not immediately deliquesce were left at a high RH (> 95%) for upwards of 5 hours with no signs of deliquescence, indicating a thermodynamic rather than kinetic control over deliquescence. Deliquescence for two particles was achieved within a few minutes and the spectra remained well-resolved, indicating full deliquescence, and may be attributed to a slightly increased RH reached by the chamber.

4.3.3. Light Absorption of 4-NC in Pure and Mixed Particles

The wavenumber-dependent complex refractive index, $m(\nu) = n(\nu) + ik(\nu)$, of the aerosol particles was modeled using the effective oscillator model for the weakly absorbing AS and a single Lorentzian oscillator for the strongly absorbing 4-NC.[63–65] In this model, the real part of the refractive index, $n(\nu)$, and the imaginary part of the refractive index, $k(\nu)$, for an aqueous solution containing N weakly absorbing solutes and J strongly absorbing solutes are:

$$n(\nu) = 1 + \frac{2}{\pi}\sum_{\alpha=1}^{N} \phi_\alpha \frac{\tilde{B}_\alpha \tilde{\nu}_{0,\alpha}}{\tilde{\nu}_{0,\alpha}^2 - \nu^2} + \sum_{\alpha=1}^{J} \phi_\alpha B_{\delta,\alpha} + \frac{2}{\pi}\sum_{\alpha=1}^{J} \phi_\alpha \frac{B_\alpha \nu_{0,\alpha}\left(\nu_{0,\alpha}^2 - \nu^2 + (\Gamma_\alpha/2)^2\right)}{\left(\nu_{0,\alpha}^2 - \nu^2 + (\Gamma_\alpha/2)^2\right)^2 + (\nu\Gamma_\alpha)^2} + \phi_w\left(n^{(w)}(\nu) - 1\right) \quad (4.5)$$

$$k(\nu) = \frac{2\nu}{\pi}\sum_{\alpha=1}^{N} \phi_\alpha \frac{\tilde{B}_\alpha \tilde{\nu}_{0,\alpha} \tilde{\Gamma}_\alpha}{\left(\tilde{\nu}_{0,\alpha}^2 - \nu^2\right)^2} + \sum_{\alpha=1}^{J} \phi_\alpha \frac{B_\alpha}{\pi}\left(\frac{\Gamma_\alpha/2}{\left(\nu - \nu_{0,\alpha}\right)^2 + (\Gamma_\alpha/2)^2} - \frac{\Gamma_\alpha/2}{\left(\nu + \nu_{0,\alpha}\right)^2 + (\Gamma_\alpha/2)^2}\right) + \phi_w k^{(w)}(\nu) \quad (4.6)$$

where $\phi_\alpha$is the mass fraction of solute α, ϕ_w is the mass fraction of water, $n^{(w)}(\nu)$ is the real part of the refractive index of pure water and $k^{(w)}(\nu)$ is the imaginary part of the refractive index of pure water. The effective oscillator parameters for solute α are a constant, $\tilde{B}_\alpha$, resonant wavenumber, $\tilde{\nu}_{0,\alpha}$, and full-width at half-maximum, $\tilde{\Gamma}_\alpha$. The Lorentzian oscillator parameters for solute α are a constant, B_α, resonant wavenumber, $\nu_{0,\alpha}$, full-width at half-maximum, Γ_α, and a constant that accounts for optical transitions in the ultraviolet or higher energies, $B_{\delta,\alpha}$,. Finally, the wavenumber is $\nu = 1/\lambda$, where λ is the vacuum wavelength of light.

For water, $n^{(w)}(\nu)$ was calculated using the parameterization from Daimon et al.[66] and $k^{(w)}(\nu)$ was set to zero as the contribution of 4-NC to the imaginary part of the refractive index in the visible region of the spectrum will be several orders of magnitude larger than that of water. For AS, the oscillator parameters were taken from Bain et al.[63] Concerning

4-NC, based on UV-vis measurements of comparatively dilute binary aqueous solutions,[66,67] absorption in the visible region of the spectrum is dominated by the tail of strong bands in the near-UV. To model our measurements, we assumed that it was satisfactory to describe these bands using a single Lorentzian oscillator and that higher energy bands could be characterized by a constant. This meant that there were four unknown parameters in the model: B_α, $\nu_{0,\alpha}$, Γ_α, and $B_{\delta,\alpha}$, where α corresponds to 4-NC.

To determine the four unknown oscillator parameters for 4-NC, we simultaneously fit 25 spectra that were measured under different RH conditions for a range of AS to 4-NC mixing ratios. A differential evolution algorithm was used for the constrained global optimization.[68] Conditions were limited to those in which particles were aqueous and homogeneous (i.e. above the transition RH's noted earlier). Simulated scattered light intensity was calculated by integrating the first component of the Stokes vector for the scattered light from the particle over the appropriate angular range for the collection objective used in our EDB.[65,69] To construct a single simulated spectrum, this calculation was repeated at each measured wavelength. For a single point in the four-dimensional search space the oscillator parameters were the same for all 25 spectra, and the radius of best-fit for the pure and 1:1 case were constrained by measurements at longer wavelengths. The radii for the 10:1 and 100:1 cases were determined from the spectra at 420 to 520 nm. The mass fractions of water, 4-NC, and AS for each of the 25 measurements were known from the measurements reported herein. Figure 4.12 shows an example of the resulting spectra comparison with the oscillator parameters of best-fit, including uncertainty, for pure 4-NC listed in the caption.

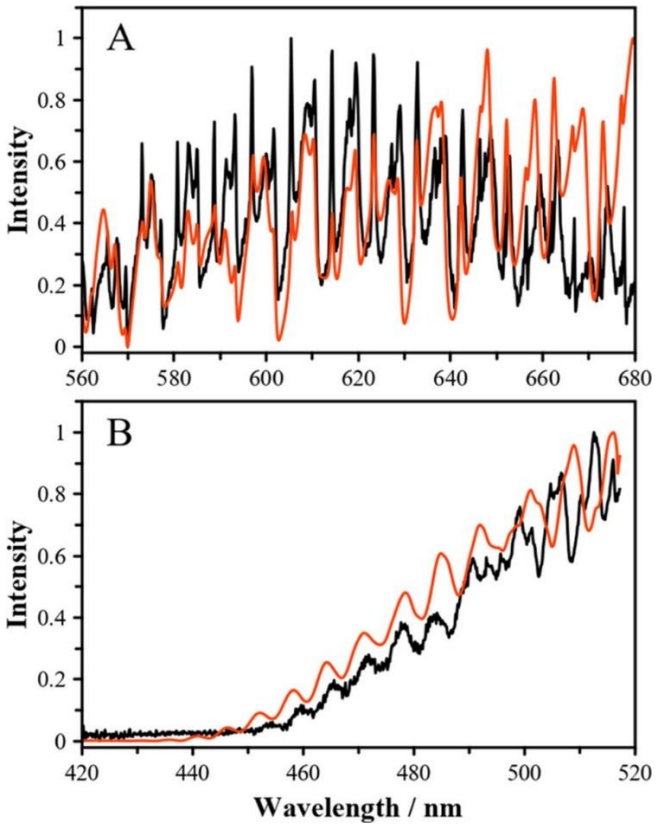

Figure 4.12: Measured spectra (black) compared against the global best-fit Mie theory simulation (red) using the results of the oscillator model to account for the influence of light absorption. The Lorentzian oscillator parameters of best-fit for 4-NC were: $B_{\alpha} = (3.43 \pm 0.82) \times 10^{-5}\, nm^{-1}$, $\nu_{0,\alpha} = (2.47 \pm 0.01) \times 10^{-3}\, nm^{-1}$, $\Gamma_{\alpha} = (1.36 \pm 0.48) \times 10^{-4}\, nm^{-1}$, and $B_{\delta,\alpha} = 0.594 \pm 0.010$. The radius used in the fit was established from spectra measured at longer wavelengths (panel A) using the methods described in the text.

The pure component case shows good agreement across all wavelengths with respect to the relative scattering intensity (Pearson correlation coefficients >0.95). The fine structure of the spectra is not fully reproduced, and these discrepancies may arise due to systematic errors in how the dispersion is treated or limitations of the effective oscillator model. A similar trend is noted for the 1:1 mixture (Figure 4.13A), indicating the mass fraction mixing rules used in the oscillator model is also satisfactory. For the 10:1 and 100:1 cases (Figures 4.13B and 4.13C), excellent agreement is observed across the entire wavelength range.

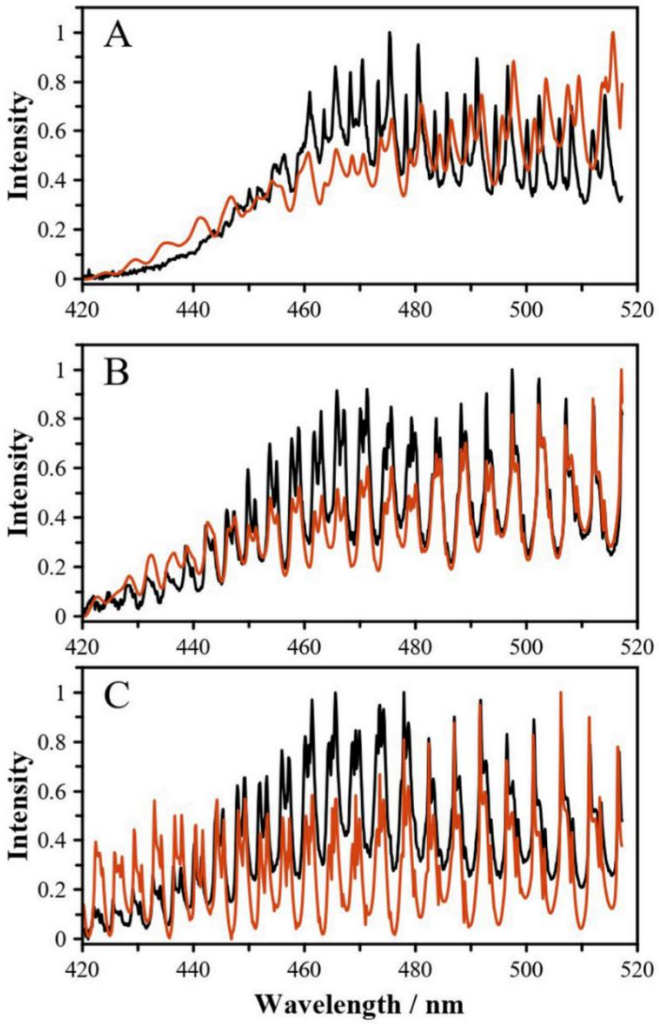

Figure 4.13: Best fit spectra for (A) 1:1; (B) 1:10; (C) 1:100 mixtures of 4-NC and AS derived using the oscillator model, as described in the main text.

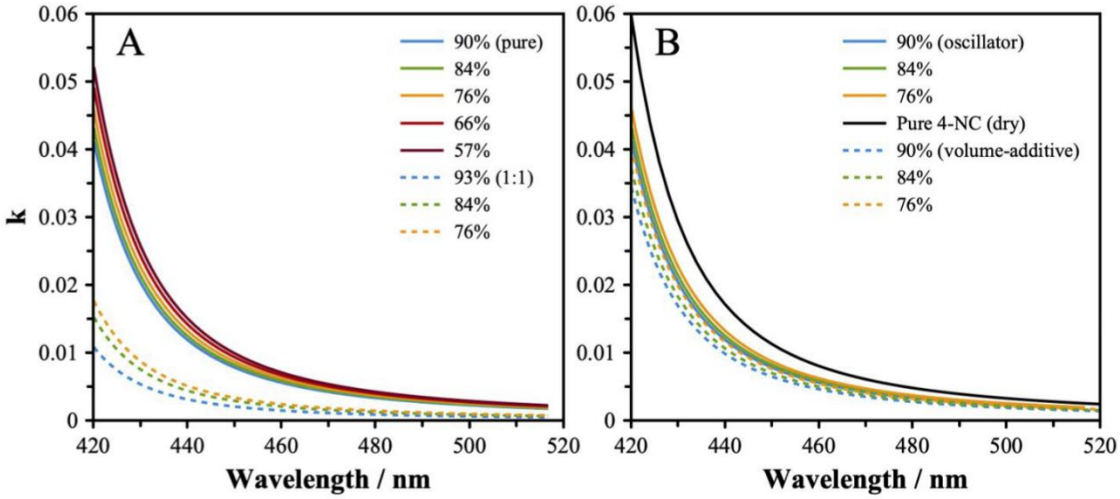

Figure 4.14: (A) The imaginary component of the complex refractive index for pure 4-NC particles (solid lines) and 1:1 mixtures with AS (dashed lines) across the range of measured RH conditions using Equation 4, the best-fit oscillator parameters and the mass fractions derived from this work. (B) The oscillator model (solid lines) compared to a volume-additive approach (dashed lined) for pure 4-NC particles at different RHs.

In Figure 4.14A, we show the value of k as a function of the wavelength for pure 4-NC and 1:1 mixture across the measured RH range based on the best-fit oscillator parameters and the mass fractions derived from this work. The dilution effect of AS significantly reduces the light absorption of the particles at the same RH, with a greater RH dependence observed due to the increased averaged particle hygroscopicity. The uncertainty range in k resulting from the uncertainty in the oscillator coefficients is shown in Figure 4.15.

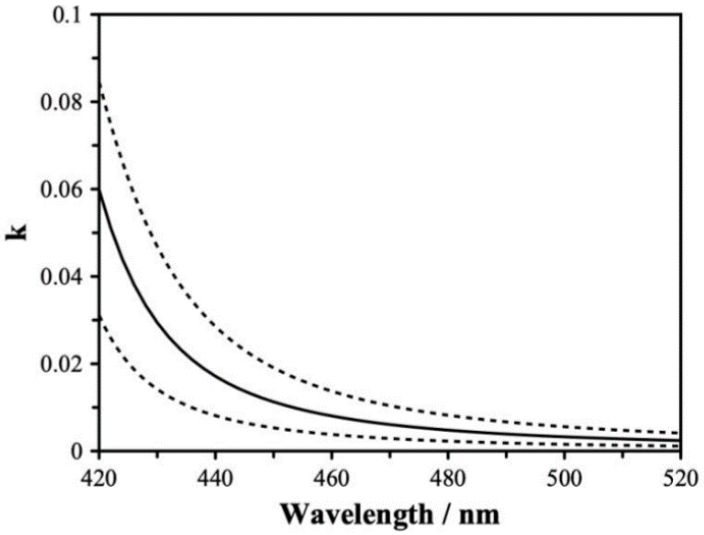

Figure 4.15: The imaginary component of the refractive index for pure 4-NC particles (solid line), as determined using the oscillator parameters reported in Figure 4.4. The dash lines indicate the uncertainty in k based on the uncertainty range in the oscillator parameters.

We can explore the application of a simple volume-additive approach to this system by calculating the imaginary component of pure 4-NC, using Equation 4.6, as a function of wavelength (shown in Figure 4.14B) and using the radial growth factor data to obtain the volume fractions. We find that the volume-additive approach leads to an under-prediction of $k(\lambda)$, in agreement with previous work that also notes an under-prediction using volume-additive methods.[51] These observations point to the inability for volume-additive mixing rules to fully account for absorption using the imaginary part of the refractive index.

4.4. Environmental Implications

In this work, we have reported the hygroscopicity of pure 4-nitrocatechol, showing growth factors consistent with low solubility material and, thus, likely minimal impact on cloud formation. However, in mixtures with ammonium sulfate, these particles become increasingly hygroscopic. This has important implications for their role in cloud formation

and their reactivity in the atmosphere. These mixtures have also shown the ability to transition to a variety of morphologies, due to their lack of miscibility, including core-shell and partially engulfed phase separated states. We have demonstrated that at low RH, mixed particles containing 4-NC and ammonium sulfate will experience phase transitions. We identified the RH at which phase separation occurs as a function of the amount of ammonium sulfate, with a slight decrease in the separation RH as the amount of AS is increased. Phase separation in this system was found to be reversible with respect to increased RH up to the efflorescence point, after which particles generally resist water uptake and do not deliquesce even at high RH. This has important implications for particles in the atmosphere that experience a range of RH conditions over their lifetime, as the RH history will play a role in predicting their phase state. We further summarize our results and discuss the environmental impacts in the following subsections.

4.4.1. Cloud Formation

The formation of a cloud from aerosol particles requires sufficiently hygroscopic and soluble material. 4-NC alone has been shown to have low hygroscopicity and, by extrapolation, it is likely that most nitro-aromatic BrC compounds are similarly poor CCN nuclei. However, pure 4-NC particles are not encountered in the atmosphere, and our results indicate the presence of inorganic material will significantly increase the hygroscopic growth and CCN activity of the aerosol. CCN is further influenced by surface tension, and while we do not report measurements of surface tension, the observation that phase separation occurs may be an indicator that 4-NC is present at the surface. Phase-

separated states themselves will not affect CCN activation unless the transition occurs at very high RH, or there are kinetic limitations to water uptake.[47,70]

4.4.2. Heterogeneous Reactions

The reaction rates for processes involving the uptake of reactive gas phase species have been shown to depend on RH in several studies.[71,72] The amount of water impacts the viscosity and rate of diffusion, and may influence reaction pathways, leading to changes in the chemical evolution of the particles. Heterogeneous reactions are known to evolve the optical properties of brown carbon, connecting hygroscopicity, phase, reactivity, and optical properties in a complex multifaceted problem.[32] Given the hygroscopic growth observed in even pure 4-NC, it is likely that an RH dependence to its heterogeneous reactivity will also be observed. The formation of LLPS states is also expected to lead to changes in heterogeneous reactivity, although the extent of these effects is not clear.[73]

4.4.3. Light Absorption

Using an oscillator model for treating the imaginary part of the complex refractive index, a best fit was performed to the data spanning a range of compositions. Values were established for 4-NC and generally good agreement was observed across all wavelengths in the visible region of the spectrum. These measurements allow the influence of RH and composition on the extent of light absorption to be interrogated, yielding parameters that may be used to model the influence of these particles on light absorption of aerosol in the atmosphere. Alternative experimental methods and analysis will be necessary to characterize the RI in the near-UV. Although we cannot probe light absorption in LLPS particles, these morphologies are known to affect light scattering and further work is

necessary to fully understand the implications of LLPS for light absorption in BrC aerosol. With the increasing prevalence of wildfires providing a significant source of BrC to the atmosphere, the role of these light absorbing particles is becoming more important. A detailed understanding of their light scattering properties and the synergistic role of co-solutes, phase morphology and hygroscopicity will be vital for predicting their environmental impacts.

Overall, we present a comprehensive study on the hygroscopicity, phase morphology and optical properties of a common brown carbon chromophore in its pure state and in mixtures with an atmospherically relevant salt. Such studies will be necessary to fully constrain the influence of BrC aerosol in the atmosphere and reduce the uncertainty with respect to their light scattering and cloud interactions.

4.5. References

(1) Haywood, J.; Boucher, O. Estimates of the Direct and Indirect Radiative Forcing Due to Tropospheric Aerosols: A Review. *Rev. Geophys.* **2000**, *38* (4), 513–543. https://doi.org/10.1029/1999RG000078.

(2) Lohmann, U.; Feichter, J. Global Indirect Aerosol Effects: A Review. *Atmos Chem Phys* **2005**, 23.

(3) Andreae, M. O.; Gelencsér, A. Black Carbon or Brown Carbon? The Nature of Light-Absorbing Carbonaceous Aerosols. *Atmos Chem Phys* **2006**, 19.

(4) Tang, M.; Alexander, J. M.; Kwon, D.; Estillore, A. D.; Laskina, O.; Young, M. A.; Kleiber, P. D.; Grassian, V. H. Optical and Physicochemical Properties of Brown Carbon Aerosol: Light Scattering, FTIR Extinction Spectroscopy, and Hygroscopic Growth. *J. Phys. Chem. A* **2016**, *120* (24), 4155–4166. https://doi.org/10.1021/acs.jpca.6b03425.

(5) Xu, R.; Yu, P.; Abramson, M. J.; Johnston, F. H.; Samet, J. M.; Bell, M. L.; Haines, A.; Ebi, K. L.; Li, S.; Guo, Y. Wildfires, Global Climate Change, and Human Health. *N Engl J Med* **2020**, 9.

(6) Kizer, K. W. Extreme Wildfires—A Growing Population Health and Planetary Problem. *JAMA* **2020**, *324* (16), 1605. https://doi.org/10.1001/jama.2020.19334.

(7) Kelly, F. J.; Fussell, J. C. Global Nature of Airborne Particle Toxicity and Health Effects: A Focus on Megacities, Wildfires, Dust Storms and Residential Biomass Burning. *Toxicol. Res.* **2020**, *9* (4), 331–345. https://doi.org/10.1093/toxres/tfaa044.

(8) Devi, J. J.; Bergin, M. H.; Mckenzie, M.; Schauer, J. J.; Weber, R. J. Contribution of Particulate Brown Carbon to Light Absorption in the Rural and Urban Southeast US. *Atmos. Environ.* **2016**, *136*, 95–104. https://doi.org/10.1016/j.atmosenv.2016.04.011.

(9) Chen, Y.; Xie, X.; Shi, Z.; Li, Y.; Gai, X.; Wang, J.; Li, H.; Wu, Y.; Zhao, X.; Chen, M.; Ge, X. Brown Carbon in Atmospheric Fine Particles in Yangzhou, China: Light Absorption Properties and Source Apportionment. *Atmospheric Res.* **2020**, *244*, 105028. https://doi.org/10.1016/j.atmosres.2020.105028.

(10) Rossiello, M. R.; Szema, A. Health Effects of Climate Change-Induced Wildfires and Heatwaves. *Cureus* **2019**. https://doi.org/10.7759/cureus.4771.

(11) Sun, Q.; Miao, C.; Hanel, M.; Borthwick, A. G. L.; Duan, Q.; Ji, D.; Li, H. Global Heat Stress on Health, Wildfires, and Agricultural Crops under Different Levels of Climate Warming. *Environ. Int.* **2019**, *128*, 125–136. https://doi.org/10.1016/j.envint.2019.04.025.

(12) Finewax, Z.; de Gouw, J. A.; Ziemann, P. J. Identification and Quantification of 4-Nitrocatechol Formed from OH and NO_3 Radical-Initiated Reactions of Catechol in Air in the Presence of NO_x : Implications for Secondary Organic Aerosol Formation from Biomass Burning. *Environ. Sci. Technol.* **2018**, *52* (4), 1981–1989. https://doi.org/10.1021/acs.est.7b05864.

(13) Lack, D. A.; Langridge, J. M.; Bahreini, R.; Cappa, C. D.; Middlebrook, A. M.; Schwarz, J. P. Brown Carbon and Internal Mixing in Biomass Burning Particles. *Proc. Natl. Acad. Sci.* **2012**, *109* (37), 14802–14807. https://doi.org/10.1073/pnas.1206575109.

(14) Laskin, A.; Laskin, J.; Nizkorodov, S. A. Chemistry of Atmospheric Brown Carbon. *Chem. Rev.* **2015**, *115* (10), 4335–4382. https://doi.org/10.1021/cr5006167.

(15) Chakrabarty, R. K.; Gyawali, M.; Yatavelli, R. L. N.; Pandey, A.; Watts, A. C.; Knue, J.; Chen, L.-W. A.; Pattison, R. R.; Tsibart, A.; Samburova, V.; Moosmüller, H. Brown Carbon Aerosols from Burning of Boreal Peatlands: Microphysical Properties, Emission Factors, and Implications for Direct Radiative Forcing. *Atmospheric Chem. Phys.* **2016**, *16* (5), 3033–3040. https://doi.org/10.5194/acp-16-3033-2016.

(16) Bond, T. C. Spectral Dependence of Visible Light Absorption by Carbonaceous Particles Emitted from Coal Combustion. *Geophys. Res. Lett.* **2001**, *28* (21), 4075–4078. https://doi.org/10.1029/2001GL013652.

(17) Morville, S.; Scheyer, A.; Mirabel, P.; Millet, M. A Multiresidue Method for the Analysis of Phenols and Nitrophenols in the Atmosphere. *J. Environ. Monit.* **2004**, *6* (12), 963. https://doi.org/10.1039/b408756a.

(18) Saleh, R.; Marks, M.; Heo, J.; Adams, P. J.; Donahue, N. M.; Robinson, A. L. Contribution of Brown Carbon and Lensing to the Direct Radiative Effect of Carbonaceous Aerosols from Biomass and Biofuel Burning Emissions. *J. Geophys. Res. Atmospheres* **2015**, *120* (19). https://doi.org/10.1002/2015JD023697.

(19) Zhang, Y.; Albinet, A.; Petit, J.-E.; Jacob, V.; Chevrier, F.; Gille, G.; Pontet, S.; Chrétien, E.; Dominik-Sègue, M.; Levigoureux, G.; Močnik, G.; Gros, V.; Jaffrezo, J.-L.; Favez, O. Substantial Brown Carbon Emissions from Wintertime Residential Wood Burning over France. *Sci. Total Environ.* **2020**, *743*, 140752. https://doi.org/10.1016/j.scitotenv.2020.140752.

(20) Browne, E. C.; Zhang, X.; Franklin, J. P.; Ridley, K. J.; Kirchstetter, T. W.; Wilson, K. R.; Cappa, C. D.; Kroll, J. H. Effect of Heterogeneous Oxidative Aging on Light Absorption by Biomass Burning Organic Aerosol. *Aerosol Sci. Technol.* **2019**, *53* (6), 663–674. https://doi.org/10.1080/02786826.2019.1599321.

(21) Saleh, R. From Measurements to Models: Toward Accurate Representation of Brown Carbon in Climate Calculations. *Curr. Pollut. Rep.* **2020**, *6* (2), 90–104. https://doi.org/10.1007/s40726-020-00139-3.

(22) De Haan, D. O.; Jansen, K.; Rynaski, A. D.; Sueme, W. R. P.; Torkelson, A. K.; Czer, E. T.; Kim, A. K.; Rafla, M. A.; De Haan, A. C.; Tolbert, M. A. Brown Carbon Production by Aqueous-Phase Interactions of Glyoxal and SO_2. *Environ. Sci. Technol.* **2020**, *54* (8), 4781–4789. https://doi.org/10.1021/acs.est.9b07852.

(23) Teich, M.; van Pinxteren, D.; Wang, M.; Kecorius, S.; Wang, Z.; Müller, T.; Močnik, G.; Herrmann, H. Contributions of Nitrated Aromatic Compounds to the Light Absorption of Water-Soluble and Particulate Brown Carbon in Different Atmospheric Environments in Germany and China. *Atmospheric Chem. Phys.* **2017**, *17* (3), 1653–1672. https://doi.org/10.5194/acp-17-1653-2017.

(24) Akherati, A.; He, Y.; Coggon, M. M.; Koss, A. R.; Hodshire, A. L.; Sekimoto, K.; Warneke, C.; de Gouw, J.; Yee, L.; Seinfeld, J. H.; Onasch, T. B.; Herndon, S. C.; Knighton, W. B.; Cappa, C. D.; Kleeman, M. J.; Lim, C. Y.; Kroll, J. H.; Pierce, J. R.; Jathar, S. H. Oxygenated Aromatic Compounds Are Important Precursors of Secondary Organic Aerosol in Biomass-Burning Emissions. *Environ. Sci. Technol.* **2020**, *54* (14), 8568–8579. https://doi.org/10.1021/acs.est.0c01345.

(25) Li, X.; Yang, Y.; Liu, S.; Zhao, Q.; Wang, G.; Wang, Y. Light Absorption Properties of Brown Carbon (BrC) in Autumn and Winter in Beijing: Composition, Formation and Contribution of Nitrated Aromatic Compounds. *Atmos. Environ.* **2020**, *223*, 117289. https://doi.org/10.1016/j.atmosenv.2020.117289.

(26) Li, C.; He, Q.; Hettiyadura, A. P. S.; Käfer, U.; Shmul, G.; Meidan, D.; Zimmermann, R.; Brown, S. S.; George, C.; Laskin, A.; Rudich, Y. Formation of Secondary Brown Carbon in Biomass Burning Aerosol Proxies through NO_3 Radical Reactions. *Environ. Sci. Technol.* **2020**, *54* (3), 1395–1405. https://doi.org/10.1021/acs.est.9b05641.

(27) Bai, Z.; Zhang, L.; Cheng, Y.; Zhang, W.; Mao, J.; Chen, H.; Li, L.; Wang, L.; Chen, J. Water/Methanol-Insoluble Brown Carbon Can Dominate Aerosol-Enhanced Light Absorption in Port Cities. *Environ. Sci. Technol.* **2020**, *54* (23), 14889–14898. https://doi.org/10.1021/acs.est.0c03844.

(28) Li, J.; Zhang, Q.; Wang, G.; Li, J.; Wu, C.; Liu, L.; Wang, J.; Jiang, W.; Li, L.; Ho, K. F.; Cao, J. Optical Properties and Molecular Compositions of Water-Soluble and Water-Insoluble Brown Carbon (BrC) Aerosols in Northwest China. *Atmospheric Chem. Phys.* **2020**, *20* (8), 4889–4904. https://doi.org/10.5194/acp-20-4889-2020.

(29) Satish, R.; Rastogi, N.; Singh, A.; Singh, D. Change in Characteristics of Water-Soluble and Water-Insoluble Brown Carbon Aerosols during a Large-Scale Biomass Burning. *Environ. Sci. Pollut. Res.* **2020**, *27* (26), 33339–33350. https://doi.org/10.1007/s11356-020-09388-7.

(30) Forrister, H.; Liu, J.; Scheuer, E.; Dibb, J.; Ziemba, L.; Thornhill, K. L.; Anderson, B.; Diskin, G.; Perring, A. E.; Schwarz, J. P.; Campuzano-Jost, P.; Day, D. A.; Palm, B. B.; Jimenez, J. L.; Nenes, A.; Weber, R. J. Evolution of Brown Carbon in Wildfire Plumes. *Geophys. Res. Lett.* **2015**, *42* (11), 4623–4630. https://doi.org/10.1002/2015GL063897.

(31) Moise, T.; Flores, J. M.; Rudich, Y. Optical Properties of Secondary Organic Aerosols and Their Changes by Chemical Processes. *Chem. Rev.* **2015**, *115* (10), 4400–4439. https://doi.org/10.1021/cr5005259.

(32) Hems, R. F.; Schnitzler, E. G.; Liu-Kang, C.; Cappa, C. D.; Abbatt, J. P. D. Aging of Atmospheric Brown Carbon Aerosol. *ACS Earth Space Chem.* **2021**, *5* (4), 722–748. https://doi.org/10.1021/acsearthspacechem.0c00346.

(33) Freedman, M. A. Liquid–Liquid Phase Separation in Supermicrometer and Submicrometer Aerosol Particles. *Acc. Chem. Res.* **2020**, *53* (6), 1102–1110. https://doi.org/10.1021/acs.accounts.0c00093.

(34) Freedman, M. A. Phase Separation in Organic Aerosol. *Chem. Soc. Rev.* **2017**, *46* (24), 7694–7705. https://doi.org/10.1039/C6CS00783J.

(35) Richards, D. S.; Trobaugh, K. L.; Hajek-Herrera, J.; Price, C. L.; Sheldon, C. S.; Davies, J. F.; Davis, R. D. Ion-Molecule Interactions Enable Unexpected Phase Transitions in Organic-Inorganic Aerosol. *Sci. Adv.* **2020**, *6* (47), eabb5643. https://doi.org/10.1126/sciadv.abb5643.

(36) Fard, M. M.; Krieger, U. K.; Peter, T. Shortwave Radiative Impact of Liquid–Liquid Phase Separation in Brown Carbon Aerosols. *Atmospheric Chem. Phys.* **2018**, *18* (18), 13511–13530. https://doi.org/10.5194/acp-18-13511-2018.

(37) Brown, H.; Liu, X.; Pokhrel, R.; Murphy, S.; Lu, Z.; Saleh, R.; Mielonen, T.; Kokkola, H.; Bergman, T.; Myhre, G.; Skeie, R. B.; Watson-Paris, D.; Stier, P.; Johnson, B.; Bellouin, N.; Schulz, M.; Vakkari, V.; Beukes, J. P.; van Zyl, P. G.; Liu, S.; Chand, D. Biomass Burning Aerosols in Most Climate Models Are Too Absorbing. *Nat. Commun.* **2021**, *12* (1), 277. https://doi.org/10.1038/s41467-020-20482-9.

(38) Vidović, K.; Lašič Jurković, D.; Šala, M.; Kroflič, A.; Grgić, I. Nighttime Aqueous-Phase Formation of Nitrocatechols in the Atmospheric Condensed Phase. *Environ. Sci. Technol.* **2018**, *52* (17), 9722–9730. https://doi.org/10.1021/acs.est.8b01161.

(39) Kucinski, T. M.; Ott, E.-J. E.; Freedman, M. A. Flash Freeze Flow Tube to Vitrify Aerosol Particles at Fixed Relative Humidity Values. *Anal. Chem.* **2020**, *92* (7), 5207–5213. https://doi.org/10.1021/acs.analchem.9b05757.

(40) Davies, J. F. Mass, Charge, and Radius of Droplets in a Linear Quadrupole Electrodynamic Balance. *Aerosol Sci. Technol.* **2019**, *53* (3), 309–320. https://doi.org/10.1080/02786826.2018.1559921.

(41) Davies, J. F.; Haddrell, A. E.; Reid, J. P. Time-Resolved Measurements of the Evaporation of Volatile Components from Single Aerosol Droplets. *Aerosol Sci. Technol.* **2012**, *46* (6), 666–677. https://doi.org/10.1080/02786826.2011.652750.

(42) Choczynski, J. M.; Kaur Kohli, R.; Sheldon, C. S.; Price, C. L.; Davies, J. F. A Dual-Droplet Approach for Measuring the Hygroscopicity of Aqueous Aerosol. *Atmospheric Meas. Tech.* **2021**, *14* (7), 5001–5013. https://doi.org/10.5194/amt-14-5001-2021.

(43) Lew, L. J. N.; Ting, M. V.; Preston, T. C. Determining the Size and Refractive Index of Homogeneous Spherical Aerosol Particles Using Mie Resonance Spectroscopy. *Appl. Opt.* **2018**, *57* (16), 4601. https://doi.org/10.1364/AO.57.004601.

(44) Price, C. L.; Bain, A.; Wallace, B. J.; Preston, T. C.; Davies, J. F. Simultaneous Retrieval of the Size and Refractive Index of Suspended Droplets in a Linear Quadrupole Electrodynamic Balance. *J. Phys. Chem. A* **2020**, *124* (9), 1811–1820. https://doi.org/10.1021/acs.jpca.9b10748.

(45) Preston, T. C.; Reid, J. P. Determining the Size and Refractive Index of Microspheres Using the Mode Assignments from Mie Resonances. *J Opt Soc Am A 32* (11), 2210–2217.

(46) Bohren, C. F.; Huffman, D. R. *Absorption and Scattering of Light by Small Particles*; John Wiley and Sons: New York, 1983.

(47) Liu, P.; Song, M.; Zhao, T.; Gunthe, S. S.; Ham, S.; He, Y.; Qin, Y. M.; Gong, Z.; Amorim, J. C.; Bertram, A. K.; Martin, S. T. Resolving the Mechanisms of Hygroscopic Growth and Cloud Condensation Nuclei Activity for Organic Particulate Matter. *Nat. Commun.* **2018**, *9* (1), 4076. https://doi.org/10.1038/s41467-018-06622-2.

(48) Rickards, A. M. J.; Miles, R. E. H.; Davies, J. F.; Marshall, F. H.; Reid, J. P. Measurements of the Sensitivity of Aerosol Hygroscopicity and the κ Parameter to the O/C Ratio. *J. Phys. Chem. A* **2013**, *117* (51), 14120–14131. https://doi.org/10.1021/jp407991n.

(49) Wex, H.; Ziese, M.; Kiselev, A.; Henning, S.; Stratmann, F. Deliquescence and Hygroscopic Growth of Succinic Acid Particles Measured with LACIS. *Geophys. Res. Lett.* **2007**, *34* (17), L17810. https://doi.org/10.1029/2007GL030185.

(50) Parsons, M. T.; Mak, J.; Lipetz, S. R.; Bertram, A. K. Deliquescence of Malonic, Succinic, Glutaric, and Adipic Acid Particles: DELIQUESCENCE OF ORGANIC ACID PARTICLES. *J. Geophys. Res. Atmospheres* **2004**, *109* (D6), n/a-n/a. https://doi.org/10.1029/2003JD004075.

(51) Michel Flores, J.; Bar-Or, R. Z.; Bluvshtein, N.; Abo-Riziq, A.; Kostinski, A.; Borrmann, S.; Koren, I.; Koren, I.; Rudich, Y. Absorbing Aerosols at High Relative Humidity: Linking Hygroscopic Growth to Optical Properties. *Atmospheric Chem. Phys.* **2012**, *12* (12), 5511–5521. https://doi.org/10.5194/acp-12-5511-2012.

(52) Clegg, S. L.; Brimblecombe, P.; Wexler, A. S. Thermodynamic Model of the System H^+–NH_4^+–Na^+–SO_4^{2-}–NO_3^-–Cl^-–H_2O at 298.15 K. *J. Phys. Chem. A* **1998**, *102* (12), 2155–2171. https://doi.org/10.1021/jp973043j.

(53) Petters, M. D.; Kreidenweis, S. M. A Single Parameter Representation of Hygroscopic Growth and Cloud Condensation Nucleus Activity. *Atmos Chem Phys* **2007**, 11.

(54) Sullivan, R. C.; Boyer-Chelmo, H.; Gorkowski, K.; Beydoun, H. Aerosol Optical Tweezers Elucidate the Chemistry, Acidity, Phase Separations, and Morphology of Atmospheric Microdroplets. *Acc. Chem. Res.* **2020**, *53* (11), 2498–2509. https://doi.org/10.1021/acs.accounts.0c00407.

(55) Stewart, D. J.; Cai, C.; Nayler, J.; Preston, T. C.; Reid, J. P.; Krieger, U. K.; Marcolli, C.; Zhang, Y. H. Liquid–Liquid Phase Separation in Mixed Organic/Inorganic Single Aqueous Aerosol Droplets. *J. Phys. Chem. A* **2015**, *119* (18), 4177–4190. https://doi.org/10.1021/acs.jpca.5b01658.

(56) Song, M.; Marcolli, C.; Krieger, U. K.; Lienhard, D. M.; Peter, T. Morphologies of Mixed Organic/Inorganic/Aqueous Aerosol Droplets. *Faraday Discuss.* **2013**, *165*, 289. https://doi.org/10.1039/c3fd00049d.

(57) Song, M.; Marcolli, C.; Krieger, U. K.; Zuend, A.; Peter, T. Liquid-Liquid Phase Separation and Morphology of Internally Mixed Dicarboxylic Acids/Ammonium Sulfate/Water Particles. *Atmospheric Chem. Phys.* **2012**, *12* (5), 2691–2712. https://doi.org/10.5194/acp-12-2691-2012.

(58) Altaf, M. B.; Zuend, A.; Freedman, M. A. Role of Nucleation Mechanism on the Size Dependent Morphology of Organic Aerosol. *Chem. Commun.* **2016**, *52* (59), 9220–9223. https://doi.org/10.1039/C6CC03826C.

(59) Kucinski, T. M.; Dawson, J. N.; Freedman, M. A. Size-Dependent Liquid–Liquid Phase Separation in Atmospherically Relevant Complex Systems. *J. Phys. Chem. Lett.* **2019**, *10* (21), 6915–6920. https://doi.org/10.1021/acs.jpclett.9b02532.

(60) Reid, J. P.; Dennis-Smither, B. J.; Kwamena, N.-O. A.; Miles, R. E. H.; Hanford, K. L.; Homer, C. J. The Morphology of Aerosol Particles Consisting of Hydrophobic and Hydrophilic Phases: Hydrocarbons, Alcohols and Fatty Acids as the Hydrophobic Component. *Phys. Chem. Chem. Phys.* **2011**, *13* (34), 15559. https://doi.org/10.1039/c1cp21510h.

(61) Gao, Y.; Chen, S. B.; Yu, L. E. Efflorescence Relative Humidity for Ammonium Sulfate Particles. *J. Phys. Chem. A* **2006**, *110* (24), 7602–7608. https://doi.org/10.1021/jp057574g.

(62) Martin, S. T. Phase Transitions of Aqueous Atmospheric Particles. *Chem. Rev.* **2000**, *100* (9), 3403–3454. https://doi.org/10.1021/cr990034t.

(63) Bain, A.; Preston, T. C. The Wavelength-Dependent Optical Properties of Weakly Absorbing Aqueous Aerosol Particles. *Chem. Commun.* **2020**, *56* (63), 8928–8931. https://doi.org/10.1039/D0CC02737E.

(64) Bain, A.; Rafferty, A.; Preston, T. C. The Wavelength-Dependent Complex Refractive Index of Hygroscopic Aerosol Particles and Other Aqueous Media: An Effective Oscillator Model. *Geophys. Res. Lett.* **2019**, *46* (17–18), 10636–10645. https://doi.org/10.1029/2019GL084568.

(65) Bain, A.; Preston, T. C. Mie Scattering from Strongly Absorbing Airborne Particles in a Photophoretic Trap. *J. Appl. Phys.* **2019**, *125* (9), 093101. https://doi.org/10.1063/1.5082157.

(66) Cornard, J.-P.; Rasmiwetti; Merlin, J.-C. Molecular Structure and Spectroscopic Properties of 4-Nitrocatechol at Different PH: UV–Visible, Raman, DFT and TD-DFT Calculations. *Chem. Phys.* **2005**, *309* (2–3), 239–249. https://doi.org/10.1016/j.chemphys.2004.09.020.

(67) Daimon, M.; Masumura, A. Measurement of the Refractive Index of Distilled Water from the Near-Infrared Region to the Ultraviolet Region. *Appl. Opt.* **2007**, *46* (18), 3811. https://doi.org/10.1364/AO.46.003811.

(68) Price, K.; Storn, R. M.; Lampinen, J. A. *Differential Evolution A Practical Approach to Global Optimization*, Aufl. 2005.; Springer Berlin: Berlin, 2014.

(69) Rothe, T.; Schmitz, M.; Kienle, A. Angular and Spectrally Resolved Investigation of Single Particles by Darkfield Scattering Microscopy. *J. Biomed. Opt.* **2012**, *17* (11), 117006. https://doi.org/10.1117/1.JBO.17.11.117006.

(70) Ovadnevaite, J.; Zuend, A.; Laaksonen, A.; Sanchez, K. J.; Roberts, G.; Ceburnis, D.; Decesari, S.; Rinaldi, M.; Hodas, N.; Facchini, M. C.; Seinfeld, J. H.; O' Dowd, C. Surface Tension Prevails over Solute Effect in Organic-Influenced Cloud Droplet Activation. *Nature* **2017**, *546* (7660), 637–641. https://doi.org/10.1038/nature22806.

(71) Li, Z.; Smith, K. A.; Cappa, C. D. Influence of Relative Humidity on the Heterogeneous Oxidation of Secondary Organic Aerosol. *Atmospheric Chem. Phys.* **2018**, *18* (19), 14585–14608. https://doi.org/10.5194/acp-18-14585-2018.

(72) Davies, J. F.; Wilson, K. R. Nanoscale Interfacial Gradients Formed by the Reactive Uptake of OH Radicals onto Viscous Aerosol Surfaces. *Chem. Sci.* **2015**, *6* (12), 7020–7027. https://doi.org/10.1039/C5SC02326B.

(73) Lam, H. K.; Xu, R.; Choczynski, J.; Davies, J. F.; Ham, D.; Song, M.; Zuend, A.; Li, W.; Tse, Y.-L. S.; Chan, M. N. Effects of Liquid–Liquid Phase Separation and Relative Humidity on the Heterogeneous OH Oxidation of Inorganic–Organic Aerosols: Insights from Methylglutaric Acid and Ammonium Sulfate Particles. *Atmospheric Chem. Phys.* **2021**, *21* (3), 2053–2066. https://doi.org/10.5194/acp-21-2053-2021.

CHAPTER V

Connecting the Phase State and Volatility of Dicarboxylic Acids at Elevated Temperature

5.1. Introduction

The partitioning of organic molecules between vapor and condensed phases is important in a wide range of scientific disciplines. In the atmosphere, gas phase oxidation leads to the production of semi-volatile and low volatility compounds that contribute to the formation of secondary organic aerosol.[1] Further evaporation and condensation of semi-volatile organic molecules drives changes in the chemical composition and size distribution of these aerosol particles over time.[2–4] In indoor environments, the vaporization of semi-volatile organics from solvents, paints, and cooking oils (so-called volatile chemical products) plays an important role in regulating air quality.[5,6] In engineering, the vaporization of fuel is a necessary step in the process of combustion, and the evaporation of components found in lubricating and cooling oils affects their long-term function.[7–10] The vapor pressure of volatile and semi-volatile compounds plays an important role in the function, characterization, and environmental impacts of these systems.

The vapor pressure is a thermodynamic quantity derived from the equilibrium pressure of a compound in the gas phase above a pure condensed phase of that substance. In mixtures of organic substances, the effective vapor pressure of each component varies with its mole fraction and chemical activity, which may be measured or derived from theory.[11] Additional complicating factors arise when both intra- and inter-molecular interactions are possible between the condensed phase species. In the homologous series of terminal

dicarboxylic acids (malonic, succinic, glutaric, adipic acid, and so on), a distinct odd-even alteration of properties, such as solubility and melting point, with the number of carbon atoms is observed.[11–14] This is attributed to the ways in which the even and odd molecules, respectively, can arrange and form intra- and inter-molecular hydrogen bonds in solution. These interactions change the thermodynamics of various transformations, such as melting, dissolution etc., and result in condensed phases that do not always tend to the thermodynamic equilibrium (crystalline) state under ambient conditions, instead forming amorphous sub-cooled liquids.[15] In the atmosphere, such interactions between organic molecules that span a wide range of chemical functionalities may lead to particles that exhibit vapor pressures that are much lower than expected.[16] Deriving an improved understanding of how physical state and vapor pressure are connected will allow us to better predict the chemical evolution of complex systems.

Many studies have explored the vapor pressure, and specifically the vapor pressure of the diacids, using various laboratory techniques such as tandem differential mobility analysis,[17–20] Knudsen effusion mass spectrometry,[21] thermal desorption mass spectrometry,[22,23] and single particle methods, including optical tweezers and the electrodynamic balance (EDB).[12] There is over an order of magnitude variability in the reported vapor pressures, attributed both to the range of methods as well as the physical state the samples can adopt (see Soonsin et al.[24] and Bilde et al.[11] for a compilation of measured values). Although some of these previous studies identified and compared amorphous sub-cooled liquid and crystalline solid states, measurements were limited to below or slightly above ambient conditions (up to 303 K). While these are most relevant

for the atmosphere, they limit a more fundamental exploration of the role of temperature in regulating phase state and the associated vapor partitioning properties. Through measurements on crystal and amorphous states, and saturated solutions, it has been identified that odd-numbered carbon chains, in particular, can form anhydrous condensed phase states that exhibit thermodynamic properties consistent with either crystalline or amorphous behavior, with the former being the most thermodynamically stable state of the material.[12,15,17,18]

In this work, we explore the temperature dependence of the vapor pressure of a series of dicarboxylic acids, specifically addressing the high temperature behavior of these systems. As the temperature increases and the melting point is approached, it is expected that the thermodynamic behavior of the condensed phases, whether amorphous or crystalline, will converge. Here, we use single particles levitated in a linear-quadrupole electrodynamic balance (LQ-EDB) and measure the rate of evaporation under dry conditions using either the change in size or the change in relative mass. Using optical methods, we determine whether the particle is crystalline or amorphous and attribute measured properties with the phase state of the sample.

From these data we determine the enthalpy of vaporization and/or enthalpy of sublimation and compare our results with previously reported values. Our measurements extend the range of available vapor pressure data and bridge a dearth of measurements in the temperature range from 293 K to ~350 K for amorphous phase states. The reported values of amorphous state vapor pressures do not require corrections for the activity of the evaporating species in a saturated solution, as in the case with some previous work, as

measurements are conducted under dry conditions. Additionally, particles with both phase states were produced under identical experimental procedures. Thus, our work allows for direct comparisons between amorphous and solid phases under the same environmental conditions and experimental configuration.

5.2. Methods

5.2.1. Sample Preparation

The chemicals in this study were used without further purification. Aqueous solutions were prepared from a series of dicarboxylic acid compounds, including malonic acid (MA, Sigma-Aldrich, 99% purity), succinic acid (SA, Sigma-Aldrich, ≥ 97 % purity), glutaric acid (GA, Sigma-Aldrich, 99 % purity) and adipic acid (AA, Sigma-Aldrich, ≥ 99.5 % purity). Solutions were prepared at concentrations from 6 to 8 g/L, except for malonic acid which was prepared at a concentration of 20 g/L to generate larger particles due to an observed rapid initial evaporation period. The concentration dictates the size of the resulting particle and does not further impact measurements. For each solution, the compound was weighed and dissolved in HPLC grade water (Fisher Chemical) and stored in a pre-cleaned plastic vial. To generate samples for levitation, up to 12 μL of each solution was transferred into a microdroplet dispenser (Microfab MJ-ABP-01, 30 µm orifice) and droplets on the order of 50 μm in diameter were introduced into the LQ-EDB. Excess water evaporated and the particles attained an equilibrium (or metastable) state with respect to gas phase water.

5.2.2. Experimental Setup

The LQ-EDB used in this study was based on the configurations described in our previous work, with minor modifications to allow the temperature to be controlled above ambient conditions using heating cartridges.[25] A succinct summary of the operation is described here. Droplets were generated by the microdroplet dispenser in the presence of an induction electrode (130 to 500 V) creating a net charge of 10 to 100 fC on the resulting droplet as it entered the LQ-EDB.[26] A 532 nm laser (Thorlabs CPS532, 5 mW) was used to illuminate the droplets for visual verification as they enter the trap. The trap consists of 4 stainless steel rods in a quadrupole arrangement with paired out-of-phase AC voltages applied in a diagonal manner, generating an electric field that confines the droplet to the central axis. A disc electrode with an applied DC voltage of 30 to 300 V in the center of the LQ-EDB creates a repulsive electrostatic force that balances net forces on the droplet and maintains the droplet in a fixed vertical position throughout the experiment. A CMOS camera (Thorlabs CS165MU) was used to visualize the droplet and stabilize the position of the droplet by changing the DC voltage through a PID feedback loop using LabVIEW software. To monitor evaporation as a function of temperature, a temperature between 303 K and 353 K was set using a Digi-Sense PID temperature controller (TC5000) coupled with four 2” cartridge heaters (1/8” diameter, McMaster-Carr 8376T27) inserted symmetrically around the particle trapping location running through the walls of the chamber. The temperature was measured with a thermistor embedded in the chamber wall, which measures a slightly higher temperature than within the chamber. This discrepancy was accounted for in the calibration, as described later. The LQ-EDB was heated for 30

minutes for the lower temperatures (303 K to 323 K) and up to 1.5 hours for the higher temperatures (333 K to 353 K) to ensure thermal equilibrium throughout the chamber ahead of experiments. Experiments were carried out under dry conditions and performed over 100's to 1000's of seconds to ensure sufficient evaporation occurred to determine evaporation rates accurately.

5.2.3. Mie Resonance Spectroscopy

The LQ-EDB trap was coupled with a broadband red LED (Thorlabs M660L4) to measure the evolving properties (size and refractive index) of spherical particles using Mie resonance spectroscopy. Broadband light was focused onto the levitated particle in the LQ-EDB and the back-scattered light from the particle was collected and introduced to a spectrometer (Ocean Insight HR4000) with resolution of 0.47 nm. Particles that have a spherical morphology can act as an efficient optical cavity in which light of specific wavelengths can become resonant.[27] This gives rise to morphology dependent resonances (MDRs) across the illuminated range of the spectrum (640 to 680 nm) and appear in the measured spectra as sharp peaks in intensity. Spectra were collected at 1 Hz with an exposure time of 1 s and analyzed offline to determine the center wavelength of each peak. The wavelength positions were delivered to the MRFIT sizing algorithm of Preston and Reid,[28] embedded in a LabVIEW graphical user interface, and the radius and wavelength-dependent refractive index of the particle were determined through a least-squares minimization procedure in comparison to Mie theory predictions of peak positions.[28] To validate the obtained results, full Mie theory simulations were generated using the output size and RI using the code of Bohren and Huffman[29] and the resulting spectra were visually

compared against experimental spectra. Sizing results were validated by qualitative assessment of the comparisons between peak widths and positions in the measured and simulated spectra. Particles in this study ranged between 3 to 10 μm and this size range was chosen because the particles smaller than 3 μm lack sufficient spectral information to accurately determine the size, while particles larger than 10 μm exhibit complex spectra that can give rise to multiple low-error solutions, thus yielding imprecise results.

All particles in this study that remained spherical under the experimental conditions were analyzed using this method. However, due to the solid phase state adopted by some particles, not all samples remained spherical and lacked the spectral information required for sizing. For such cases, an electrostatic analysis was used to determine any changes in particle mass during evaporation.

5.2.4. Electrostatic Analysis

While generally superseded by more accurate optical methods, the electrostatic analysis of particles using an EDB to determine relative mass changes has been long established. In the absence of an air flow in the chamber, the only force acting on the particle is gravity, therefore the balancing voltage (DC) is directly proportional to the mass of the particle present, as shown in equation 1:[30]

$$mg = \frac{qV_{DC}C}{z} \tag{5.1}$$

where m is the mass of the particle, g is the acceleration due to gravity, q is the charge on the particle, V_{DC} is the balancing voltage, C is the geometrical constant that accounts for the effect of electrode geometry on the electric field, and z is vertical distance from the electrode to the particle. Both q and C are assumed to be constant for a particle at a fixed z

above the electrode, so the DC varies linearly with the particle mass. Therefore, tracking the changes in DC voltage yields an estimation of decrease in relative mass of the particle due to its evaporation, which was used to derive the vapor pressure along with an estimated starting size.

5.2.5. Evaporation Model

A steady-state isothermal evaporation model was used to relate the measured evaporation rate of diacid components to their vapor pressure. Continuum regime kinetics were applied due to the large size of the particle relative to the mean free path of the evaporating molecules, which gives a Knuden number of ~0.01.[31] For a general system containing multiple components with index *i*, the mass flux from a particle of radius *a* is related to the vapor pressure, $p_{i,a}$, through Equation 5.2:

$$\frac{dm_i}{dt} = \frac{4\pi a M_i D_i}{RT}\left(p_{i,\infty} - p_{i,a}\right) \tag{5.2}$$

where m_i is the mass of component *i* in the droplet, M_i is the molecular mass of *i*, D_i is the gas-phase diffusion coefficient, *R* is the gas constant, *T* is the temperature, $p_{i,\infty}$ is the environmental partial pressure of *i* , and $p_{i,a}$ is the partial pressure of *i* at the surface of the particle. For these single component diacids, $p_{i,\infty}$ is maintained at zero, and $p_{i,a}$ represents the pure component vapor pressure.

To derive the vapor pressure using Eq. 5.2, the density, gas-phase diffusion coefficient and molecular mass of the species of interest are needed. The diffusion coefficient values

as a function of temperature were derived for SA, GA, MA and AA using the Chapman-Enskog approach, as shown below in Equation 5.3:

$$D_i = 0.0018583\sqrt{T^3\left[\frac{1}{M_i}+\frac{1}{M_{N_2}}\right]}\frac{1}{P\sigma_{i,N_2}^2\Omega_{i,N_2}} \quad (5.3)$$

where M_i and M_{N_2} are the molecular masses of component *i* and N_2 respectively, *P* is the gas pressure in atm, σ_{i,N_2} is the binary collision diameter, with $\sigma_{i,N_2} = \frac{1}{2}(\sigma_i + \sigma_{N_2})$, and Ω_{i,N_2} is the collision integral which was determined using the tabulated values presented by Bird et al.[32] and the parameterization of Neufeld et al.[33] The values necessary for performing these calculations are provided in Table 5.1.

Table 5.1. Values for the collision diameter (σ**)** and collision integral (Ω) used to calculate the diffusion coefficient (D_i) for all compounds (MA, SA, GA, AA). See references in main text

Compound, *i*	**M_i / g mol^{-1}**	**σ_i / Å**	**$\Omega_{i,N2}$ (298K)**	**$\sigma_{i,N2}$ / Å**	**D_i x 10^{-6} / m^2 s^{-1} (298K)**
Nitrogen	28.00	3.798		3.798	
Malonic Acid	104.06	5.33	1.400	4.564	6.8039
Succinic Acid	118.09	5.69	1.400	4.744	6.0449
Glutaric Acid	132.12	6.01	1.440	4.904	5.8637
Adipic Acid	146.14	6.30	1.375	5.049	5.3872

This approach is generally considered to yield gas phase diffusion values that are accurate to within 5%, although some discrepancies up to 13% have been observed,[34] and allows the temperature dependence to be determined.

If the absolute size of the particle is known, as with measurements on spherical particles, and $p_{i,\infty} = 0$, Equation 5.2 may be re-written as:

$$\frac{da^2}{dt} = \frac{-2M_i D_i p_{i,a}}{\rho RT} \tag{5.4}$$

where ρ is the density of the particle. This may be rearranged to solve for $p_{i,a}$ from the measured rate of change of the radius-squared with time. For measurements where the radius was not directly measured, as in the case of non-spherical solid particles, an estimate of the initial radius was required and a subsequent numerical simulation of the evolving mass using Equation 5.2 was performed. The model generates an output of mass versus time, which was normalized to the starting value and compared against the experimental normalized V_{DC} data. The value of $p_{i,a}$ was varied in order to achieve agreement between the measured and modelled evaporation trends.

5.3. Results and Discussion

5.3.1. In-Situ Temperature Calibration

To characterize vapor pressures as a function of temperature, a reliable measurement of temperature was required. A thermocouple in the aluminum chamber wall of the LQ-EDB was used to control the heater output, but the exact temperature experienced by a levitated particle is lower than in the walls due to the low thermal conductivity of air in the chamber. In this work, we used the evaporation rate of a well-characterized chemical compound

(glycerol) to solve equation 5.2 for T, with a known value of $p_{i,a}$. The temperature dependent vapor pressure of glycerol was determined from an empirical expression:

$$\ln\left(p_{i,a} \,/\, kPa\right) = A \times \ln(T) + \frac{B}{T} + C + D \times T^2 \tag{5.5}$$

with coefficients $A = -2.12586 \times 10^1$, $B = 1.67263 \times 10^4$, $C = 1.65510 \times 10^2$ and $D = 1.10048 \times 10^{-5}$ taken from the CHERIC database. In previous measurements at room temperature, this relation has been shown to be accurate.[35]

Measurements were made on the size-evolution of glycerol particles trapped at a range of temperatures, from 293 to 333 K, and the evaporation rate of the particle was determined under dry conditions to avoid the complicating effects of water uptake. Figure 5.1A shows the radius evolution of three particles at three different temperatures. To compare the influence of temperature alone on the evaporation rate, the size must be factored out. When integrating Equation 5.4, one arrives at the expression:

$$a^2 = kt + a_0^2 \tag{5.6}$$

where a_0 is the starting size and *k* is the evaporation rate given by:

$$k = \frac{-2M_i D_i p_{i,a}}{\rho RT} \tag{5.7}$$

We can rearrange Equation 5.6 to:

$$\frac{a^2}{a_0^2} = \frac{k}{a_0^2} t + 1 \tag{5.8}$$

and, thus, a plot of $\frac{a^2}{a_0^2}$ versus $\frac{t}{a_0^2}$ will yield a straight line that depends only on *k*. Figure 5.1B shows this relationship and leads to straight line plots that vary only due to the temperature, giving a clear indication of the influence of temperature on the evaporation rate.

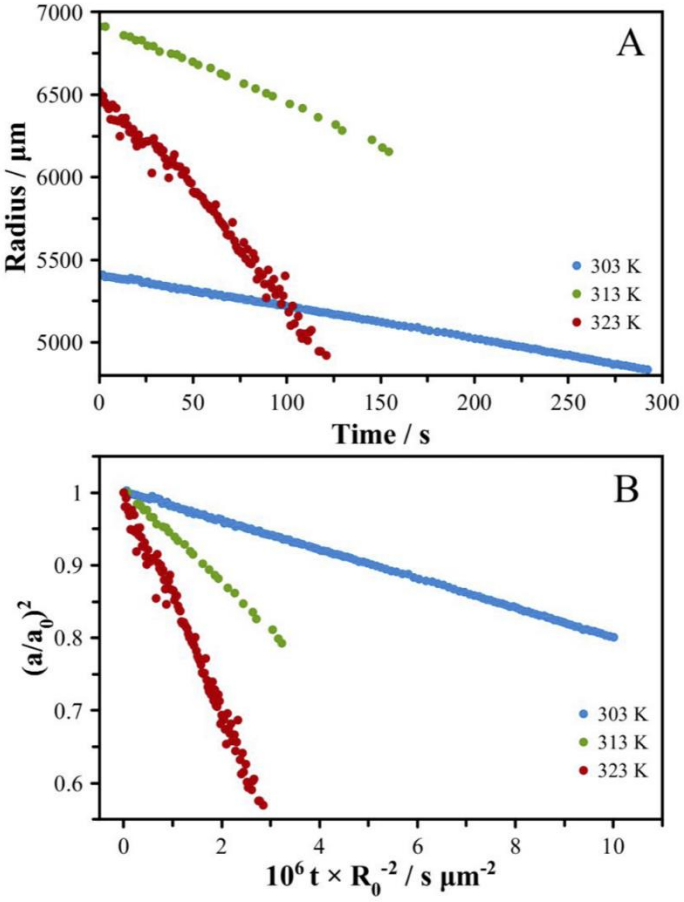

Figure 5.1: (A) Radius evolution of glycerol particles evaporating at temperatures from 303 – 323 K. (B) Temperature dependence on evaporation rate with the influence of size omitted.

From these data and the parameterized vapor pressure (Equation 5.5), the temperature was determined by solving Equation 5.4 and yielded a linear dependence of the calculated temperature as a function of the set-point temperature (Figure 5.1A). The uncertainty in the calculated T of ± 1 K is determined from a $\pm 10\%$ uncertainty in the value of D_i (for glycerol) and does not consider any uncertainty in the values of $p_{i,a}$. Figure 5.2A shows good agreement between the set and calculated temperature of the trap, with a small negative deviation of the trap temperature form the set temperature, as expected based on thermal conductivity and heat loss to the environment. A comparison of the vapor pressure

derived using the evolving mass of the particle in an electrostatic analysis yielded values that agreed within 10%.

Further temperature calibration to higher temperatures was not possible using glycerol due to the rapid rate of evaporation and the inability for the MDR's to be resolved due to the rapid change in particle size. Instead, measurements were performed on another semi-volatile organic molecule, 1,2,6-hexanetriol, at up to 347 K, with a vapor pressure $50\times$ lower than glycerol at room temperature. This system was chosen as there are literature sources against which the results can be compared. The vapor pressure measured as a function of temperature is shown in Figure 5.2B. These data agree well with the low temperature measurements of Logozzo and Preston,[36] and yield an estimate for the enthalpy of vaporization to be $\Delta H^{\circ} = 129 \pm 3$ kJ / mol. Compared to the value obtained from the Logozzo and Preston data of 144 kJ / mol (note the value reported in the original manuscript was incorrectly stated to be 154 kJ /mol), it is clear that measurements over a large range of temperatures are required for accurately constraining the enthalpy. When combining both datasets, we arrive at a value of 130 ± 2 kJ /mol. Note that the uncertainty quoted reflects an error in the linear fit and does not account for systematic errors in any parameters.

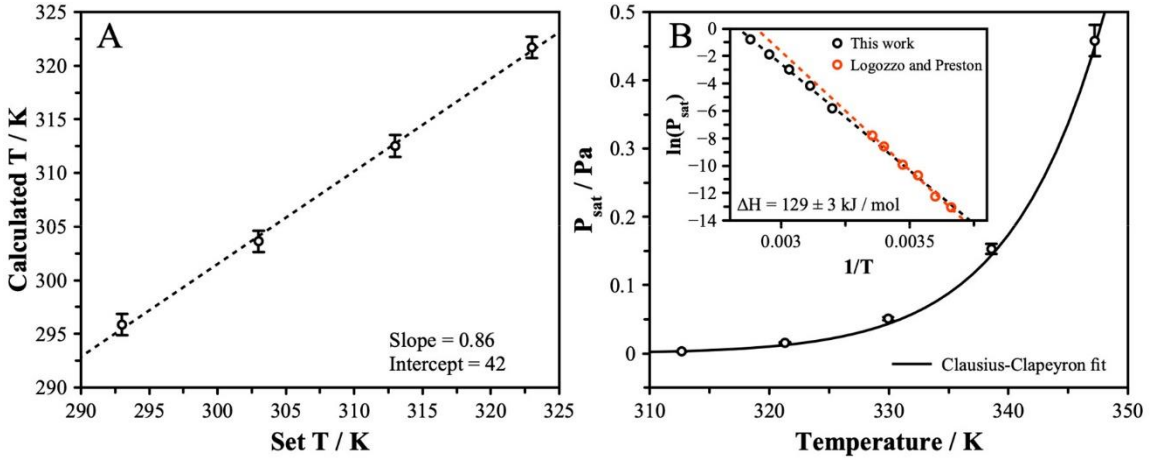

Figure 5.2: (A) The evaporation of a glycerol particle was used to derive the temperature in the LQ-EDB. Determination of the actual temperature inside the LQ-EDB using the linear relationship between calculated and set temperature. (B) The vapor pressure trend of 1,2,6-hexanetriol is shown as a function of temperature for our data and that of Logozzo and Preston.[36] Figure inset shows the calculated value for the enthalpy of vaporization of 1,2,6-hexanetriol using the linear slope of $\log_e(P_{sat})$ versus 1/T for our data. See text for a discussion of the connection with the data reported by Logozzo and Preston.[36]

5.3.2. Morphology of Diacid Particles Under Dry Conditions

The vapor pressures of all four diacids were determined by conducting evaporation measurements at temperatures varying from 303 to 353 K in increments of 10 K. The odd/even alteration in carbon number of these diacids influence their morphologies, and dry particles exist as either amorphous sub-cooled liquid or crystalline solid particles. Adipic acid ($n_C = 6$) and succinic acid ($n_C = 4$) samples were both observed to consistently form a solid, non-spherical particle morphology under dry conditions, indicating these systems effloresced to a crystalline solid state. Glutaric acid and malonic acid were observed to randomly form either solid, non-spherical particles or spherical, amorphous sub-cooled liquid particles following trapping. The morphology affects the rate of evaporation resulting in differences in their vapor pressures corresponding to the different enthalpies of the subcooled and crystalline states. In all cases, the amorphous subcooled

liquids showed larger vapor pressures than their crystalline counterparts. A summary of the morphologies adopted by particles across a range of temperatures is shown in Table 5.2.

Table 5.2. Summary of particle morphology at each temperature for each diacid. 'C' represents crystalline morphology whereas 'A' represents amorphous morphology. Note that Mie resonance sizing was performed for only amorphous particles, whereas electrostatic analysis was performed for both amorphous and crystalline particles.

Diacid	**Carbon #**	**Temperature / K**					
		303	313	323	333	343	353
Malonic Acid (MA)	3	C / A	C / A	A	A	A	A
Succinic Acid (SA)	4	C	C	C	C	C	C
Glutaric Acid (GA)	5	C / A	C / A	C / A	C / A	C / A	C / A
Adipic Acid (AA)	6	C	C	C	C	C	C

Although various factors were explored to explain the formation of crystalline versus amorphous states in these particles, no consistent explanation was determined. Instead, the process is likely stochastic in nature, with molecular diffusion playing a determining role in whether the particle achieves a thermodynamic equilibrium state. We discuss the results and dynamics of each diacid in the following sections.

5.3.3. Succinic Acid

Succinic acid particles were observed to form a solid crystalline phase on drying, indicated by the complete loss of structure in the broadband light scattering spectra. The temperature dependence on the evaporation rates of SA particles was investigated across 303 to 353 K and the vapor pressures were determined at these temperatures. Due to the crystalline state, the electrostatic method was used to derive vapor pressures, with the size estimated by the starting solution concentration. The vapor pressure increases with temperature, as depicted in Figure 5.3A, where each open circle is the average of at least three evaporation

measurements performed at a specific temperature, with error bars depicting the standard deviation in derived vapor pressure. The origin of the ~10% uncertainty comes from environmental factors in the trap, such as small changes in RH and temperature that affect the conditions experienced by the particle, and particle shape effects. The surface area to volume ratio determines the rate of evaporation and it is assumed in the analysis of these measurements that the particle adopts a spherical morphology. Because it is not the case, there is an absolute uncertainty based on the shape factor and a random error that arises from the different shape factors arising due to the morphology adopted by the particle.

The calculated vapor pressure ranged from 8.9×10^{-5} to 3.7×10^{-2} Pa from 303 to 353 K, respectively. Literature data of the vapor pressure at 298 K report values in the range 3.9×10^{-5} to 1.5×10^{-3} Pa, compared to our extrapolated value of 2.2×10^{-5} Pa.[20,22,37,38] The vapor pressure at 298 K in this study shows agreement within the range of literature values. In their compilation of data at 298 K, Bilde et al.[11] find a best value of $7.7^{+5}_{-3} \times 10^{-5}$ Pa for the solid-state vapor pressure, which is higher than our value. However, the spread in values for this system are large and our measurements fall within the reported ranges. Indeed, Soonsin et al.[15] showed that the evaporation of SA particles shows two vapor pressures indicating two possible crystal arrangements. The first of which contained enclosed water and amorphous portions, while the second arrangement was due to the loss of enclosed water and the further crystallization of the amorphous portions.[11,15]

The temperature dependence of the vapor pressure allows us to establish a value for the enthalpy of sublimation of succinic acid. Using the Clausius-Clapeyron equation in conjunction with experimental vapor pressures, the enthalpy of sublimation was found to

be 134 $\pm$ 9 kJ/mol, as shown in Figure 5.3A, which is comparable to the value reported by Cappa et al.[22] of 128 kJ/mol but is lower than the literature average reported by Bilde et al. of 115$\pm$15 kJ/mol.[11]

5.3.4. Adipic Acid

Adipic acid follows a similar trend to succinic acid as the next even-number diacid in the homologous series. Again, due to its crystalline morphology we used the electrostatic analysis approach to determine vapor pressure and measured vapor pressures in the range of 4.50 x 10^{-5} Pa to 2.8 x 10^{-2} Pa for 303 to 353 K, respectively. In this system, low temperature measurements deviate to slightly higher vapor pressures than expected based on a linear fit of $\log_e(P_{sat})$ versus inverse temperature, as dictated by the Clausius-Clapeyron relation. Higher temperature measurements were closer to the expected trend and are discussed here.

The temperature dependence of vapor pressure of AA, as depicted in Figure 5.3B, shows a similar trend to SA, but is comparatively lower due to the differences in molecular structure and weight. Literature vapor pressures are found in the wide range of 6.0 x 10^{-6} Pa to 2.8 x 10^{-4} at a temperature of 298 K.[21,37] Extrapolating our data to this temperature using the Clausius-Clapeyron equation yields an estimated value of 1.4 x 10^{-5} Pa which is within the literature value range and agrees well with the best estimate compiled by Bilde et al. of $1.9^{+1.4}_{-0.8}$ x 10^{-5} Pa.[11] Direct measurements under room temperature conditions are challenging due to the very slow change in the particle size and the relatively low precision of the electrostatic measurements compared to optical measurements of size. The enthalpy

of sublimation for AA was determined to be 129 ± 9 kJ / mol, falling lower than the values reported by Cappa et al.[22] but within the range of values reported by Bilde et al.[11]

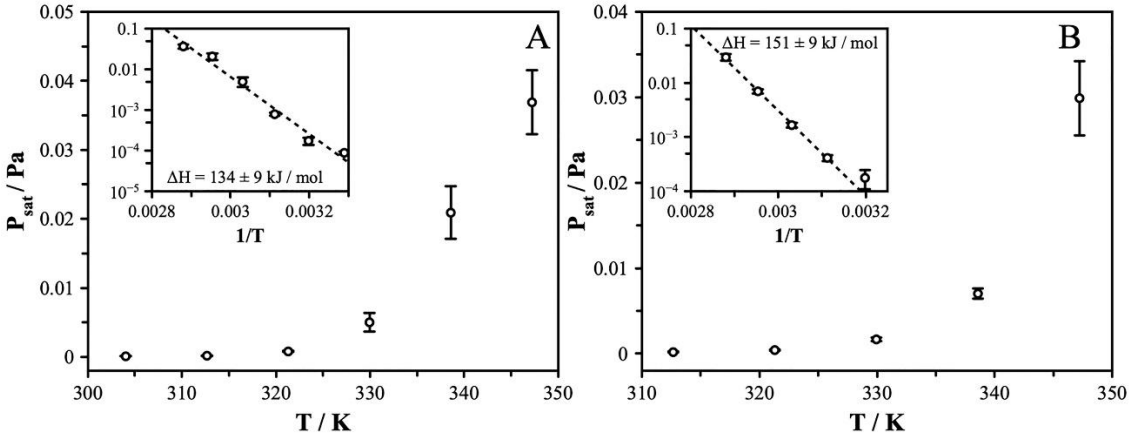

Figure 5.3: The experimentally determined vapor pressure as a function of temperature for: (A) Succinic acid, and (B) Adipic acid. Inset figures show Clausius-Clapeyron plots (note that the y-axis is represented with $\log_{10}$ rather than $\log_e$) along with the enthalpy of sublimation derived from the linear slope of $\log_e(P_{sat})$ and 1/T. Error bars represent the standard deviation in the vapor pressure values for repeat measurement at each temperature.

5.3.5. Glutaric Acid

Glutaric acid particles were encountered in both spherical amorphous states and non-spherical crystalline states across all temperatures. It is not clear what factors control the final morphology of these particles. Slow drying by controlling the RH, temperature changes, and particle size were not found to strongly impact the formation of one phase over another. At high temperatures (333 K to 343 K), amorphous particles were consistently observed, perhaps due to the system being closer to the melting temperature or experiencing more rapid drying. To generate non-spherical crystalline particles to probe under these conditions, particles were trapped at lower temperatures, where non-spherical particle formation was more typically observed. A general observation pointed to freshly made glutaric acid stock solutions producing non-spherical particles, while older solutions

produced more spherical particles. This was a purely empirical observation, and we have no explanation for its origin. No changes in the solution were expected and no exposure to light or ambient gas phase reactants was possible that might cause chemical changes. One hypothesis, unsubstantiated by literature or experiment, points to dimers or small clusters remaining stable in solution for extended times that can nucleate a crystal phase. These clusters breakdown over time as they become fully solubilized. This explanation requires a very slow kinetic process to drive changes in the solution over time and efforts to test this theory by sonicating and heating the solution did not yield any differences in behavior. At this point, we conclude that formation of a solid crystalline phase is a stochastic process and may involve multiple steps due to the formation of polymorphs in glutaric acid resulting in a highly non-linear dependence of particle phase on many different properties and processes. For the purposes of this work, we accept that samples were generated with either crystalline or amorphous character and analyze the behavior of these systems accordingly.

A direct comparison of the slope of the DC voltage of a spherical versus a non-spherical particle is shown in Figure 5.4 showing that the spherical particles evaporate considerably faster. The particles are easily segregated into spherical and non-spherical by comparing the Mie resonance spectra, clearly showing the different morphologies, as seen in Figure 5.5.

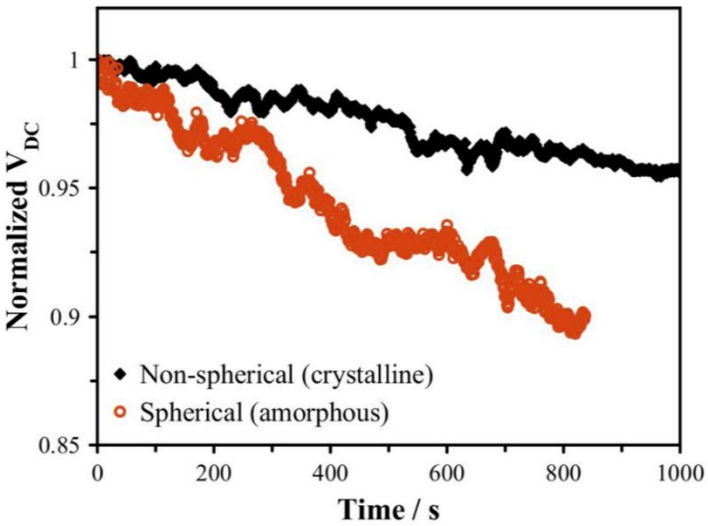

Figure 5.4: Comparison of the normalized DC voltage from a non-spherical (black) and spherical (red) glutaric acid particle. Over the same period, spherical particles evaporate much quicker than their non-spherical counterpart.

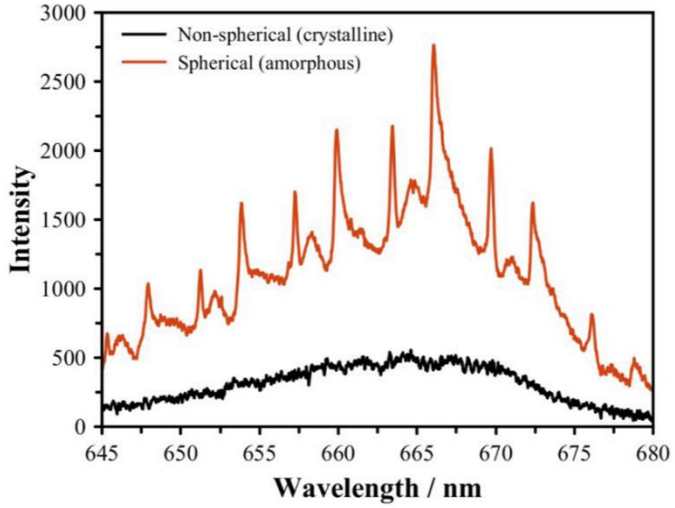

Figure 5.5: Comparison of Mie resonance spectra for a non-spherical (back) and spherical (red) glutaric acid particle. Absence of Mie resonance peaks indicates a non-spherical particle.

In the case of the non-spherical particles, the electrostatic analysis method was applied to determine the vapor pressure as a function of temperature, shown in Figure 5.6A. At 298K, the value we determine was 4.4 x 10^{-5} Pa, which is on the low end of the literature data compiled and reported by Bilde et al.,[11] with a literature average value for the crystal state

to be $1.7^{+1.5}_{-0.8}$ x 10^{-4} Pa (Figure 5.6B). From a Clausius-Clapeyron analysis, the enthalpy of sublimation was determined to be 154±9 kJ / mol. This is higher than many literature values and the vapor pressure values measured here were considerably lower, indicating that a more stable state was measured in these experiments. As reported by Yeung et al.,[39] GA has two crystalline forms with different thermal stabilities. At lower temperatures the β-form is stable while the α-form is found to be stable at higher temperatures. The energy difference between the crystal polymorphs is on the order of 2 kJ / mol and it is not possible to distinguish the difference based on the enthalpy of sublimation alone.[40]

For spherical particles, the size evolution was analyzed using Mie theory, and yielded vapor pressures that were considerably higher. These are shown in Figure 5.6A and reveal values that are around 5× higher than the solid particles. At 298K, the vapor pressure is estimated to be 4.6 × 10^{-4} Pa, which is lower than the value reported by Bilde et al. of $1.0^{+0.3}_{-0.2} \times 10^{-3}$Pa but falls within the broad range of values in the literature.[11] The enthalpy of vaporization here was found to be 129 ± 6 kJ / mol, in agreement with literature values, but falling above the literature average compiled by Bilde et al.[11,20,22,37,38] The difference in the enthalpy between our measured solid and subcooled states is on the same order as values for the enthalpy of fusion of glutaric acid, indicating that the amorphous phase is consistent with the sub-cooled liquid.[40]

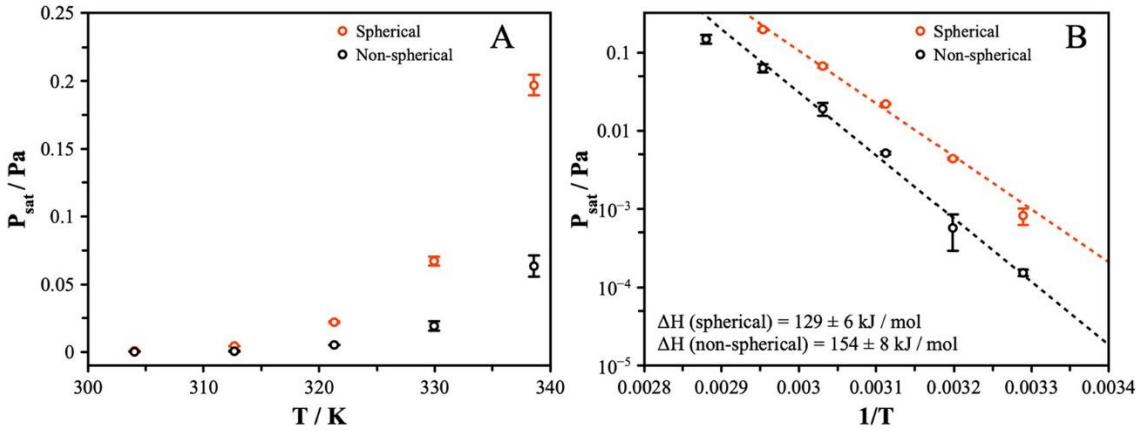

Figure 5.6: (A) Comparison between the derived vapor pressures for both spherical (red) and non-spherical (black) glutaric acid particles. The non-spherical vapor pressures were consistently lower than the spherical particle vapor pressures across all temperatures due to the differences in morphology. (B) The enthalpy of sublimation for both spherical and non-spherical morphologies of glutaric acid was calculated using the linear relationship between $\log_e P_{sat}$ and 1/T. Again, non-spherical enthalpies were lower at each temperature compared to spherical particles and error bars represent their respective standard deviation in the vapor pressure values for different measurement trials at each temperature.

5.3.6. Malonic Acid

Malonic acid, like glutaric acid, is an odd-numbered dicarboxylic acid and showed both amorphous and crystalline character. The crystalline phase was only observed at 303 and 313 K, and vapor pressures at these temperatures were determined using electrostatic analysis to be on the order of 5.5×10^{-5} and 2.3×10^{-4} Pa, respectively. A full Clausius-Clapeyron analysis was not performed due to the limited data available as a function of temperature. As with the case of glutaric acid, the vapor pressures for the crystalline particles were around an order of magnitude lower than the amorphous particles. For MA, the evaporation of amorphous particles presented some interesting observations. Figure 5.7 shows the radius evolution of a single particle held at 333 K. It is clear from this plot that there are multiple distinct slopes in the data, indicating possible phase transitions that lead to reduced vapor pressure and evaporation rate. This change in slope was observed from the radius data, derived from spectroscopy, and the electrostatic data. At this temperature,

three slopes were identified, however the data begins to break down, as seen in Figure 5.7. This was due to a degradation of the spectra and the small absolute size of the particle. To confirm the purity of the compound, the composition of the starting solution was probed using electrospray ionization mass spectrometry (Q Exactive Focus Orbitrap MS) in both positive and negative ionization modes. A prominent peak was observed at m/z consistent with the singly deprotonated parent compound, and lack of any significant peaks above the background confirms that sample was not measurably contaminated.

During the evaporation, the refractive index was observed to change in conjunction with the size. The RI depends on many factors, such as composition, density, and temperature. Given that the composition was pure, and the temperature was constant, the change in RI may indicate a change in the particle phase to one with a higher density. It should be noted, however, that there is a larger uncertainty in the RI than the radius, and this is apparent as the scatter in the RI increases significantly.

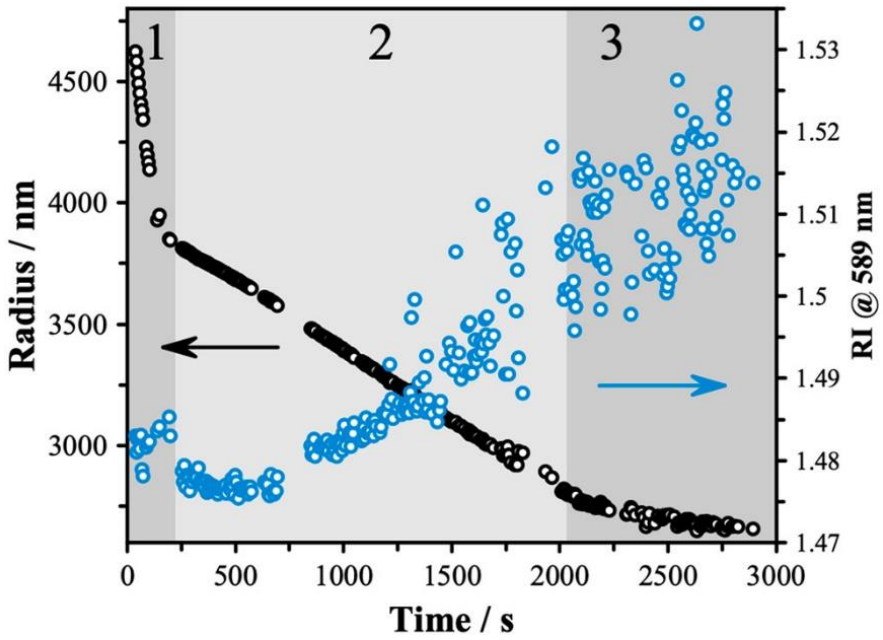

Figure 5.7: The evaporation of malonic acid over 3000s showed an evolution in both the radius and refractive index (RI). Three distinct slopes were observed which are marked by the shaded region. This also corresponds to a simultaneous increase in RI over the course of the measurement.

An analysis of the two slopes (1 and 2, indicated in Figure 5.7) and the resulting estimates of vapor pressure from each is shown in Figure 5.8A and 5.8B. Extrapolating to 298 K, the vapor pressures predicted from slope 1 and slope 2, respectively, are 0.004 and 1.3 x 10^{-4}. Data from slope 1 indicate a higher vapor pressure than the sub-cooled value compiled by Bilde et al.[11] ($6.2^{+3.2}_{-2.1} \times 10^{-4}$ Pa) that were extrapolated from measurements on aqueous solutions, while much close agreement is observed for slope 2 when compared against the reported solid vapor pressure ($1.7^{+1.1}_{-0.7} \times 10^{-4}$ Pa). Both slopes show a temperature dependence as expected from the Clausius-Clapeyron equation, with a ~20 kJ /mol difference in the estimated enthalpy of vaporization (104 ± 5 kJ /mol versus 124±5 kJ /mol for amorphous sub-cooled and solid-state crystal phases, respectively). This change in enthalpy is around the difference observed between amorphous and crystalline glutaric

acid, but falls slightly lower than literature data for the enthalpy of fusion (of 23 kJ / mol).[41] This indicates that over the course of measurement, the sample may be undergoing a phase transition. Indeed, the Mie spectra show clear peaks initially, indicating that the particle remains spherical. Over time, during slope 2, the peaks in the spectra become less well resolved, as evidenced by the degradation of the spectra resulting in increased scatter in the radius and RI output, indicating that the particle tends towards a non-spherical morphology. The values of vapor pressure for slope 2 are slightly higher than the values reported on particles that were crystalline from the start of the measurement, indicating the particle may be a mix of crystalline and amorphous during this regime. Slope 3 in Figure 5.7 was only observed in limited cases, and due to the small size of the particle at this point, the estimated vapor pressure using these data is not reliable, falling significantly below the other data. However, it is likely that this represents the fully crystalline state with the amorphous contribution having been eliminated.

Several factors may be contributing to these observations. The existence of many malonic acid polymorphs likely gives rise to the transitions between phases during the measurement.[42] While the stability and thermodynamics of up to five polymorphs have been explored in the solid state, it is not known what forms will be available to levitated particles prepared following rapid drying from aqueous solution droplets, as is the case here. Additionally, malonic acid can undergo a keto-enol tautomerization in aqueous solution. Recent work indicates this is accelerated in droplets; however, the timescales are still on the order of hundreds to thousands of seconds, with the rate slowing at lower RH.[43] Given our droplets experience rapid drying immediately after generation, it is likely that

the keto-enol ratio will be dictated by the conditions in the dilute starting solution. The equilibrium constant strongly favors the keto-form and, thus, we assume that our sample particles are primarily consisting of this tautomer.[44]

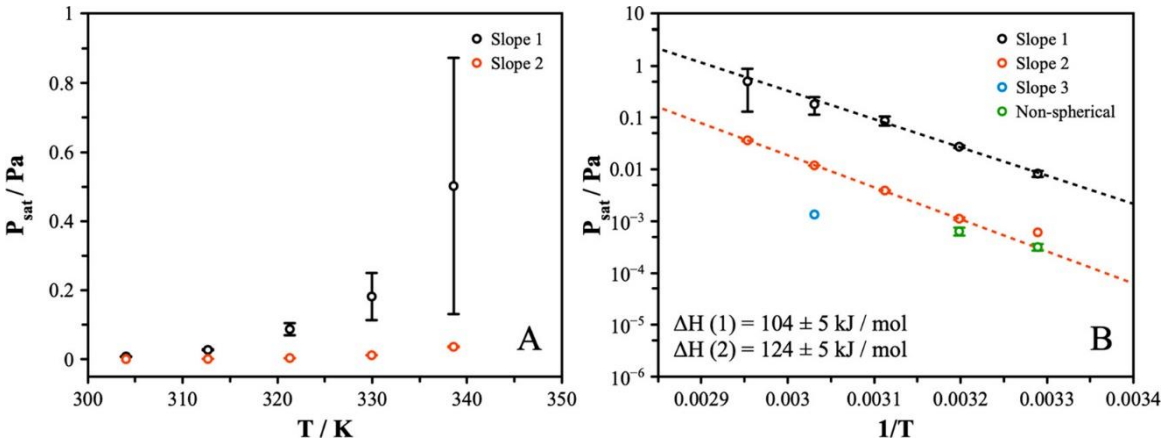

Figure 5.8: (A) A comparison of the derived vapor pressure for the first (black) and second (red) slopes observed during the evaporation of MA. The second slope vapor pressure is lower than the first slope due to their difference in evaporation rate. (B) Relationship between $\log_e(P_{sat})$ and 1/T for four different phases attributed to three distinct MA polymorphs (black, red, and blue) and the MA solid phase (green). The corresponding enthalpy of vaporization was derived for both slopes 1 and 2 using the method previously discussed.

Table 5.3. Summary of all data corresponding to the measurements and relevant literature. Literature values were obtained from Bilde et al.[11] from their comprehensive analysis and averaging of the literature data. We refer readers to the reference contained therein for original sources.

Species	P_{sat} (298 K) / Pa	ΔH / kJ mol^{-1}	P_{sat} (298 K) / Pa Lit.	ΔH / kJ mol^{-1} Lit.
Malonic acid (amorphous)	$4.0\pm0.4 \times 10^{-3}$	104 ± 5	$6.2^{+3.2}_{-2.1} \times 10^{-4}$	115 ± 22
Malonic acid (crystalline)	$1.3\pm0.2 \times 10^{-4}$	124 ± 5	$1.7^{+1.1}_{-0.7} \times 10^{-4}$	111 ± 15
Succinic acid	$2.2\pm0.2 \times 10^{-5}$	134 ± 9	$7.7^{+5}_{-3} \times 10^{-5}$	115 ± 15
Glutaric acid (amorphous)	$4.6\pm0.3 \times 10^{-4}$	129 ± 6	$1.0^{+0.3}_{-0.2} \times 10^{-3}$	100 ± 5
Glutaric acid (crystalline)	$4.4\pm0.4 \times 10^{-5}$	154 ± 8	$1.7^{+1.5}_{-0.8} \times 10^{-4}$	130 ± 11
Adipic acid	$1.4\pm0.1 \times 10^{-5}$	129 ± 9	$1.9^{+1.4}_{-0.8} \times 10^{-5}$	131 ± 18

5.4. Conclusions

We report measurements on the rate of evaporation of particles levitated in a linear quadrupole electrodynamic balance at elevated temperatures and derive the vapor pressure of pure component dicarboxylic acids. Through analysis of the physical state adopted by the particles in our measurements, we explore the connection between the vapor pressure and the formation of amorphous or crystalline phase states. We have reported vapor pressure measurements for dicarboxylic acid molecules across a range of temperatures previously unexplored in the literature for levitated particles. To aid comparisons, we have reproduced our values for the vapor pressure at 298 K and enthalpies, along with literature data, in Table 5.3. The literature data, taken from the meta-analysis of Bilde et al.[11], represent averages of many experimental datasets spanning a varied range of temperatures and, while some of our data falls outside the compiled averages, the same trends are observed with respect to the influence of phase, molecular size and temperature. As expected, an odd/even alteration in physical state was observed with changing number of carbon atoms. Even-number molecules, which are known to exhibit lower solubility, were observed to form the crystalline phase under all conditions, as evidenced by the loss of spectral features in the Mie resonance spectra. Odd-numbered molecules were observed to randomly form either the crystalline phase or an amorphous sub-cooled liquid phase. While it was not possible to control the phase state adopted by the particle, unambiguous identification of the phase state was inferred from the persistence of resonance peaks in the spectra (amorphous) or the loss of structure features typical of crystallization (solid). These measurements allow for a direct comparison of the effect of phase state using particles

generated and manipulated in the same experimental procedures. Consistent with previous studies that compile measurements from multiple techniques to achieve a comparison between amorphous and solid phase states, we show that crystal phase state vapor pressures are on the order of 4× to 10× lower than their amorphous counterparts. These measurements also allowed both the enthalpy of vaporization and sublimation for the compounds of interest to be determined, with values generally consistent with previous estimates derived from low temperature measurements. The differences observed between the crystalline and sub-cooled liquid states were consistent with the enthalpy of fusion, validating assertions of the ascribed phase state. In the case of malonic acid, abrupt changes in the evaporation rate were observed, indicating a change of phase over the course of the measurement. This was not observed in glutaric acid and may be attributed to the greater mobility of malonic acid molecules due to the smaller size.

Compared to the extensive previous literature exploring these systems, summarized in the previously cited review by Bilde et al.,[11] this work provides evidence that the amorphous phase states of these compounds, previously shown only at room temperature and below, persist at elevated temperatures up the maximum accessible temperature of our methods. While a convergence of the phase state is expected as the melting point is approached, the persistence of amorphous phases at high temperature provides an opportunity to measure vapor pressure across a broad range of temperatures. This allows for improved estimates of the vapor pressure at low temperatures relevant to the atmosphere, as discussed in the following section.

5.4.1. Atmospheric Relevance

Although these measurements were performed for samples at elevated temperatures, the thermodynamic data are well described using a simple Clausius-Clapeyron equation. This allows vapor pressure to be estimated at low temperatures through a linear extrapolation of $\log_e(P_{sat})$ versus inverse temperature. We have demonstrated several important factors in this work that will inform future studies on the vapor pressure and volatility of atmospheric samples. Firstly, at least in the cases explored here, amorphous sub-cooled liquid phases persist even at elevated temperatures, indicating that volatility basis sets derived from thermal desorption methods for SOA samples should yield similar results to isothermal measurements.[45] Secondly, using isothermal measurements above ambient temperatures, we can establish and estimate vapor pressure for low volatility species that would otherwise evaporate too slowly under ambient conditions. This allows a methodology for establishing vapor pressures and volatilities for low and extremely low volatility organic compounds.

However, given the chemical complexity of atmospheric aerosol particles, it is unclear how informative any pure component measurements are for estimating the vapor pressure of individual component in mixtures. When the phase state is taken as an additional complicating factor, single valued vapor pressures are not sufficient to fully describe the behavior of these systems. Furthermore, the phase states adopted by particles containing mixtures of odd and even numbered acids is unknown, and the thermodynamics that describe volatilization of species in complex atmospheric particles is even less well-constrained. In future work, we will couple the high temperature LQ-EDB to a high-resolution mass spectrometer, to perform a compositional analysis of complex mixtures as

they undergo evaporation.[46–48] This will facilitate a molecularly-resolved understanding of the chemical evolution and connect the findings to the physical and thermodynamic properties of complex organic mixtures.

5.5. References

(1) Hallquist, M.; Wenger, J. C.; Baltensperger, U.; Rudich, Y.; Simpson, D.; Claeys, M.; Dommen, J.; Donahue, N. M.; George, C.; Goldstein, A. H.; Hamilton, J. F.; Herrmann, H.; Hoffmann, T.; Iinuma, Y.; Jang, M.; Jenkin, M. E.; Jimenez, J. L.; Kiendler-Scharr, A.; Maenhaut, W.; McFiggans, G.; Mentel, T. F.; Monod, A.; Prévôt, A. S. H.; Seinfeld, J. H.; Surratt, J. D.; Szmigielski, R.; Wildt, J. The Formation, Properties and Impact of Secondary Organic Aerosol: Current and Emerging Issues. *Atmospheric Chem. Phys.* **2009**, *9* (14), 5155–5236. https://doi.org/10.5194/acp-9-5155-2009.

(2) Bilde, M.; Pandis, S. N. Evaporation Rates and Vapor Pressures of Individual Aerosol Species Formed in the Atmospheric Oxidation of α- and β-Pinene. *Environ. Sci. Technol.* **2001**, *35* (16), 3344–3349. https://doi.org/10.1021/es001946b.

(3) D'Ambro, E. L.; Schobesberger, S.; Zaveri, R. A.; Shilling, J. E.; Lee, B. H.; Lopez-Hilfiker, F. D.; Mohr, C.; Thornton, J. A. Isothermal Evaporation of α-Pinene Ozonolysis SOA: Volatility, Phase State, and Oligomeric Composition. *ACS Earth Space Chem.* **2018**, *2* (10), 1058–1067. https://doi.org/10.1021/acsearthspacechem.8b00084.

(4) Donahue, N. M.; Robinson, A. L.; Trump, E. R.; Riipinen, I.; Kroll, J. H. Volatility and Aging of Atmospheric Organic Aerosol. In *Atmospheric and Aerosol Chemistry*; McNeill, V. F., Ariya, P. A., Eds.; Topics in Current Chemistry; Springer: Berlin, Heidelberg, 2014; pp 97–143. https://doi.org/10.1007/128_2012_355.

(5) McDonald, B. C.; de Gouw, J. A.; Gilman, J. B.; Jathar, S. H.; Akherati, A.; Cappa, C. D.; Jimenez, J. L.; Lee-Taylor, J.; Hayes, P. L.; McKeen, S. A.; Cui, Y. Y.; Kim, S.-W.; Gentner, D. R.; Isaacman-VanWertz, G.; Goldstein, A. H.; Harley, R. A.; Frost, G. J.; Roberts, J. M.; Ryerson, T. B.; Trainer, M. Volatile Chemical Products Emerging as Largest Petrochemical Source of Urban Organic Emissions. *Science* **2018**, *359* (6377), 760–764. https://doi.org/10.1126/science.aaq0524.

(6) Qin, M.; Murphy, B. N.; Isaacs, K. K.; McDonald, B. C.; Lu, Q.; McKeen, S. A.; Koval, L.; Robinson, A. L.; Efstathiou, C.; Allen, C.; Pye, H. O. T. Criteria Pollutant Impacts of Volatile Chemical Products Informed by Near-Field Modelling. *Nat. Sustain.* **2021**, *4* (2), 129–137. https://doi.org/10.1038/s41893-020-00614-1.

(7) Yilmaz, E.; Tian, T.; Wong, V. W.; Heywood, J. B. An Experimental and Theoretical Study of the Contribution of Oil Evaporation to Oil Consumption; 2002; pp 2002-01–2684. https://doi.org/10.4271/2002-01-2684.

(8) Gough, M. A.; Rowland, S. J. Characterization of Unresolved Complex Mixtures of Hydrocarbons in Petroleum. *Nature* **1990**, *344* (6267), 344648a0. https://doi.org/10.1038/344648a0.

(9) Gough, M.; Rowland, S. Characterization of Unresolved Complex Mixtures of Hydrocarbons from Lubricating Oil Feedstocks. *Energy Fuels* **1991**, *5* (6), 869–874. https://doi.org/10.1021/ef00030a016.

(10) Ravikumar, V.; Senthilkumar, D.; Solaimuthu, C. Evaporation Rate and Engine Performance Analysis of Coated Diesel Engine Using Raphanus Sativus Biodiesel and Its Diesel Blends. *Int. J. Ambient Energy* **2015**, *38* (2), 1–7. https://doi.org/10.1080/01430750.2015.1086673.

(11) Bilde, M.; Barsanti, K.; Booth, M.; Cappa, C. D.; Donahue, N. M.; Emanuelsson, E. U.; McFiggans, G.; Krieger, U. K.; Marcolli, C.; Topping, D.; Ziemann, P.; Barley, M.; Clegg, S.; Dennis-Smither, B.; Hallquist, M.; Hallquist, Å. M.; Khlystov, A.; Kulmala, M.; Mogensen, D.; Percival, C. J.; Pope, F.; Reid, J. P.; Ribeiro da Silva, M. A. V.; Rosenoern, T.; Salo, K.; Soonsin, V. P.; Yli-Juuti, T.; Prisle, N. L.; Pagels, J.; Rarey, J.; Zardini, A. A.; Riipinen, I. Saturation Vapor Pressures and Transition Enthalpies of Low-Volatility Organic Molecules of Atmospheric Relevance: From Dicarboxylic Acids to Complex Mixtures. *Chem. Rev.* **2015**, *115* (10), 4115–4156. https://doi.org/10.1021/cr5005502.

(12) Pope, F. D.; Tong, H.-J.; Dennis-Smither, B. J.; Griffiths, P. T.; Clegg, S. L.; Reid, J. P.; Cox, R. A. Studies of Single Aerosol Particles Containing Malonic Acid, Glutaric Acid, and Their Mixtures with Sodium Chloride. II. Liquid-State Vapor Pressures of the Acids. *J. Phys. Chem. A* **2010**, *114* (37), 10156–10165. https://doi.org/10.1021/jp1052979.

(13) Rozaini, M. Z. H.; Brimblecombe, P. The Odd Even Behaviour of Dicarboxylic Acids Solubility in the Atmospheric Aerosols. *Water. Air. Soil Pollut.* **2009**, *198* (1–4), 65–75. https://doi.org/10.1007/s11270-008-9826-5.

(14) Bilde, M.; Svenningsson, B.; Mønster, J.; Rosenørn, T. Even−Odd Alternation of Evaporation Rates and Vapor Pressures of C3−C9 Dicarboxylic Acid Aerosols. *Env Sci Technol* **2003**, *37* (7), 1371–1378.

(15) Soonsin, V.; Zardini, A. A.; Marcolli, C.; Zuend, A.; Krieger, U. K. The Vapor Pressures and Activities of Dicarboxylic Acids Reconsidered: The Impact of the Physical State of the Aerosol. **2010**. https://doi.org/10.5194/acpd-10-20515-2010.

(16) Huisman, A. J.; Krieger, U. K.; Zuend, A.; Marcolli, C.; Peter, T. Vapor Pressures of Substituted Polycarboxylic Acids Are Much Lower than Previously Reported. *Atmos Chem Phys* **2013**, *13* (13), 6647--6662. https://doi.org/10.5194/acp-13-6647-2013.

(17) Bilde, M.; Svenningsson, B.; Monster, J.; Rosenorn, T. Even Odd Alternation of Evaporation Rates and Vapor Pressures of C3−C9 Dicarboxylic Acid Aerosols. *Environ. Sci. Technol.* **2003**, *37*, 1371–1378.

(18) Tao, F.; Bernasek, S. L. Understanding Odd−Even Effects in Organic Self-Assembled Monolayers. *Chem. Rev.* **2007**, *107* (5), 1408–1453. https://doi.org/10.1021/cr050258d.

(19) Salo, K.; Jonsson, Å. M.; Andersson, P. U.; Hallquist, M. Aerosol Volatility and Enthalpy of Sublimation of Carboxylic Acids. *J. Phys. Chem. A* **2010**, *114* (13), 4586–4594. https://doi.org/10.1021/jp910105h.

(20) Koponen, I. K.; Riipinen, I.; Hienola, A.; Kulmala, M.; Bilde, M. Thermodynamic Properties of Malonic, Succinic, and Glutaric Acids: Evaporation Rates and Saturation Vapor Pressures. *Environ. Sci. Technol.* **2007**, *41* (11), 3926–3933. https://doi.org/10.1021/es0611240.

(21) Booth, A. M.; Barley, M. H.; Topping, D. O.; McFiggans, G.; Garforth, A.; Percival, C. J. Solid State and Sub-Cooled Liquid Vapour Pressures of Substituted Dicarboxylic Acids Using Knudsen Effusion Mass Spectrometry (KEMS) and Differential Scanning Calorimetry. *Atmospheric Chem. Phys.* **2010**, *10* (10), 4879–4892. https://doi.org/10.5194/acp-10-4879-2010.

(22) Cappa, C. D.; Lovejoy, E. R.; Ravishankara, A. R. Determination of Evaporation Rates and Vapor Pressures of Very Low Volatility Compounds: A Study of the C_4 −C_{10} and C_{12} Dicarboxylic Acids. *J. Phys. Chem. A* **2007**, *111* (16), 3099–3109. https://doi.org/10.1021/jp068686q.

(23) Chattopadhyay, S.; Ziemann, P. J. Vapor Pressures of Substituted and Unsubstituted Monocarboxylic and Dicarboxylic Acids Measured Using an Improved Thermal Desorption Particle Beam Mass Spectrometry Method. *Aerosol Sci. Technol.* **2005**, *39* (11), 1085–1100. https://doi.org/10.1080/02786820500421547.

(24) Soonsin, V.; Zardini, A. A.; Marcolli, C.; Zuend, A.; Krieger, U. K. The Vapor Pressures and Activities of Dicarboxylic Acids Reconsidered: The Impact of the Physical State of the Aerosol. *Atmospheric Chem. Phys.* **2010**, *10* (23), 11753–11767. https://doi.org/10.5194/acp-10-11753-2010.

(25) Price, C. L.; Bain, A.; Wallace, B. J.; Preston, T. C.; Davies, J. F. Simultaneous Retrieval of the Size and Refractive Index of Suspended Droplets in a Linear Quadrupole Electrodynamic Balance. *J. Phys. Chem. A* **2020**, *124* (9), 1811–1820. https://doi.org/10.1021/acs.jpca.9b10748.

(26) Davies, J. F. Mass, Charge, and Radius of Droplets in a Linear Quadrupole Electrodynamic Balance. *Aerosol Sci. Technol.* **2019**, *53*, 309–320. https://doi.org/10.1080/02786826.2018.1559921.

(27) Krieger, U. K.; Marcolli, C.; Reid, J. P. Exploring the Complexity of Aerosol Particle Properties and Processes Using Single Particle Techniques. *Chem. Soc. Rev.* **2012**, *41* (19), 6631. https://doi.org/10.1039/c2cs35082c.

(28) Preston, T. C.; Reid, J. P. Determining the Size and Refractive Index of Microspheres Using the Mode Assignments from Mie Resonances. *J. Opt. Soc. Am. A* **2015**, *32* (11), 2210. https://doi.org/10.1364/JOSAA.32.002210.

(29) Bohren, C. F.; Huffman, D. R. *Absorption and Scattering of Light by Small Particles*; John Wiley and Sons: New York, 1983.

(30) Davies, J. F.; Price, C. L.; Choczynski, J.; Kohli, R. K. Hygroscopic Growth of Simulated Lung Fluid Aerosol Particles under Ambient Environmental Conditions. *Chem. Commun.* **2021**, *57* (26), 3243–3246. https://doi.org/10.1039/D1CC00066G.

(31) Kulmala, M. Condensational Growth and Evaporation in the Transition Regime. *Aerosol Sci. Technol.* **1993**, *19* (3), 381–388. https://doi.org/10.1080/02786829308959645.

(32) Bird, R. B.; Stewart, W. E.; Lightfoot, E. N. *Transport Phenomena, 2nd Edition*, 2nd ed.; John Wiley and Sons: New York, 2002.

(33) Neufeld, P. D.; Janzen, A. R.; Aziz, R. A. Empirical Equations to Calculate 16 of the Transport Collision Integrals Ω(l, s)* for the Lennard-Jones (12–6) Potential. *J. Chem. Phys.* **1972**, *57* (3), 1100–1102. https://doi.org/10.1063/1.1678363.

(34) Marrero, T. R.; Mason, E. A. Gaseous Diffusion Coefficients. *J. Phys. Chem. Ref. Data* **1972**, *1* (1), 3–118. https://doi.org/10.1063/1.3253094.

(35) Davies, J. F.; Haddrell, A. E.; Reid, J. P. Time-Resolved Measurements of the Evaporation of Volatile Components from Single Aerosol Droplets. *Aerosol Sci. Technol.* **2012**, *46* (6), 666–677. https://doi.org/10.1080/02786826.2011.652750.

(36) Logozzo, A.; Preston, T. C. Temperature-Controlled Dual-Beam Optical Trap for Single Particle Studies of Organic Aerosol. *J. Phys. Chem. A* **2022**, *126* (1), 109–118. https://doi.org/10.1021/acs.jpca.1c09363.

(37) Riipinen, I.; Koponen, I. K.; Frank, G. P.; Hyvärinen, A.-P.; Vanhanen, J.; Lihavainen, H.; Lehtinen, K. E. J.; Bilde, M.; Kulmala, M. Adipic and Malonic Acid Aqueous Solutions: Surface Tensions and Saturation Vapor Pressures. *J. Phys. Chem. A* **2007**, *111* (50), 12995–13002. https://doi.org/10.1021/jp073731v.

(38) Mønster, J.; Rosenørn, T.; Svenningsson, B.; Bilde, M. Evaporation of Methyl- and Dimethyl-Substituted Malonic, Succinic, Glutaric and Adipic Acid Particles at Ambient Temperatures. *J. Aerosol Sci.* **2004**, *35* (12), 1453–1465. https://doi.org/10.1016/j.jaerosci.2004.07.004.

(39) Yeung, M. C.; Ling, T. Y.; Chan, C. K. Effects of the Polymorphic Transformation of Glutaric Acid Particles on Their Deliquescence and Hygroscopic Properties. *J. Phys. Chem. A* **2010**, *114* (2), 898–903. https://doi.org/10.1021/jp908250v.

(40) Espeau, P.; Négrier, P.; Corvis, Y. Crystallographic and Pressure Temperature State Diagram Approach for the Phase Behavior and Polymorphism Study of Glutaric Acid. *Cryst. Growth Des.* **2013**, *13* (2), 723–730. https://doi.org/10.1021/cg301442f.

(41) Hansen, A. R.; Beyer, K. D. Experimentally Determined Thermochemical Properties of the Malonic Acid/Water System: Implications for Atmospheric Aerosols. *J. Phys. Chem. A* **2004**, *108* (16), 3457–3466. https://doi.org/10.1021/jp0376166.

(42) Reddy, J. P.; Delori, A.; Foxman, B. M. Molecular and Crystal Structure of a New Polymorph of Malonic Acid with $Z'=3$. *J. Mol. Struct.* **2013**, *1041*, 122–126. https://doi.org/10.1016/j.molstruc.2013.03.017.

(43) Kim, P.; Continetti, R. E. Accelerated Keto Enol Tautomerization Kinetics of Malonic Acid in Aqueous Droplets. *ACS Earth Space Chem.* **2021**, *5* (9), 2212–2222. https://doi.org/10.1021/acsearthspacechem.1c00221.

(44) Leopold, K. R.; Haim, A. Equilibrium, Kinetics, and Mechanism of the Malonic Acid-Iodine Reaction. *Int. J. Chem. Kinet.* **1977**, *9* (1), 83–95. https://doi.org/10.1002/kin.550090108.

(45) Tikkanen, O.-P.; Buchholz, A.; Ylisirniö, A.; Schobesberger, S.; Virtanen, A.; Yli-Juuti, T. Comparing Secondary Organic Aerosol (SOA) Volatility Distributions Derived from Isothermal SOA Particle Evaporation Data and FIGAERO–CIMS Measurements. *Atmospheric Chem. Phys.* **2020**, *20* (17), 10441–10458. https://doi.org/10.5194/acp-20-10441-2020.

(46) Kohli, R. K.; Davies, J. F. Measuring the Chemical Evolution of Levitated Particles: A Study on the Evaporation of Multicomponent Organic Aerosol. *Anal. Chem.* **2021**, *93* (36), 12472–12479. https://doi.org/10.1021/acs.analchem.1c02890.

(47) Kaur Kohli, R.; Van Berkel, G. J.; Davies, J. F. An Open Port Sampling Interface for the Chemical Characterization of Levitated Microparticles. *Anal. Chem.* **2022**, *94* (8), 3441–3445. https://doi.org/10.1021/acs.analchem.1c05550.

(48) Jacobs, M. I.; Davies, J. F.; Lee, L.; Davis, R. D.; Houle, F.; Wilson, K. R. Exploring Chemistry in Microcompartments Using Guided Droplet Collisions in a Branched Quadrupole Trap Coupled to a Single Droplet, Paper Spray Mass Spectrometer. *Anal. Chem.* **2017**, *89* (22), 12511–12519. https://doi.org/10.1021/acs.analchem.7b03704.

CHAPTER VI

Conclusions and Future Directions

The work described in this thesis aims to provide a detailed understanding of the physical chemistry of aerosol particles to better understand their role in the environment. Aerosol in the atmosphere affect visibility, air quality, and climate, and are constantly transformed due to environmental conditions, altering their physical, chemical and optical properties. Aerosol is composed of organic and inorganic species. Atmospheric reactions affect and alter properties such as volatility, hygroscopicity, and phase state further complicating impacts on visibility, air quality and climate. The aims of this thesis were to develop an instrument that can probe the microphysical properties of aerosol through single particle levitation. A linear quadrupole electrodynamic balance (LQ-EDB) coupled to a broadband light source was constructed and analytical tools were developed explore the physical properties of aerosol particles.

6.1. Thesis Summary and Conclusions

Chapter 2 introduced the instrumentation used to levitate and probe particles using a LQ-EDB with Mie resonance spectroscopy. These methods are complementary to traditional methods used to study aerosol, and provide additional information on the physical characteristics of aerosol particles. The use of single particle techniques, like the electrodynamic balance, provide a further understanding of the microphysical state of aerosol particles and can be suspended for extended periods of time, mimicking the time frames of atmospheric processes.

The linear-quadrupole electrodynamic balance (LQ-EDB), compared to other single particle techniques and EDB configurations, provides:

- Ease of particle trapping and extended levitation using the DC voltage PID feedback loop through LabVIEW software.
- Capability to quickly change environmental conditions of the LQ-EDB to better simulate natural atmospheric processes.
- Ability to probe the physical and optical properties of aerosol particles using Mie resonance spectroscopy and simultaneously retrieve the size and refractive index using MRFIT.

Chapter 3 builds upon Chapter 2 and explained the methods used to benchmark the LQ-EDB setup coupled to Mie resonance spectroscopy. The influence of LED illumination was ruled out by exposing particles to different intensities and ensuring the spectra did not change. The evaporation of a series of glycols were characterized and their vapor pressures were determined and compared to literature values to benchmark the instrument. To determine the accuracy of the experimental setup, the refractive index (RI) at the deliquescence relative humidity of a well characterized component, NaCl, was noted. The size was determined within ± 5 nm and RI ± 0.002 – 0.005. The hygroscopic growth of NaCl was then used to determine the wavelength-dependence of the RI to apply our methods to a broader range of wavelengths. Finally, the instrument was used to probe particles containing humic acid, a light absorbing compound, to explore the influence of light absorption on Mie resonance spectra, providing a foundation for the work in Chapter 4.

The capability of exploring particles containing light absorbing compounds was taken a step further in Chapter 4 where the instrumentation was used to probe samples containing 4-nitrocatechol (4-NC), a known brown carbon (BrC) compound. In these experiments, the dual droplet method, where a second levitated particles is used as an RH probe, was used to characterize the RH in the chamber rather than relying on the RH probe reading. Initially, the hygroscopic growth of pure 4-NC particles was explored to determine the radial growth factors (rGF), the hygroscopicity parameter, kappa, and pure component RI. Ammonium sulfate was then mixed with 4-NC in increasing molar ratios to determine its effect on hygroscopicity. Overall, the rGF's increased with an increasing amount of ammonium sulfate, due to the larger hygroscopicity of ammonium sulfate. These mixed particles also showed signs of liquid-liquid phase separation (LLPS) in which the separation relative humidity (SRH) decreased with increasing amounts of ammonium sulfate. The methods developed here may be applied to other particles containing BrC, establishing procedures for future studies on a wider range of chromophores.

The LQ-EDB used in Chapters 3 and 4 was re-designed to include heating cartridges to raise the temperature of the chamber. The temperature was measured with a thermistor probe and was precisely calibrated from the evaporation rate of a well-characterized compound, glycerol. After temperature calibration, the evaporation rates of a series of dicarboxylic acids (malonic, succinic, glutaric, and adipic acid) at temperatures ranging from 303 to 353 K were measured. These compounds existed as either a spherical amorphous or aspherical crystalline particles, depending on their physical state. Generally, even-number molecules with lower solubility formed crystalline phases while odd-

numbered molecules randomly formed either the crystalline or amorphous phase. This technique allowed us to detect several polymorphs of malonic acid. Overall, the crystalline vapor pressures were much lower than the spherical vapor pressures, allowing a comparison of the thermodynamics of vaporization and sublimation. Going forwards, this method will allow for vapor pressure measurements on low and very low volatility compounds, providing useful information for atmospheric processes such as new particle formation.

6.2. Future Directions

The techniques and experimental methods introduced throughout this thesis serve as a basis for future experiments, allowing for the exploration of many aerosol particle properties including phase state, hygroscopicity, diffusion, and viscosity.

6.2.1. Future Evaporation Measurements

The dicarboxylic acid evaporation measurements from Chapter 5 will be expanded upon through the investigation into the properties of mixed particles. Further work is needed to characterize the vapor pressures of particles containing two or more components. This work will include the use of a high-resolution mass spectrometer to perform a compositional analysis of complex mixtures as they undergo evaporation.[1,2] These measurements will provide a compositionally-resolved measurement of multi-component evaporation allowing the thermodynamic properties individual components to be resolved.

6.2.2. Future BrC Measurements

The measurements and techniques reported in Chapter 4 served as a model that can be applied to other BrC containing particles. These methods will be applied to the study of other nitro-aromatic compounds to further explore the physical and optical properties of BrC. Furthermore, they provide the foundation to facilitate the exploration of chamber generated secondary organic aerosol (SOA) containing BrC, allowing us to apply single particle methods to chamber generated aerosol particles to reveal previously unresolved properties and processes. Finally, measurements connecting the photochemical transformations of light absorbing aerosol particles with their physical characteristics will reveal much needed information that will inform how BrC aerosol evolve in the atmosphere.

6.3. References

(1) Kohli, R. K.; Davies, J. F. Measuring the Chemical Evolution of Levitated Particles: A Study on the Evaporation of Multicomponent Organic Aerosol. *Anal. Chem.* **2021**, *93* (36), 12472–12479. https://doi.org/10.1021/acs.analchem.1c02890.

(2) Kaur Kohli, R.; Van Berkel, G. J.; Davies, J. F. An Open Port Sampling Interface for the Chemical Characterization of Levitated Microparticles. *Anal. Chem.* **2022**, *94* (8), 3441–3445. https://doi.org/10.1021/acs.analchem.1c05550.